Department of Applied Physics

Fully Relativistic Convergent Close-Coupling Method

Christopher J. Bostock

This thesis is presented for the Degree of
Doctor of Philosophy
of
Curtin University of Technology

August, 2010

Declaration

To the best of my knowledge and belief this thesis contains no material previously published by any other person except where due acknowledgment has been made. This thesis contains no material which has been accepted for the award of any other degree or diploma in any university.

Christopher J. Bostock
August, 2010

Abstract

The calculation of accurate excitation and ionization cross sections for electron collisions with atoms and ions plays a fundamental role in atomic and molecular physics, laser physics, x-ray spectroscopy, plasma physics and chemistry. Within the veil of plasma physics lie important research areas affiliated with the lighting industry, nuclear fusion, and astrophysics. For high energy projectiles or targets with a large atomic number it is presently understood that a scattering formalism based on the Dirac equation is required to incorporate relativistic effects. This thesis reports on the development of the relativistic convergent close-coupling (RCCC) method and highlights the following three main accomplishments:

1. The inclusion of the Breit interaction, a relativistic correction to the coulomb potential, in the RCCC method. This led to calculations that resolved a discrepancy between theory and experiment for the polarization of x-rays emitted by highly charged hydrogenlike ions excited by electron impact. X-rays emitted from plasmas can be used as a diagnostic tool. The RCCC results were published in *Phys. Rev. A*, 80(5):052708, 2009.

2. The extension of the RCCC method to accommodate two electron and quasi-two electron targets. The method was applied to electron scattering from mercury. Accurate plasma physics modeling of mercury based fluorescent lamps requires detailed information on a large number of electron impact excitation cross sections involving transitions between various states. The RCCC results were published in *Phys. Rev. A*, 82(2):022713, 2010.

3. The third accomplishment outlined in this thesis is the restructuring of the RCCC computer code (approximately 40000 lines of Fortran)

to utilize a hybrid OpenMP-MPI parallelization scheme which now enables the RCCC code to run on the recently commissioned 11900 cpu supercomputer at the National Computational Infrastructure Facility in Canberra.

The work presented in this thesis has resulted in international collaborations with both experimentalists and other theorists in the field of relativistic electron scattering. For example, the work on the Breit interaction has led to a collaboration with experimentalists at the GSI Helmholtz Centre for Heavy Ion Research in Germany, and total ionization cross sections for highly charged ions generated with the RCCC method are useful for plasma modelers in the USA.

List of Publications

During the course of this PhD project several manuscripts have been published in refereed journals and the research results have been presented at international conferences.

REFEREED PUBLICATIONS

- Christopher J. Bostock, Dmitry V. Fursa, and Igor Bray. Relativistic convergent close-coupling method applied to electron scattering from mercury. *Phys. Rev. A*, 82(2):022713, 2010
- Christopher J. Bostock, Dmitry V. Fursa, and Igor Bray. Relativistic convergent close-coupling method: Calculation of electron scattering from hydrogenlike ions. *Phys. Rev. A*, 80(5):052708, 2009
- Dmitry V. Fursa, Christopher J. Bostock, and Igor Bray. Relativistic convergent close-coupling method: Calculation of electron scattering from cesium. *Phys. Rev. A*, 80(2):022717, 2009

CONFERENCE PROCEEDINGS

- C. Bostock and D. V. Fursa and I. Bray. Inclusion of the Breit interaction in the relativistic convergent close-coupling method. *Journal of Physics: Conference Series*, Vol. 194(6):062005, 2009
- Christopher J. Bostock, Dmitry V. Fursa, and Igor Bray. Polarization of the Lyman-α_1 x-ray line emitted by hydrogen-like Ti^{21+}, Ar^{17+} and Fe^{25+} ions excited by electron impact. [10th International Colloquium on Atomic Spectra and Oscillator Strengths for Astrophysical and Laboratory Plasmas, Berkeley, California. To be published in *Canadian Journal of Physics*, 2011.]

Contents

Contents

List of Tables

List of Tables

List of Figures

List of Figures

List of Figures

Acknowledgments

I wish to thank my supervisor Assoc. Prof. Dmitry Fursa for his invaluable assistance and guidance throughout the period of this research. Similarly, it has been a pleasure to work with and learn from Prof. Igor Bray.

I also wish to thank all members of the Institute of Theoretical Physics, including visitors, especially Klaus Bartschat, for the congenial atmosphere in which to work.

I am grateful to the Australian Research Council for the funding which enabled this research, as well as the presentation of the research results at international conferences. Resources of the Australian National Computational Infrastructure Facility and its Western Australian node iVEC are gratefully acknowledged.

Numerous other people have provided assistance during this research work: Dr. Harry Quiney (The University of Melbourne), Dr. Chris Fontes (Los Alamos National Laboratory), Dr. George Csanak (Los Alamos National Laboratory) and Dr. Günter Weber (GSI Germany).

Finally, and most importantly, special thanks go to my family, in particular my fiancée, Yvette, for her constant encouragement, support and proof reading prowess.

Chapter 1

Introduction

Many of the major discoveries in physics have involved scattering experiments: Rutherford's students, Geiger and Marsden [23] scattered alpha particles from a thin gold foil which lead to the groundbreaking discovery of the atomic nucleus; high energy electrons scattering from protons at the Standford Linear Accelerator elucidated the quark constituents of protons; Franck and Hertz [24] scattered electrons from gaseous mercury atoms to unveil the quantized energy levels in atoms. Practical applications abound: the underlying structure of materials and biological specimens can be obtained via the coherent scattering of x-rays, neutrons and electrons from relevant samples.

Both theory and experiment are crucial in the development of scattering techniques. There have been examples (addressed in the following paragraphs) where experiments have been in disagreement with theory, and revisiting the experiments has uncovered problems with the experimental technique. The relativistic convergent close-coupling (RCCC) method is a theory that enables the calculation of data for a wide variety of electron collisions with atoms and ions. It can be used in Franck-Hertz type experiments involving electron collisions with atoms such as mercury, and even in high energy (several hundred keV) electron collisions with highly charged ions such as U^{91+}.

Interestingly, the RCCC method, even though it is now primarily applied to electron scattering from atoms and ions, has its roots in nuclear physics. In the 1980's, McCarthy and Stelbovics, two theoretical physicists in the field of nuclear scattering, took a technique that was being used in nuclear

scattering theories and applied it to the problem of electron scattering from hydrogenlike ions [25]. The technique relied on solving the non-relativistic Lippmann-Schwinger equation [26] in momentum space for the scattering system. In the following decade the method was refined, culminating in 1992 with the work of Bray and Stelbovics [27] who explicitly demonstrated that the solution of the Lippmann-Schwinger equation in momentum space for the electron-hydrogen scattering problem converged as the scattering wave function was expanded in a basis set of increasing size. The theory proved to be robust and obtained excellent agreement with most, but not all experiments. The experiments that were in disagreement were repeated, and it was subsequently found that there were problems with the initial experiments. The new experiments were in agreement with the CCC theory [27–31]. The scattering theory developed by Bray and Stelbovics was called the convergent close-coupling (CCC) method: convergent because the solution to the Lippmann-Schwinger equation converged with increasing size of the basis set used in the expansion of the scattering wavefunction. The "close-coupling" terminology stems from the historical fact that many of the previous scattering theories expanded the scattering wavefunction in terms of only the "close" low-lying states of the target [32, 33].

The CCC method was further extended by Fursa and Bray [34] so that it was applicable to electron scattering from heliumlike targets. Again there was disagreement with certain experiments. These experiments were repeated and agreement was obtained with the CCC method [35, 36]. The CCC method was generalized to electron scattering from alkali atoms [37] and alkali-earth atoms [38]. It is applicable to ionizing collisions [39–42] in addition to excitation processes. The CCC method was developed as a non-relativistic theory, however it is presently understood that a more suitable method based on the Dirac equation is required for the description of scattering processes involving high energy projectiles and/or targets with a large atomic number. Before launching into a description of the relativistic convergent close-coupling method, the subject of this thesis, a brief excursion into the domain of relativistic quantum electrodynamics is required in order to set the scene in which the method is applicable.

In 1905 Einstein published a paper [43], "On the Electrodynamics of Moving Bodies" in which he indicated that if the equations of classical electromagnetism, Maxwell's equations, were to remain invariant in all inertial

frames, then restrictions were required in the way spatial (x,y,z) and time (t) variables transform between inertial frames.* Einstein then postulated that the same transformations apply to kinematics and dynamics and not just Maxwell's equations, which lead to constraints on the relationship between energy, momentum and mass: $E^2 = p^2c^2 + m^2c^4$ in the relativistic case as opposed to $E = p^2/2m$ in the non-relativistic case. Schrödinger in the 1920's initially attempted to produce a relativistic quantum theory [45], but on encountering difficulties in describing the spectrum of hydrogen, published a non-relativistic version of wave mechanics [46–51]. This was shown to be equivalent to Heisenberg's matrix mechanics [52, 53]. Dirac's relativistic wave equation [54, 55] accounted for the electron's spin and produced the correct hydrogen spectrum. However, Schrödinger's initial relativistic wave equation (now called the Klein-Gordon equation) and Dirac's relativistic wave equation, both encountered problems: the former could not account for spin, and the latter admitted negative energy states which required an *ad hoc* fix involving a filled sea of negative energy states [55]. Positrons could be interpreted as holes in this negative energy sea. The problems associated with the single particle Klein-Gordon and the single particle Dirac equation were ultimately resolved by the machinery of quantum field theory which can adequately accommodate particle creation and destruction. Developed by physicists such as Pauli, Jordan, Wigner, Fermi, Dirac and others, the new theory in turn had its problems, such as infinities that appear in calculations. These infinities were tamed with techniques developed mainly by Schwinger [56–59], Tomonaga [60] and Feynman [61–63] for which they were awarded the 1965 Nobel Prize. Dyson [64, 65] showed that the field quantization methods of Schwinger and Tomonaga were equivalent to Feynman's propagator method based on wave equations. The current formulation of the theory [66, 67], known as relativistic quantum electrodynamics (or QED for short) is one of the most precisely tested theories in physics. The calculation of the Lamb shift [68, 69] and radiative corrections to the anomalous magnetic moment of the electron [56–58] are often cited as two of its crowning achievements.

In 1951 Furry [70] extended the theory of quantum electrodynamics so that it could accommodate processes involving bound states, such as those found in atomic and molecular physics. Contemporary treatises [71, 72]

*See Schwartz [44] for an English translation of Einstein's original paper.

stress that the Furry bound state interaction picture is the most appropriate framework in which to calculate QED effects in atoms and molecules.

The RCCC method involves solving the relativistic Lippmann-Schwinger equation in momentum space. In turn, the relativistic Lippmann-Schwinger equation is based on the single particle Dirac equation. Other relativistic scattering theories based on the Dirac equation also exist. The most advanced of them are the Dirac R-matrix method [73–76], the recently developed Dirac B-spline R-matrix method (DBRM) [77, 78] and Dirac R-matrix with pseudo-states method (DRMPS) [79]. Time dependent scattering methods based on the Dirac equation also exist, such as the time dependent close-coupling method developed by Pindzola et al. [80].

Theories based on the single particle Dirac equation, as opposed to quantum field theory, encounter conceptual and technical difficulties when issues associated with negative energy states and particle creation and destruction are considered. As highlighted by Sakurai [81] many of these issues can be resolved when the full framework of quantum field theory is employed in the analysis of a problem. To whet the appetite of the interested reader, Appendix F highlights some of the conceptual tensions that exist in relativistic quantum theories.

The remainder of this thesis is organized as follows: Chapter 2 outlines the theory underlying the calculation of electron scattering on hydrogenlike targets using the RCCC method. The inclusion of the Breit and Møller interactions in the RCCC method is described in Chapter 3. These inclusions lead to calculations that resolved a discrepancy between theory and experiment for the polarization of x-rays emitted by highly charged hydrogenlike ions excited by electron impact. In Chapter 4, the extension of the RCCC method to accommodate two-electron and quasi two-electron targets is described in detail. The method is applied to electron scattering from mercury, which plays an important role in the lighting industry. Electron scattering from mercury is also of importance in testing fundamental aspects of scattering theory associated with the formation of negative ion resonances. The RCCC method can resolve such resonances, whereas the non-relativistic CCC method could not. The last Chapter describes how the RCCC computer code (approximately 40000 lines of Fortran) was restructured to employ a hybrid OpenMP-MPI parallelization scheme. This allowed it run on the recently commissioned 11900 cpu supercomputer at

the National Computational Infrastructure Facility in Canberra. This allows the RCCC method to not only perform larger calculations, but a calculation of a given size also scales very well with the number of cpus used. That is, increasing the number of cpus used in the calculation by a given factor reduces the calculation time by approximately the same factor.

For the benefit of future graduate students, included in the appendices are detailed derivations of the partial wave expansion of the relativistic Lippmann-Schwinger equation, and also expressions for partial wave cross sections and integrated cross sections. Such derivations are not usually included in research articles, nor in other literature in the field of relativistic scattering theory.

Chapter 2

The RCCC method for hydrogenlike and quasi-hydrogenlike targets

In this Chapter a detailed formulation of the relativistic convergent close-coupling (RCCC) method is presented for the general case of electron scattering from quasi-hydrogenlike targets. A square-integrable Dirac L-spinor basis is used to obtain a set of target states representing both the bound and continuum spectra of the target. A set of momentum-space coupled relativistic Lippmann-Schwinger equations (based on the Dirac equation) for the T-matrix is then formulated and solved. Expressions for scattering amplitudes, cross sections, and spin assymetry parameters are presented. These expressions are then utilized in Chapter 3 which contains results for electron scattering on highly charged hydrogenlike ions.

2.1 Target structure

We assume that the target atom or ion is well described by a model of one electron above a frozen Dirac-Fock core. The set of core orbitals $\{\varphi_{\rm c}\}$ is obtained by performing a self-consistent field Dirac-Fock calculation using, for example, the GRASP package [82]. The resulting Dirac equation for the active electron wave function is

$$H_{\rm T}\phi(\boldsymbol{r}) = \Big(c\,\boldsymbol{\alpha}\cdot\boldsymbol{p} + \beta m_0 c^2 + V_{\rm T}\Big)\,\phi(\boldsymbol{r}) = \epsilon\phi(\boldsymbol{r}), \tag{2.1}$$

where $\boldsymbol{\alpha}$ and β are the Dirac matrices, c is the speed of light, m_0 is the electron mass, $\boldsymbol{p}$ is the momentum operator. In what follows we will use atomic units: $m_0 = 1$ and $c \approx 137$. For a central potential V_T the solutions of the Dirac equation (2.1) are characterized by the relativistic quantum number κ and are given by a four-component spinor [83]

$$\phi_{\kappa m}(\boldsymbol{r}) = \frac{1}{r}\begin{pmatrix} \phi^\mathrm{L}_\kappa(r)\,\chi_{\kappa m} \\ i\phi^\mathrm{S}_\kappa(r)\,\chi_{-\kappa m} \end{pmatrix}. \tag{2.2}$$

Here $\phi^\mathrm{L}_\kappa(r)$ and $\phi^\mathrm{S}_\kappa(r)$ are the large and small components of the radial wave function, $\chi_{\kappa m}$ is a two-component coupled spin-orbit function, m is the magnetic quantum number. The relativistic quantum number κ is related to the total angular momentum j and parity $\pi = (-1)^l$ of the orbital via

$$j = |\kappa| - \frac{1}{2}, \tag{2.3}$$

$$l = \begin{cases} \kappa, & \kappa > 0, \\ -\kappa - 1, & \kappa < 0. \end{cases} \tag{2.4}$$

The potential V_T of interaction of the active electron with a closed core is a sum of a frozen-core Dirac-Fock potential V^FC and a polarization potential V^pol,

$$V_\mathrm{T} = V^\mathrm{FC} + V^\mathrm{pol}. \tag{2.5}$$

The non-local V^FC potential is defined as a sum of local (direct) V^FC_d and non-local (exchange) terms,

$$V_\mathrm{T} = V^\mathrm{FC}_\mathrm{d} + V^\mathrm{FC}_\mathrm{e}, \tag{2.6}$$

with

$$V^\mathrm{FC}_\mathrm{d}\phi(\boldsymbol{r}) = \left(-\frac{Z}{r} + \sum_{\varphi_\mathrm{c}} \int d^3r' \frac{|\varphi_\mathrm{c}(\boldsymbol{r'})|^2}{|\boldsymbol{r} - \boldsymbol{r'}|}\right)\phi(\boldsymbol{r}), \tag{2.7}$$

$$V^\mathrm{FC}_\mathrm{e}\phi(\boldsymbol{r}) = -\sum_{\varphi_\mathrm{c}} \int d^3r' \frac{\varphi_\mathrm{c}(\boldsymbol{r'})^*\phi(\boldsymbol{r'})}{|\boldsymbol{r} - \boldsymbol{r'}|}\varphi_\mathrm{c}(\boldsymbol{r}). \tag{2.8}$$

We use a point-nuclear model with Z being the nuclear charge. The number of electrons in the frozen core is $N_\mathrm{c} = \sum_{\varphi_\mathrm{c}}(2j_\mathrm{c} + 1)$. Note that for neutral atoms $Z = N_\mathrm{c} + 1$, but for positively charged ions the asymptotic charge of

the target is nonzero,

$$Z_{\rm as} = Z - N_{\rm c} - 1. \tag{2.9}$$

The phenomenological one-electron core polarization potential $V^{\rm pol}$ allows us to take into account more accurately the effect of closed inert shells on the active electron. For light atoms and ions a simple model used in the nonrelativistic CCC method [37] can be employed. However, for heavy targets, such as cesium, a more accurate form of polarization potential is necessary. The polarized-orbital methods of McEachran et al. [84] can be used to produce the polarization potential from the core orbitals.

2.2 Diagonalization of the Dirac Hamiltonian

The key step in the formulation of the CCC method is the diagonalization of the nonrelativistic Schrödinger Hamiltonian of the target in a finite-size Sturmian basis. In the case of the Dirac Hamiltonian, diagonalization in a finite-size basis proved to be a significantly more complicated problem. Firstly, the spectrum of the Dirac Hamiltonian of a hydrogenlike atom does not have a finite lower bound and consists of three distinct intervals: the continuous spectrum $(-\infty, -c^2)$ corresponding to the negative energy electrons (positrons), the discrete spectrum $(-c^2, c^2)$ containing the target bound states, and the target continuous spectrum (c^2, ∞), see Fig. 2.1 below. The absence of the lowest-energy state for the Dirac Hamiltonian means that the variational principle and techniques derived from it such as diagonalization in the finite-size basis cannot be applied to the problem, at least not in the same straightforward manner as is done for the nonrelativistic Schrödinger Hamiltonian. Secondly, the choice of the basis proved to be very important as a simple generalization of the nonrelativistic diagonalization techniques leads to the appearance of so-called "intruder" states [85] that carry no physical meaning and were an artifact of the incorrect account of the interaction between the negative energy electron continuum and the positive energy bound and continuum parts of the Dirac equation spectrum.

The problems of the applicability of the variational principle to the Dirac Hamiltonian and choice of the basis for diagonalization have been resolved by Grant and Quiney [86], we refer the reader to this reference for the detailed discussion. We should also note that an alternative but equivalent formulation has been presented by Szmytkowski [87]. In this paper we will

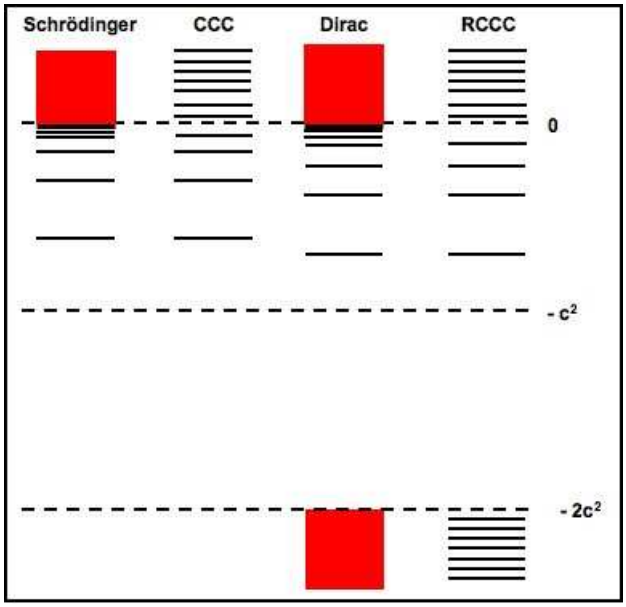

Figure 2.1: A qualitative comparison of the Dirac and Schrödinger target spectra and their discretization using CCC and RCCC methods. The energy was shifted by $-c^2$ to facilitate comparison with CCC. Note that RCCC generally yields a lower energy ground state and that there are states with energy below $-2c^2$ as well as above.

follow the formulation of Grant and Quiney [86].

The target atom wave function $\phi_{\kappa m}(\boldsymbol{r})$ is sought as an expansion [86]

$$\phi_{\kappa m}(\boldsymbol{r}) = \frac{1}{r}\begin{pmatrix} \phi^{\mathrm{L}}_{\kappa}(r)\,\chi_{\kappa m} \\ i\phi^{\mathrm{S}}_{\kappa}(r)\,\chi_{-\kappa m} \end{pmatrix} = \frac{1}{r}\begin{pmatrix} \sum_{n_r} c^{\mathrm{L}}_{n_r} f^{\mathrm{L}}_{n_r\kappa}(r)\,\chi_{\kappa m} \\ i\sum_{n_r} c^{\mathrm{S}}_{n_r} f^{\mathrm{S}}_{n_r\kappa}(r)\,\chi_{-\kappa m} \end{pmatrix}. \qquad (2.10)$$

Here $c^{\mathrm{L}}_{n_r}$ and $c^{\mathrm{S}}_{n_r}$ are expansion coefficients, and $f^{\mathrm{L}}_{n_r\kappa}(r)$ and $f^{\mathrm{S}}_{n_r\kappa}(r)$ are Dirac L-spinors [86]. Dirac L-spinors form a complete square-integrable basis and are the relativistic analogue of Coulomb Sturmian functions (Laguerre functions) which are used in the formulation of the nonrelativistic CCC method. The important feature of the expansion (2.10) is that although the large and small components of the wave function are expanded separately the Dirac L-spinors for large and small components are not independent but satisfy the following system of differential equations,

$$\frac{d}{dr} f^{\mathrm{L}}_{n_r\kappa}(r) \;=\; -\frac{\kappa}{r} f^{\mathrm{L}}_{n_r}(r) + \left(\frac{N_{n_r\kappa} - n_r - \gamma}{r} + \lambda\right) f^{\mathrm{S}}_{n_r}, \qquad (2.11)$$

$$\frac{d}{dr}f^{\rm S}_{n_r\kappa}(r) \;=\; \frac{\kappa}{r}f^{\rm S}_{n_r}(r)+\left(\frac{-N_{n_r\kappa}-n_r-\gamma}{r}+\lambda\right)f^{\rm L}_{n_r}, \qquad (2.12)$$

where $\gamma=\sqrt{\kappa^2-(Z/c)^2}$ and $N_{n_r\kappa}=\sqrt{\kappa^2+2n_r\gamma+{n_r}^2}$. The consequence of this relation is that the large and small components of the Dirac L-spinors satisfy the criterion of strict kinetic balance [86] which guarantees the correct account of the interaction between different parts of the Dirac equation spectrum and the correct transition to the nonrelativistic limit ($c\to\infty$). The explicit form of the Dirac L-spinors is

$$\begin{aligned} f^{\rm L/S}_{n_r\kappa}(r) \;=\; & \left[\frac{n_r!(2\gamma+n_r)}{2N_{n_r\kappa}(N_{n_r\kappa}-\kappa)\Gamma(2\gamma+n_r)}\right]^{1/2}(2\lambda r)^{\gamma}e^{-\lambda r} \\ & \times\left(-(1-\delta_{n_r,0})L^{2\gamma}_{n_r-1}(2\lambda r)\pm\frac{N_{n_r\kappa}-\kappa}{n_r+2\gamma}L^{2\gamma}_{n_r}(2\lambda r)\right), \end{aligned} \qquad (2.13)$$

with the $\pm$ corresponding to the large/small components, respectively. $\Gamma(a)$ is the usual gamma function [88]. Dirac L-spinors are normalized to unity but form a non-orthogonal set. We refer the reader to Ref. [86] for a detailed discussion of the Dirac L-spinors properties, such as orthogonality and the transition to the nonrelativistic limit. We also note that Dirac L-spinors have been used to generate a complete set of pseudostates in the DRMPS method [79].

The problem of diagonalization of the Hamiltonian $H_{\rm T}$ in the basis of L-spinors is divided into two steps. In the first step, we consider the Dirac equation (2.1) with the local part of the potential, $V^{\rm loc}_{\rm T}=V^{\rm FC}_{\rm d}+V^{\rm pol}$, and formulate a standard eigenvalue problem for the expansion coefficients $\{c^{\rm L}_{n_r},c^{\rm S}_{n_r}\}, n_r=1,...,N_\kappa$ by substitution of the expansion (2.10) into the (local) Dirac equation,

$$\begin{aligned} & \sum_{n_r}\langle f^{\rm L}_{m_r\kappa}|V^{\rm loc}_{\rm T}+c^2|f^{\rm L}_{n_r\kappa}\rangle c^{\rm L}_{n_r}-c\sum_{n_r}\langle f^{\rm L}_{m_r\kappa}|\frac{d}{dr}-\frac{\kappa}{r}|f^{\rm S}_{n_r\kappa}\rangle c^{\rm S}_{n_r} \\ & =\sum_{n_r}\epsilon\langle f^{\rm L}_{m_r\kappa}|f^{\rm L}_{n_r\kappa}\rangle c^{\rm L}_{n_r}, \end{aligned} \qquad (2.14)$$

$$c\sum_{n_r}\langle f^{\rm S}_{m_r\kappa}|\frac{d}{dr}+\frac{\kappa}{r}|f^{\rm L}_{n_r\kappa}\rangle c^{\rm L}_{n_r}+\sum_{n_r}\langle f^{\rm S}_{m_r\kappa}|V^{\rm loc}_{\rm T}-c^2|f^{\rm S}_{n_r\kappa}\rangle c^{\rm S}_{n_r}$$

$$= \sum_{n_r} \epsilon \langle f^{\rm S}_{m_r\kappa} | f^{\rm S}_{n_r\kappa} \rangle c^{\rm S}_{n_r}. \tag{2.15}$$

Note that for N_κ L-spinors used in expansion (2.10) the size of the eigenvalue problem is $2N_\kappa$. The result of the diagonalization is a set of $2N$ orbitals $\{\tilde{\phi}_n\}$ and corresponding energies $\tilde{\epsilon}_n$ with N_κ of them describing bound states and discretized continuum states for the potential $V_{\rm T}^{\rm loc}$ and in addition there is a set of N_κ orbitals describing discretized negative energy continuum states, see Fig. 2.1.

According to Dirac [89] the negative energy states are filled with electrons and the Pauli exclusion principle prohibits decay to them from positive energy bound and continuum parts of spectrum. Excitations from the negative energy states results in the creation of electron-positron pairs. The energy required for such processes ($\sim 2c^2 \approx 1$ MeV) is much higher than the energies normally considered in electron-atom collision studies. Therefore we will exclude all negative energy orbitals that come from the diagonalization of the Dirac Hamiltonian.

In the second step we use N_κ (positive-energy) orbitals $\{\tilde{\phi}_n\}$ as a basis to diagonalize the full target Hamiltonian $H_{\rm T}$. This requires evaluation of the matrix elements of the non-local frozen-core potential $V_{\rm e}^{\rm FC}$,

$$\begin{aligned} \langle \tilde{\phi}_n | V_{\rm e}^{\rm FC} | \tilde{\phi}_{n'} \rangle &= \delta_{\kappa_n,\kappa_{n'}} \sum_{\varphi_{\rm c}} \sum_{\lambda} \frac{2j_{\rm c}+1}{2j_n+1} \Pi(\kappa_n, \kappa_{\rm c}, \lambda) \\ &\times (C^{j_n \frac{1}{2}}_{j_{\rm c} \frac{1}{2}, \lambda 0})^2 \int_0^\infty dr' \, \varphi_{\rm c}(r') \tilde{\phi}_n(r') \\ &\times \int_0^\infty dr \, \varphi_{\rm c}(r) \tilde{\phi}_n(r), v_\lambda(r', r), \end{aligned} \tag{2.16}$$

where

$$v_\lambda(r', r) = \begin{cases} r^\lambda / r'^{\lambda+1} & \text{for} \quad r' > r, \\ r'^\lambda / r^{\lambda+1} & \text{for} \quad r' < r, \end{cases} \tag{2.17}$$

and $\Pi(\kappa_n, \kappa_{\rm c}, \lambda)$ incorporates the parity selection rules [90],

$$\Pi(\kappa_n, \kappa_{\rm c}, \lambda) = \frac{1}{2} \left(1 - \frac{\kappa_n}{|\kappa_n|} \frac{\kappa_{\rm c}}{|\kappa_{\rm c}|} (-1)^{j_n + j_{\rm c} + \lambda} \right). \tag{2.18}$$

The result of the target structure calculations is a set of wave functions $\{\phi^N_n\}$ and corresponding energies ϵ^N_n, $n = 1, ..., N = \sum_\kappa N_\kappa$, that describe

the target atom or ion and satisfy

$$\langle \phi_m^N | H_{\rm T} | \phi_n^N \rangle = \epsilon_n^N \delta_{m,n}. \tag{2.19}$$

2.3 Relativistic scattering formulation

We now turn to the formulation of the relativistic scattering problem. This formulation is similar to the nonrelativistic case and we present here only the main results with emphasis on the differences with the nonrelativistic case [27]. In what follows we use index "1" to describe the projectile electron coordinates and index "2" for the target electron coordinates.

The Dirac Hamiltonian describing the total projectile electron and target scattering system is given by

$$H = H_1 + H_2 + V_{12}, \tag{2.20}$$

where $H_i = K_i + V_i$, with K_i denoting the free Dirac Hamiltonian and $V_i = V_i^{\rm FC} + V_i^{\rm pol}$ denoting the interaction potential of electron i with the closed frozen core as described in the previous section. We note that with this notation $H_{\rm T} = H_2$ and $V_{\rm T} = V_2$. The potential V_{12} denotes the Coulomb electron-electron potential. Generalization to the Breit and Møller potentials will be discussed in the next chapter.

The total scattering wave function satisfies

$$(E - H)|\Psi_i^{(+)}\rangle = 0, \tag{2.21}$$

where the superscript $(+)$ denotes the incoming plane-wave or Coulomb-wave and outgoing spherical-wave boundary conditions. The initial target state is ϕ_i and projectile wavenumber is k_i.

We use the set of target states $\{\phi_n^N\}$ to perform a multichannel expansion of the total wave function,

$$|\Psi_i^{N(+)}\rangle = \frac{1}{2}(1 - P_{12})|\psi_i^{N(+)}\rangle = \frac{1}{2}(1 - P_{12}) \sum_n |f_{n,i}^N \phi_n^N\rangle, \tag{2.22}$$

where $f_{n,i}^N$ are channel functions and P_{12} is the space exchange operator. The explicit antisymmetrization in Eq. (2.22) guarantees that the total wave

function satisfies the Pauli exclusion principle,

$$\langle x_1 x_2 | \Psi_i^{N(+)} \rangle = -\langle x_2 x_1 | \Psi_i^{N(+)} \rangle, \tag{2.23}$$

however it leads to nonunique channel functions $f_{n,i}^N$ and consequently to an ill defined set of scattering equations. Similarly to the nonrelativistic case[27] one can show that uniqueness of the total wave function can be ensured, without loss of generality, by imposing the following condition

$$\langle \phi_m^N | f_{n,i}^N \rangle = -\langle \phi_n^N | f_{m,i}^N \rangle. \tag{2.24}$$

We now turn to the derivation of the close-coupling equations. In the general case the charged target has asymptotic charge $Z_{\rm as}$, see Eq. (2.9), with the asymptotic Hamiltonian of the scattering system defined as

$$H_{\rm as} = K_1 - \frac{Z_{\rm as}}{r_1} + H_2. \tag{2.25}$$

The distorted-waves $|\boldsymbol{k}^{(\pm)}, \mu, b\rangle$ are solutions of the one-electron Dirac equation,

$$(\epsilon - K_1 + \frac{Z_{\rm as}}{r_1} - U_1)|\boldsymbol{k}^{(\pm)}, \mu, b\rangle = 0, \tag{2.26}$$

where U_1 is an arbitrary short-ranged distorting potential, μ is the spin magnetic number and b is the sign of energy, $\epsilon = \pm\epsilon_k = \pm c\sqrt{k^2 + c^2}$, with the positive sign corresponding to electrons and the negative sign to positrons (negative energy electrons). The Dirac distorted-waves satisfy the following orthogonality and completeness conditions,

$$\langle \boldsymbol{k}^{(\pm)} \mu b | \boldsymbol{k}'^{(\pm)} \mu' b' \rangle = \delta_{\mu,\mu'}\, \delta_{b,b'}\, \delta(\boldsymbol{k} - \boldsymbol{k}'), \tag{2.27}$$

$$\sum_{b\mu}\!\!\!\!\!\!\int d^3k |\boldsymbol{k}^{(\pm)} \mu' b' \rangle \langle \boldsymbol{k}^{(\pm)} \mu b| = \tilde{1}, \tag{2.28}$$

where $\tilde{1}$ denotes the unity 4×4 matrix.

Dirac distorted-waves reduce to standard Dirac plane-waves in the case of scattering from neutral targets and zero distorting potential and are given by [91]

$$|\boldsymbol{k}\mu b\rangle = U_\mu^b |\boldsymbol{k}\rangle = U_\mu^b \frac{1}{(2\pi)^{3/2}} e^{i\boldsymbol{k}\cdot\boldsymbol{r}}, \tag{2.29}$$

where the four-component spinors U_μ^b are

$$U_\mu^+ = \sqrt{\frac{\epsilon_k + c^2}{2\epsilon_k}} \begin{pmatrix} \chi_\mu \\ \frac{c\boldsymbol{\sigma}\cdot\boldsymbol{k}}{\epsilon_\kappa + c^2}\chi_\mu \end{pmatrix}, \quad U_\mu^- = \sqrt{\frac{\epsilon_k + c^2}{2\epsilon_k}} \begin{pmatrix} -\frac{c\boldsymbol{\sigma}\cdot\boldsymbol{k}}{\epsilon_k + c^2}\chi_\mu \\ \chi_\mu \end{pmatrix}. \quad (2.30)$$

Here $\boldsymbol{\sigma}$ consists of the Pauli matrices and χ_μ are two-component basis spinors.

The spectral decomposition of the Dirac Green's function,

$$G^{(\pm)}(E) = \sum_\mu \sum\!\!\!\!\!\!\int d^3k \left(\frac{|\boldsymbol{k}^{(\pm)}\mu+\rangle\langle\boldsymbol{k}^{(\pm)}\mu+|}{E - \epsilon_k \pm i0} + \frac{|\boldsymbol{k}^{(\pm)}\mu-\rangle\langle\boldsymbol{k}^{(\pm)}\mu-|}{E + \epsilon_k \pm i0} \right), \quad (2.31)$$

has now two terms corresponding to the positive energy and negative energy parts of the spectrum.

Substituting the expansion (2.22) in the Dirac equation (2.21) we obtain

$$(E - H_{\rm as} - U_1)|\psi_i^{N(+)}\rangle = (V_1 + \frac{Z_a}{r_1} - U_1 + V_{12} + [E - H]P_{12})|\psi_i^{N(+)}\rangle. \quad (2.32)$$

Using the Green's function (2.31) we can transform Eq. (2.32) to the momentum-space Lippmann-Schwinger equation,

$$\begin{aligned} |\psi_i^{N(+)}\rangle &= |\boldsymbol{k}_i^{(+)}\mu_i b_i \phi_i^N\rangle \\ &\quad + \sum_n \sum\!\!\!\!\!\!\int_{b,\mu} dk^3 \frac{|\boldsymbol{k}^{(-)}\mu b\phi_n\rangle\langle\boldsymbol{k}^{(-)}\mu b\phi_n^N|V_U|\psi_i^{N(+)}\rangle}{E - \epsilon_n^N - b\epsilon_k + i0}. \end{aligned} \quad (2.33)$$

Here $|\boldsymbol{k}^{(+)}\mu b\phi\rangle = |\boldsymbol{k}^{(+)}\mu b\rangle \times |\phi\rangle$ and

$$V_U^N = V_1 + \frac{Z_a}{r_1} - U_1 + V_{12} - E\theta I_1^N + [E(1-\theta) - H]\, P_{12}. \quad (2.34)$$

Any nonzero constant θ implements the condition (2.24), see Refs. [37] and [92] for details.

We premultiply Eq. (2.33) by $\langle\boldsymbol{k}_f^{(-)}\mu_f b_f \phi_f^N|V_U^N$ to obtain a set of Lippmann-Schwinger equations,

$$\begin{aligned} T_{fi}^{++}(\boldsymbol{k}_f^{(-)}\mu_f, \boldsymbol{k}_i^{(+)}\mu_i) &= V_{fi}^{++}(\boldsymbol{k}_f^{(-)}\mu_f, \boldsymbol{k}_i^{(+)}\mu_i) \\ &\quad + \sum_{n=1}^N \sum\!\!\!\!\!\!\int_\mu d^3k \frac{V_{fn}^{++}(\boldsymbol{k}_f^{(-)}\mu_f, \boldsymbol{k}^{(-)}\mu) T_{ni}^{++}(\boldsymbol{k}^{(-)}\mu, \boldsymbol{k}_i^{(+)}\mu_i)}{E - \epsilon_n - \epsilon_k + i0} \end{aligned}$$

$$+\sum_{n=1}^{N}\sum\!\!\!\!\!\!\int_{\mu} d^3k \frac{V_{fn}^{+-}(\boldsymbol{k}_f^{(-)}\mu_f,\boldsymbol{k}^{(-)}\mu)T_{ni}^{-+}(\boldsymbol{k}^{(-)}\mu,\boldsymbol{k}_i^{(+)}\mu_i)}{E-\epsilon_n+\epsilon_k+i0}, \tag{2.35}$$

$$\begin{aligned} T_{fi}^{-+}(\boldsymbol{k}_f^{(-)}\mu_f,\boldsymbol{k}_i^{(+)}\mu_i) &= V_{fi}^{-+}(\boldsymbol{k}_f^{(-)}\mu_f,\boldsymbol{k}_i^{(+)}\mu_i) \\ &+\sum_{n=1}^{N}\sum\!\!\!\!\!\!\int_{\mu} d^3k \frac{V_{fn}^{-+}(\boldsymbol{k}_f^{(-)}\mu_f,\boldsymbol{k}^{(+)}\mu)T_{ni}^{++}(\boldsymbol{k}^{(-)}\mu,\boldsymbol{k}_i^{(+)}\mu_i)}{E-\epsilon_n-\epsilon_k+i0} \\ &+\sum_{n=1}^{N}\sum\!\!\!\!\!\!\int_{\mu} d^3k \frac{V_{fn}^{--}(\boldsymbol{k}_f^{(-)}\mu_f,\boldsymbol{k}_\mu^{(-)})T_{ni}^{-+}(\boldsymbol{k}^{(-)}\mu,\boldsymbol{k}_i^{(+)}\mu_i)}{E-\epsilon_n+\epsilon_k+i0}, \end{aligned} \tag{2.36}$$

where the T-matrix elements are defined as

$$\begin{aligned} T_{fi}^{b_f b_i}(\boldsymbol{k}_f^{(-)}\mu_f,\boldsymbol{k}_i^{(+)}\mu_i) &= \langle \boldsymbol{k}_f^{(-)}\mu_f b_f \phi_f^N | T_U^N | \boldsymbol{k}_i^{(+)}\mu_i b_i \phi_i\rangle \\ &= \langle \boldsymbol{k}_f^{(-)}\mu_f b_f \phi_f^N | V_U^N | \psi_i^{(+)}\rangle \end{aligned} \tag{2.37}$$

and

$$V_{nn'}^{bb'}(\boldsymbol{k}^{(\pm)}\mu,\boldsymbol{k}'^{(\pm)}\mu') = \langle \boldsymbol{k}^{(\pm)}\mu b \phi_n^N | V_U^N | \boldsymbol{k}'^{(\pm)}\mu' b' \phi_{n'}^N\rangle. \tag{2.38}$$

For clarity we dropped N and U.

The T-matrix element $T_{ni}^{-+}(\boldsymbol{k}\mu,\boldsymbol{k}_i\mu_i)$ describes transition from a positive energy state to a negative energy state. The important feature of the Lippmann-Schwinger equation (2.36) is that the projectile electron negative energy states enter the equation only as virtual states. For a positive total energy E of the scattering system the Green's function associated with the negative energy term $T_{ni}^{-+}(\boldsymbol{k}\mu,\boldsymbol{k}_i\mu_i)$ has no singularity ($E-\epsilon_n+\epsilon_k>0$, i.e., we assume here that the energies of target bound states are much less than the electron rest energy) and therefore it describes closed states. In what follows we drop all negative energy terms in the Lippmann-Schwinger equation. For electron-atom/ion scattering processes the error associated with this approximation is negligible as the Green's function for the negative energy terms is of order $1/2c^2$. The resulting form of the Lippmann-Schwinger equation is the same as for the nonrelativistic case with transitions between positive energy states only, however it contains relativistic kinematics. Exclusion of the negative energy states in both target structure and scatter-

ing formulation is equivalent to the so-called no-virtual-pair approximation [72, 93].

The following choice for the distorting potential U has been used in our calculations,

$$U(r) = V^{\rm pol}(r) - \frac{N_{\rm c}+1}{r} + \sum_{\varphi_{\rm c}} \int d^3r' \frac{|\varphi_{\rm c}(\boldsymbol{r'})|^2}{|\boldsymbol{r}-\boldsymbol{r'}|} + \int d^3r' \frac{|\phi_n(\boldsymbol{r'})|^2}{|\boldsymbol{r}-\boldsymbol{r'}|}, \quad (2.39)$$

where we typically take ϕ_n to be the ground state. This choice leads to a short-ranged potential for neutral targets while at the same time it allows us to minimize the numerical problems arising from large Z/r terms in V-matrix elements. Finally, we note that similar to the nonrelativistic CCC method [37] the physical T-matrix ($U = 0$) can be extracted from the distorted-wave T-matrix via

$$\begin{aligned} \langle \boldsymbol{k}_f^{(-)}\mu_f + \phi_f^N | T | \boldsymbol{k}_i^{(+)}\mu_i + \phi_i \rangle &= \langle \boldsymbol{k}_f^{(-)}\mu_f + \phi_f^N | T_U | \boldsymbol{k}_i^{(+)}\mu_i + \phi_i \rangle \\ &+ \langle \boldsymbol{k}_f^{(-)}\mu_f + | U | \boldsymbol{k}_i^{(+)}\mu_i + \rangle \delta_{f,i}, \end{aligned} \quad (2.40)$$

where the absence of index U in the left-hand side indicates that the final T-matrix must be independent of the choice of this distorting potential.

2.4 Partial wave expansion

The Lippmann-Schwinger equation for the partial-wave T-matrix can be obtained from Eq. (2.36) by performing a partial-wave expansion of the T-matrix and V-matrix. In order to do this we need to specify a partial-wave representation of the (positive energy) Dirac distorted waves [94]

$$|\boldsymbol{k}^{(\pm)}\mu+\rangle = \sqrt{\frac{\epsilon_k + c^2}{\pi \epsilon_k}} \sum_{\kappa,m} i^L C^{jm}_{Lm-\mu,\frac{1}{2}\mu} Y_L^{*m-\mu}(\boldsymbol{k}) e^{\pm i(\sigma_\kappa+\delta_\kappa)} \frac{1}{kr} |u^m_{\kappa,k}\rangle, \quad (2.41)$$

where $C^{jm}_{j_1 m_1, j_2 m_2}$ is a Clebsch-Gordan coefficient, σ_κ is the Dirac-Coulomb phase shift, δ_κ is the distorted-wave phase shift, $j = |\kappa| - 1/2$ and

$$\langle \boldsymbol{r} | u^m_{\kappa,k} \rangle = \begin{pmatrix} u^{\rm L}_{k\kappa}(r)\chi_{\kappa m} \\ i u^{\rm S}_{k\kappa}(r)\chi_{-\kappa m} \end{pmatrix}. \quad (2.42)$$

The radial functions $u^{\mathrm{L/S}}_{k\kappa}(r)$ are calculated numerically using an Adams-Moulton predictor-corrector integration method as described by Sienkiewicz and Baylis [95]. In (2.41) the normalization of the radial function $u^{\mathrm{L/S}}_{k\kappa}(r)$ is chosen such that at large values of r the radial function oscillates with unit amplitude and has the following asymptotic form

$$u^{\mathrm{L/S}}_{k\kappa}(r) \quad \sim \quad \cos(\delta_\kappa)F^{\mathrm{L/S}}_{\kappa}(kr) + \sin(\delta_\kappa)G^{\mathrm{L/S}}_{\kappa}(kr), \tag{2.43}$$

where $F^{\mathrm{L/S}}$ and $G^{\mathrm{L/S}}$ are the regular and irregular Dirac-Coulomb functions respectively. We use the program DCOUL of Salvat et al. [96] to calculate Dirac-Coulomb phase shifts σ_κ. The same program is also used to find values of the Dirac-Coulomb functions in the asymptotic region ($U = 0$) in order to determine distorted wave phase shifts δ_κ and to choose the correct normalization of the $u^{\mathrm{L/S}}_{k\kappa}(r)$ functions.

The partial-wave expansion of the V and T-matrix can now be defined as

$$\begin{aligned}
\langle k^{(-)}\kappa, n : \Pi J|V|k^{'(+)}\kappa', n' : \Pi J\rangle \quad &= \quad \sum_{M\mu m_n M'\mu' m_{n'}} C^{jm_j}_{LM,\frac{1}{2}\mu} C^{j'm'_j}_{L'M',\frac{1}{2}\mu'} \\
&\times \quad C^{JM_J}_{jm_j,j_n m_n} C^{JM_J}_{j'm'_j,j_{n'}m_{n'}} \\
&\times \quad \int d\boldsymbol{k} \int d\boldsymbol{k}' Y^{*M}_{L}(\boldsymbol{k}) Y^{M'}_{L'}(\boldsymbol{k}') \\
&\times \quad \langle \boldsymbol{k}^{(-)}\mu+, \phi^N_n|V|\boldsymbol{k}^{'(+)}\mu'+, \phi^N_{n'}\rangle,
\end{aligned} \tag{2.44}$$

where J and M_J are the total angular momentum of the scattering system and its projection, $\Pi = \pi(-1)^L = \pi'(-1)^{L'}$ is the total parity and $|k\kappa, n : \Pi J\rangle$ stands for the angular momentum coupled projectile-target wave function. The partial-wave V-matrix (2.44) is complex, but a real quantity can be defined via

$$V^{\Pi J}_{n,n'}(k\kappa, k'\kappa') = (i)^L(-i)^{L'}e^{-i\eta}e^{-i\eta'}\langle k^{(-)}\kappa, n : \Pi J|V|k^{'(+)}\kappa', n' : \Pi J\rangle, \tag{2.45}$$

where $\eta_\kappa = \sigma_\kappa + \delta_\kappa$. The V-matrix elements (2.45) can be easily evaluated using standard techniques of relativistic atomic structure [72, 90]. Adopting for the partial-wave T-matrix the same definition as in (2.45) the Lippmann-

Schwinger equation (2.36) reduces to the following partial wave form,

$$\begin{aligned} T_{fi}^{\Pi J}(k_f\kappa_f, k_i\kappa_i) &= V_{fi}^{\Pi J}(k_f\kappa_f, k_i\kappa_i) \\ &+ \sum_n \sum_\kappa \!\!\!\!\!\!\int dk \frac{V_{fn}^{\Pi J}(k_f\kappa_f, k\kappa) T_{ni}^{\Pi J}(k\kappa, k_i\kappa_i)}{E - \epsilon_n^N - \epsilon_{k'} + i0}. \end{aligned} \tag{2.46}$$

Appendix B contains the complete derivation. This equation can be solved numerically using complex arithmetic. However, we find it more convenient to define a real K-matrix and solve the corresponding set of equations in real arithmetic. The transformation from the complex T-matrix to real K-matrix is similar to the nonrelativistic case,

$$\begin{aligned} K_{ni}^{\Pi J}(k_n\kappa, k_i\kappa_i) &= \sum_{\kappa'} \sum_{n'=1}^{N_o} T_{nn'}^{\Pi J}(k_n\kappa, k_{n'}\kappa') \\ &\times \left(\delta_{n',i}\delta_{\kappa',\kappa_i} + i\pi\mu_{n'} K_{n'i}^{\Pi J}(k_{n'}\kappa', k_i\kappa_i)\right), \end{aligned} \tag{2.47}$$

where N_o specifies the number of open channels for which $\epsilon_{k_n} = E - \epsilon_n > 0$ and

$$\mu_n = k_n \frac{\epsilon_{k_n}}{c^2}. \tag{2.48}$$

The difference compared to the nonrelativistic result ($\mu_n = k_n$) comes from the difference in the relation between energy and momentum in relativistic and nonrelativistic theory. The Lippmann-Schwinger equation for the K matrix can be written as

$$\begin{aligned} K_{fi}^{\Pi J}(k_f\kappa_f, k_i\kappa_i) &= V_{fi}^{\Pi J}(k_f\kappa_f, k_i\kappa_i) \\ &+ \sum_n \sum_\kappa \mathcal{P} \!\!\!\!\!\!\int dk \frac{V_{fn}^{\Pi J}(k_f\kappa_f, k\kappa) K_{ni}^{\Pi J}(k\kappa, k_i\kappa_i)}{E - \epsilon_n^N - \epsilon_{k'}}, \end{aligned} \tag{2.49}$$

where $\mathcal{P}$ stands for a principal-value integral. The V-matrix in the above equation is real and symmetric which leads to the real and symmetric K-matrix.

The important advantage of obtaining the T-matrix via Eq. (2.47) is

that the resultant T-matrix is symmetric and unitary by construction,

$$\mathrm{Im}(T_{fi}^{\Pi J}(k_f\kappa_f, k_i\kappa_i)) = -\pi \sum_n \sum_{\kappa_n} \mu_n T_{fn}^{*\Pi J}(k_f\kappa_f, k_n\kappa_n) T_{ni}^{\Pi J}(k_n\kappa_n, k_i\kappa_i). \tag{2.50}$$

The coupled set of integral equations (2.49) is solved for each value of total parity Π and angular momentum J by replacing integration over momentum by a quadrature rule. The choice of quadrature rule and reduction to the set of linear equations is practically the same as in the nonrelativistic CCC method [27, 37].

2.5 Scattering amplitude and cross section

We define the scattering amplitude $F_{fi}^{\mu_f\mu_i}(\theta)$ in the collision frame (z-axis is along the incident momentum of the projectile, θ is the angle between scattered electron momentum and z axis) for a transition from a state ϕ_i with parity π_i, angular momentum j_i, its projection m_i to a state ϕ_f with parity π_f, angular momentum j_f, its projection m_f as

$$\begin{aligned} F_{m_f m_i}^{\mu_f\mu_i}(\theta) &= -\sum_{\kappa_f\kappa_i J\Pi} i^{L_i - L_f} e^{\eta_{\kappa_f} + \eta_{\kappa_i}} C^{jm_j}_{L_f M_f, \frac{1}{2}\mu_f} C^{j'\mu_i}_{L_i 0, \frac{1}{2}\mu_i} C^{JM_J}_{jm_j, j_f m_f} C^{JM_J}_{j'\mu_i, j_i m_i} \\ &\quad \times Y_{L_f}^{M_f}(\boldsymbol{k}_f) \sqrt{\frac{2L_i+1}{4\pi}} T_{fi}^{\Pi J}(k_f\kappa_f, k_i\kappa_i), \end{aligned} \tag{2.51}$$

where $m_j = m_i + \mu_i - m_f$ and $M_f = m_j - \mu_f$.

The differential cross section corresponding to the transition described by the scattering amplitude (2.51) for the case of unpolarized target atom and electron beams can be obtained as

$$\frac{d\sigma_{fi}}{d\Omega} = (2\pi)^4 \frac{k_f}{k_i} \frac{\epsilon_f \epsilon_i}{c^4} \frac{1}{2(2j_i+1)} \sum_{\mu_f\mu_i m_f m_i} |F_{m_f m_i}^{\mu_f\mu_i}(\theta)|^2. \tag{2.52}$$

Compared to the nonrelativistic case it has an additional term $\epsilon_f\epsilon_i/c^4$ which appears due to the relativistic relationship between the velocity and momentum [97]. Appendix C contains the derivation of the expression for the relativistic cross section in which this extra kinematical factor appears.

The cross section integrated over electron scattering angles is given by

$$\sigma_{fi} = \int d\Omega \frac{d\sigma_{fi}}{d\Omega} = \sum_{J\Pi} \sigma_{fi}^{J\Pi}, \tag{2.53}$$

where the partial-wave integrated cross sections $\sigma_{fi}^{J\Pi}$ can be expressed via the partial-wave T-matrix as

$$\sigma_{fi}^{J\Pi} = (2\pi)^4 \frac{k_f}{k_i} \frac{\epsilon_f \epsilon_i}{c^4} \frac{1}{2(2j_i+1)} \frac{2J+1}{4\pi} \sum_{\kappa_f \kappa_i} |T_{fi}^{\Pi J}(k_f \kappa_f, k_i \kappa_i)|^2. \tag{2.54}$$

The derivation of this equation is given in Appendix D.

For scattering from neutral targets the unitarity of the T-matrix (2.50) leads to the optical theorem that relates the elastic forward scattering amplitude and total scattering cross section for a target atom in the initial state with magnetic sublevel m_i and incident electron with spin projection μ_i,

$$\sigma_{m_i\mu_i}^{\rm tot} = \sum_f \sigma_{m_i\mu_i}^f = (2\pi)^4 \frac{1}{k_i} \frac{\epsilon_i}{c^2} \frac{1}{\pi} {\rm Im}(F_{m_i m_i}^{\mu_i \mu_i}(0)), \tag{2.55}$$

where

$$\sigma_{m_i\mu_i}^f = (2\pi)^4 \frac{k_f}{k_i} \frac{\epsilon_f \epsilon_i}{c^4} \sum_{\mu_f m_f} \int d\Omega |F_{m_f m_i}^{\mu_f \mu_i}(\theta)|^2. \tag{2.56}$$

The spin-averaged cross section describing transitions between magnetic sublevels is defined as

$$\sigma_{m_f m_i} = (2\pi)^4 \frac{k_f}{k_i} \frac{\epsilon_f \epsilon_i}{c^4} \frac{1}{2} \sum_{\mu_f \mu_i} |F_{m_f m_i}^{\mu_f \mu_i}(\theta)|^2. \tag{2.57}$$

Averaging over initial magnetic sublevels we obtain the cross section for excitation of a particular magnetic sublevel

$$\sigma_{m_f} = \frac{1}{2j_i+1} \sum_{m_i} \sigma_{m_f m_i}. \tag{2.58}$$

Summing over final magnetic sublevels we obtain the standard integrated cross section

$$\sigma_{fi} = \frac{1}{2j_i+1} \sum_{m_f m_i} \sigma_{m_f m_i}. \tag{2.59}$$

2.6 Spin assymetry parameters

Scattering of polarized electrons from polarized atoms has been studied in a series of experiments [98]. These experiments measured the scattered electron intensities for all four possible combinations of relative polarization (with respect to the scattering plane) of incident electron (up or down) and target atom (up and down). This makes it possible to determine the DCS for scattering of unpolarized electrons and target atoms, as well as three spin asymmetries describing scattering of unpolarized electrons from polarized atoms (A_1), polarized electrons from unpolarized atoms (A_2), and 'antiparallel-parallel' asymmetry (A_{nn}) for scattering of polarized electrons from polarized atoms. Asymmetries A_1 and A_2 are zero in nonrelativistic calculations and offer a sensitive test to account for relativistic effects in theoretical models. We also note that all spin asymmetries are zero when calculated in the first Born approximation providing, therefore, a test for importance of channel coupling in electron scattering from atoms/ions.

The spin asymmetry parameters A_i can be expressed in terms of differential cross sections in the following way [99],

$$A_1 = \left[q\left(\frac{1}{2},\frac{1}{2}\right) + q\left(\frac{1}{2},-\frac{1}{2}\right) - q\left(-\frac{1}{2},\frac{1}{2}\right) - q\left(-\frac{1}{2},-\frac{1}{2}\right)\right]/4q_u, \quad (2.60)$$

$$A_2 = \left[q\left(\frac{1}{2},\frac{1}{2}\right) + q\left(-\frac{1}{2},\frac{1}{2}\right) - q\left(\frac{1}{2},-\frac{1}{2}\right) - q\left(-\frac{1}{2},-\frac{1}{2}\right)\right]/4q_u, \quad (2.61)$$

$$A_{nn} = \left[q\left(\frac{1}{2},-\frac{1}{2}\right) + q\left(-\frac{1}{2},\frac{1}{2}\right) - q\left(\frac{1}{2},\frac{1}{2}\right) - q\left(-\frac{1}{2},-\frac{1}{2}\right)\right]/4q_u, \quad (2.62)$$

where the magnetic sublevel DCS is defined as

$$q\left(m_i\mu_i\right) = (2\pi)^4 \frac{k_f}{k_i}\frac{\epsilon_f\epsilon_i}{c^4}\sum_{\mu_f m_f}|F^{\mu_f\mu_i}_{m_f m_i}(\theta)|^2, \quad (2.63)$$

with

$$q_u(\theta) = \frac{d\sigma}{d\Omega} = \frac{1}{4}\left[q\left(\frac{1}{2},-\frac{1}{2}\right) + q\left(-\frac{1}{2},\frac{1}{2}\right) + q\left(\frac{1}{2},\frac{1}{2}\right) + q\left(-\frac{1}{2},-\frac{1}{2}\right)\right]. \quad (2.64)$$

2.7 Scattering amplitude and the analytical Born subtraction technique

In any practical calculation the partial-wave expansion has to be terminated at some value of total angular momentum $J_{\max}$. At high incident electron energies the $J_{\max}$ value has to be sufficiently large in order to achieve convergence in the partial wave-expansion. We can use the analytical Born subtraction technique to reduce the size of the partial-wave expansion. This technique has been widely used in nonrelativistic electron-atom scattering methods, see for example Inokuti [100]. It is probably less common in the relativistic techniques though recently Fontes and Zhang [101] provided a useful review of it. The analytical Born subtraction technique relies on the property that at large values of total angular momentum J the partial-wave T-matrix becomes equal to the partial-wave V-matrix,

$$T^{\Pi J}_{fi}(k_f\kappa_f, k_i\kappa_i) = \tilde{V}^{\Pi J}_{fi}(k_f\kappa_f, k_i\kappa_i), \tag{2.65}$$

where the partial-wave $\tilde{V}$-matrix is calculated with the direct only part of the potential (2.34),

$$\tilde{V} = V_1 + \frac{Z_{\rm as}}{r_1} + V_{12}, \tag{2.66}$$

using Dirac plane-waves (2.29). This is equivalent to calculating the T-matrix in the first-order Born approximation (FBA) for the large J values. The above expression holds for scattering from both neutral and charged targets as the centrifugal term becomes dominant at large values of J.

In order to take advantage of the relation (2.65) we redefine the scattering amplitude (2.51) as

$$\begin{aligned} F^{\mu_f\mu_i}_{m_f m_i}(\theta) \;=\; & -\sum_{\kappa_f\kappa_i J\Pi} C^{jm_j}_{L_fM_f,\frac{1}{2}\mu_f} C^{j'\mu_i}_{L_i0,\frac{1}{2}\mu_i} C^{JM_J}_{jm_j,j_fm_f} C^{JM_J}_{j'\mu_i,j_im_i} \\ & \times i^{L_i-L_f} e^{\eta_{\kappa_f}+\eta_{\kappa_i}} Y^{M_f}_{L_f}(\boldsymbol{k}_f)\sqrt{\frac{2L_i+1}{4\pi}} \\ & \times \left(T^{\Pi J}_{fi}(k_f\kappa_f, k_i\kappa_i) - V^{\Pi J}_{fi}(k_f\kappa_f, k_i\kappa_i)\right) \\ & -\langle \boldsymbol{k}_f\mu_f+, \phi_f|\tilde{V}|k_i\mu_i+, \phi_i\rangle. \end{aligned} \tag{2.67}$$

Calculation of cross sections and other scattering parameters discussed in the previous section with use of the amplitude (2.67) normally does not require

a large partial wave expansion, leading to substantial saving in computer time.

Calculation of the scattering amplitude via Eq. (2.67) requires evaluation of the FBA plane-wave V-matrix which can be done using the expressions for the Dirac plane-waves (2.29),

$$\langle \boldsymbol{k}_f \mu_f +, \phi_f | \tilde{V} | \boldsymbol{k}_i \mu_i +, \phi_i \rangle = A_{\mu_f \mu_i}(\theta) \frac{1}{(2\pi)^3} \frac{4\pi}{q^2} R_{m_f m_i}(\theta), \quad (2.68)$$

where $\boldsymbol{q} = \boldsymbol{k}_i - \boldsymbol{k}_f$ is the momentum transfer,

$$R_{m_f m_i}(\theta) = \langle \phi_f | e^{i\boldsymbol{q}\cdot\boldsymbol{r}} | \phi_i \rangle - \delta_{f,i} \left[1 - \int d^3 r_1 e^{i\boldsymbol{q}\cdot\boldsymbol{r}} \left(V_d^{\mathrm{FC}}(r) + \frac{Z_{\mathrm{as}} + 1}{r} \right) \right], \quad (2.69)$$

$$\begin{aligned} A_{\mu_f \mu_i}(\theta) = U_{\mu_f}^{+\dagger} U_{\mu_i}^{+} &= N_{fi} \left[\delta_{\mu_f, \mu_i} \left(1 + \frac{c^2 k_i k_f \cos\theta}{(\epsilon_f + c^2)(\epsilon_i + c^2)} \right) \right. \\ &+ \left. \delta_{-\mu_f, \mu_i} \frac{2\mu_f c^2 k_i k_f \sin\theta}{(\epsilon_f + c^2)(\epsilon_i + c^2)} \right] \end{aligned} \quad (2.70)$$

and

$$N_{fi} = \sqrt{\left(\frac{\epsilon_i + c^2}{2\epsilon_i} \right) \left(\frac{\epsilon_f + c^2}{2\epsilon_f} \right)}. \quad (2.71)$$

The differential cross section (DCS) calculated using the FBA amplitude leads to

$$\frac{d\sigma_{fi}^{\mathrm{FBA}}}{d\Omega} = \frac{k_f}{k_i} \frac{\epsilon_f \epsilon_i}{c^4} \frac{1}{2j_i + 1} \frac{4}{q^4} \sum_{m_f m_i} |R_{m_f m_i}(\theta)|^2 \sum_{\mu_f \mu_i} \frac{1}{2} A_{\mu_f \mu_i}(\theta), \quad (2.72)$$

with

$$\sum_{\mu_f \mu_i} \frac{1}{2} A_{\mu_f \mu_i}(\theta) = \frac{1}{2\epsilon_f \epsilon_i} \left(\epsilon_f \epsilon_i + c^4 + c^2 k_f k_i \cos\theta \right). \quad (2.73)$$

In the case of elastic scattering, $k_f = k_i$, the last expression leads to the well known Mott elastic scattering formula.

Calculation of the FBA integrated cross sections

$$\sigma_{fi}^{\mathrm{FBA}} = \int d\Omega \frac{d\sigma_{fi}^{\mathrm{FBA}}}{d\Omega}, \quad (2.74)$$

allows for an alternative implementation of the analytical Born subtraction

technique for integrated cross sections that does not require evaluation of the scattering amplitude (2.67). This can be achieved by adopting the following expression for integrated cross sections

$$\sigma_{fi} = \sum_{J\Pi} \left(\sigma_{fi}^{J\Pi} - \sigma_{fi}^{J\Pi,\mathrm{FBA}} \right) + \sigma_{fi}^{\mathrm{FBA}}, \tag{2.75}$$

where $\sigma_{fi}^{J\Pi,\mathrm{FBA}}$ is defined as in Eq. (2.54) but with $\tilde{V}_{fi}^{\Pi J}(k_f\kappa_f, k_i\kappa_i)$ matrix elements.

Chapter 3

Inclusion of the Breit and Møller interactions

In this Chapter we present the theory required to include the Breit and Møller interactions in the RCCC method for electron scattering on highly charged hydrogenlike ions. We apply the method by calculating the polarization of the Lyman-α_1 x-ray line emitted by hydrogenlike Ti^{21+}, Ar^{17+} and Fe^{25+} ions excited by electron impact. We find that account of Breit relativistic corrections is important to resolve the discrepancy between experiment and theoretical calculations. For the much heavier hydrogenlike U^{91+} ion where the Møller interaction becomes important we present the estimate of the polarization of the Lyman-α_1 x-ray line and performed calculation of the total ionization cross section.

3.1 The Breit and Møller interactions

In 1929 Breit [102–104] used classical arguments to include relativistic corrections to the Coulomb potential in helium fine structure calculations. In the Coulomb gauge the Breit interaction is of the form

$$V_{12}^{\mathrm{B}} = \frac{e^2}{r_{12}}[-\boldsymbol{\alpha}_1 \cdot \boldsymbol{\alpha}_2 + \frac{1}{2}(\boldsymbol{\alpha}_1 \cdot \boldsymbol{p}_1 \boldsymbol{\alpha}_2 \cdot \boldsymbol{p}_2) r_{12}^2]. \tag{3.1}$$

In the above potential the first term on the right hand side can be interpreted as a "magnetic" interaction between electron spins, and the second term on the right hand side can be interpreted as a "retardation" term due to the

finite propagation time of the interaction between the electrons.

Møller [105], in 1932, considered the scattering of fast electrons and derived a more general expression for the relativistic interaction between electrons. In the Lorentz gauge the Møller interaction takes the form [106]

$$V_{12}^{\mathrm{M}} = \frac{e^2}{r_{12}}(1 - \boldsymbol{\alpha}_1 \cdot \boldsymbol{\alpha}_2)\mathrm{e}^{iKr_{12}}, \tag{3.2}$$

where $K = |E - E'|/c$, and E and E' denote the initial and final energies of one of the electrons. The form of the interaction is different if the Coulomb gauge is used, however Hata and Grant [107] have shown that the Lorentz and Coulomb gauge forms for the interaction have equivalent matrix elements provided the wave functions used are derived from a local potential, which is the situation for electron scattering from hydrogenlike ions. The Møller interaction incorporates both the Coulomb interaction and all relativistic corrections, whereas the Breit interaction given by Eq. (3.1) must be added to the Coulomb potential. The Møller interaction depends on the energy transferred between the electrons and in the limit of low energy transfer it reduces to the Coulomb plus Breit interaction [106].

The matrix elements of the Coulomb, Breit and Møller interactions have been given by Grant [90] and expressed in a convenient form for computation by Walker [108]. The calculation of the matrix elements of the Møller interaction,

$$\langle ABJM|\frac{e^2}{r_{12}}(1 - \boldsymbol{\alpha}_1 \cdot \boldsymbol{\alpha}_2)\mathrm{e}^{iKr_{12}}|CDJ'M'\rangle, \tag{3.3}$$

requires the identity

$$\frac{\mathrm{e}^{iKr_{12}}}{r_{12}} = iK\sum_{\nu=0}^{\infty}(2\nu+1)j_\nu(Kr_<)(n_\nu(Kr_>) - ij_\nu(Kr_>))\boldsymbol{C}^\nu(1)\cdot\boldsymbol{C}^\nu(2), \tag{3.4}$$

where $j_\nu(Kr_<)$ and $n_\nu(Kr_>)$ are spherical Bessel and Neumann functions [109], and $r_<, r_>$ specify the lesser and greater of r_1 and r_2 respectively. For the on-shell matrix elements $K = |E_C - E_A|/c = |E_D - E_B|/c$. In performing full RCCC calculations we require off-shell V-matrix elements and to obtain these we follow the method outlined by Hata and Grant [107],

$$V_{12}^{\mathrm{M}} = 1/2\left(V_{12}^{\mathrm{M}}(K_{AC}) + V_{12}^{\mathrm{M}}(K_{BD})\right), \tag{3.5}$$

where $K_{AC} = |E_C - E_A|/c$ and $K_{BD} = |E_D - E_B|/c$.

Fontes et al. [1] have performed calculations that show that the effect of dropping the imaginary part in Eq.(3.4) is negligible and is of the order of 2-3% for $1s - 2s$, $1s - 2p_{1/2}$, and $1s - 2p_{3/2}$ excitation cross sections for a very highly charged Z=100 hydrogenlike target. Thus only the real part of the Møller interaction may then be used.

3.2 Matrix elements of the Coulomb, Breit and Møller interactions

Using the identity

$$\frac{1}{r_{12}} = \frac{1}{|\boldsymbol{r}_1 - \boldsymbol{r}_2|} = \sum_{\nu=0}^{\infty} \frac{r_<^\nu}{r_>^{\nu+1}} \boldsymbol{C}^\nu(1) \cdot \boldsymbol{C}^\nu(2), \tag{3.6}$$

the matrix elements of the Coulomb interaction are given by

$$\begin{aligned} V_{12_C} &= \langle ABJM | \frac{e^2}{r_{12}} | CDJ'M' \rangle \\ &= \delta_{JJ'}\delta_{MM'} \sum_{\nu=0}^{\infty} M_C^\nu(ABCD; JM) R_C^\nu(ABCD), \end{aligned} \tag{3.7}$$

where

$$\begin{aligned} M_C^\nu(ABCD; JM) &= [j_A, j_B, j_C, j_D]^{1/2} \begin{pmatrix} j_A & \nu & j_C \\ \frac{1}{2} & 0 & -\frac{1}{2} \end{pmatrix} \\ &\times \begin{pmatrix} j_D & \nu & j_B \\ \frac{1}{2} & 0 & -\frac{1}{2} \end{pmatrix} \begin{Bmatrix} j_A & j_D & J \\ J_B & j_A & \nu \end{Bmatrix} \end{aligned} \tag{3.8}$$

and

$$\begin{aligned} R_C^\nu(ABCD) &= e^2 \int_0^\infty \int_0^\infty \frac{r_<^\nu}{r_>^{\nu+1}} [P_A(1)P_C(1) + Q_A(1)Q_C(1)] \mathrm{d}r_1 \\ &\times [P_B(2)P_D(2) + Q_B(2)Q_D(2)] \mathrm{d}r_2. \end{aligned} \tag{3.9}$$

The following notation is used

$$\begin{aligned} j &= l + \frac{1}{2}\alpha, \qquad \alpha = \pm 1, \\ [j] &= (2j+1), \end{aligned} \tag{3.10}$$

and following selection rules apply

$$\begin{aligned} &j_A + j_C + \nu \quad \text{is odd if } \alpha_{\rm A} = \alpha_{\rm C}, \text{ even if } \alpha_{\rm A} \neq \alpha_{\rm C}, \\ &j_B + j_D + \nu \quad \text{is odd if } \alpha_{\rm B} = \alpha_{\rm D}, \text{ even if } \alpha_{\rm B} \neq \alpha_{\rm D}. \end{aligned} \tag{3.11}$$

3.2.1 Two body Breit magnetic

The matrix elements of the "magnetic" part of the Breit interaction are given by

$$\begin{aligned} V_{12_M} &= \langle ABJM| \frac{-e^2}{r_{12}} \boldsymbol{\alpha}_1 \cdot \boldsymbol{\alpha}_2 |CDJ'M'\rangle \\ &= \delta_{JJ'}\delta_{MM'} \sum_{\nu\beta\beta'}^{\infty} M_M^{\nu\beta\beta'}(ABCD;JM) R_M^{\nu}(A\beta, B-\beta', C-\beta, D\beta'), \end{aligned} \tag{3.12}$$

where

$$\begin{aligned} M_M^{\nu\beta\beta'}(ABCD;JM) &= 6\beta\beta'(-1)^{j_C+j_D+J-1+\lambda_B+\lambda_C} \\ &\times [j_A, j_B, j_C, j_D, \lambda_A, \lambda_B, \lambda_C, \lambda_D]^{1/2} \\ &\times \begin{pmatrix} \lambda_A & \nu & \lambda_C \\ 0 & 0 & 0 \end{pmatrix} \begin{pmatrix} \lambda_D & \nu & \lambda_B \\ 0 & 0 & 0 \end{pmatrix} \\ &\times \sum_L [L] \begin{Bmatrix} j_C & j_D & J \\ j_B & j_A & \nu \end{Bmatrix} \begin{Bmatrix} \lambda_A & \lambda_C & \nu \\ \frac{1}{2} & \frac{1}{2} & 1 \\ j_A & j_C & L \end{Bmatrix} \\ &\times \begin{Bmatrix} \lambda_D & \lambda_B & \nu \\ \frac{1}{2} & \frac{1}{2} & 1 \\ j_D & j_B & L \end{Bmatrix} \end{aligned} \tag{3.13}$$

and

$$\begin{aligned} R_M^{\nu}(A\beta, B-\beta', C-\beta, D\beta') &= e^2 \int_0^{\infty}\int_0^{\infty} \frac{r_<^{\nu}}{r_>^{\nu+1}} \\ &\times R_{A\beta_A}(1) R_{B\beta_B}(2) R_{C\beta_C}(1) R_{D\beta_D}(2) \mathrm{d}r_1 \mathrm{d}r_2, \end{aligned} \tag{3.14}$$

with $\lambda_A = j_A - \frac{1}{2}\alpha_A\beta$, $\lambda_B = j_B + \frac{1}{2}\alpha_B\beta'$, $\lambda_C = j_C + \frac{1}{2}\alpha_C\beta$ and $\lambda_D = j_D - \frac{1}{2}\alpha_D\beta'$, with $\beta = \pm 1$ specifying the upper ($\beta = +1$) and lower ($\beta = -1$) components of the wave-function.

3.2.2 Two body Breit retarded

The matrix elements of the "retarded" part of the Breit interaction are given by

$$\begin{aligned} V_{12_R} &= \langle ABJM|\frac{1}{2}e^2(\boldsymbol{\alpha}_1\cdot\boldsymbol{p}_1\boldsymbol{\alpha}_2\cdot\boldsymbol{p}_2)r_{12}|CDJ'M'\rangle \\ &= \delta_{JJ'}\delta_{MM'}\sum_{\nu\nu' L\beta\beta'}^{\infty} M_R^{\nu'\nu L\beta\beta'}(ABCD;JM) \\ &\times \; R_R^{\nu\nu' L}(A\beta, B-\beta', C-\beta, D\beta'), \end{aligned} \tag{3.15}$$

where

$$\begin{aligned} M_R^{\nu}(ABCD;JM) &= 3\beta\beta'(-1)^{j_C+j_D+J-1+\lambda_B+\lambda_C} \\ &\times \; [j_A, j_B, j_C, j_D, \lambda_A, \lambda_B, \lambda_C, \lambda_D]^{1/2}[\nu,\nu'] \\ &\times \; \begin{pmatrix} 1 & \nu & L \\ 0 & 0 & 0 \end{pmatrix}\begin{pmatrix} 1 & \nu' & L \\ 0 & 0 & 0 \end{pmatrix} \\ &\times \; \begin{pmatrix} \lambda_A & \nu & \lambda_C \\ 0 & 0 & 0 \end{pmatrix}\begin{pmatrix} \lambda_D & \nu & \lambda_B \\ 0 & 0 & 0 \end{pmatrix} \\ &\times \; \begin{Bmatrix} j_C & j_D & J \\ j_B & j_A & \nu \end{Bmatrix} \\ &\times \; \begin{Bmatrix} \lambda_A & \lambda_C & \nu \\ \frac{1}{2} & \frac{1}{2} & 1 \\ j_A & j_C & L \end{Bmatrix}\begin{Bmatrix} \lambda_D & \lambda_B & \nu \\ \frac{1}{2} & \frac{1}{2} & 1 \\ j_D & j_B & L \end{Bmatrix} \end{aligned} \tag{3.16}$$

and

$$\begin{aligned} R_R^{\nu\nu L}(A\beta, B-\beta', C-\beta, D\beta') &= e^2\int_0^{\infty}\int_0^{\infty} W_{\nu\nu' L}(1,2) \\ &\times \; R_{A\beta_A}(1)R_{B\beta_B}(2)R_{C\beta_C}(1)R_{D\beta_D}(2)\mathrm{d}r_1\mathrm{d}r_2, \end{aligned} \tag{3.17}$$

with

$$\begin{aligned} W_{\nu,\nu,L}(1,2) &= -2\frac{[L]}{[\nu]}\frac{r_<^\nu}{r_>^{\nu+1}} \qquad (\nu = L-1, L+1) \\ W_{L-1,L+1L}(1,2) &= -[L]\left(\frac{r_1^{L+1}}{r_2^{L+2}} - \frac{r_1^{L-1}}{r_2^{L}}\right) \qquad (r_1 < r_2) \\ &= 0 \qquad (r_1 > r_2) \\ W_{L-1,L+1L}(1,2) &= W_{L-1,L+1,L}(2,1). \end{aligned} \tag{3.18}$$

Note we have as before, $\lambda_A = j_A - \frac{1}{2}\alpha_A\beta$, $\lambda_B = j_B + \frac{1}{2}\alpha_B\beta'$, $\lambda_C = j_C + \frac{1}{2}\alpha_C\beta$ and $\lambda_D = j_D - \frac{1}{2}\alpha_D\beta'$, with $\beta = \pm 1$ specifying the upper ($\beta = +1$) and lower ($\beta = -1$) components of the wave-function.

3.2.3 Møller interaction

The matrix elements of the Møller interaction, Eq.(3.2),

$$V_{12\text{Møller}} = \langle ABJM|\frac{e^2}{r_{12}}(1 - \boldsymbol{\alpha}_1 \cdot \boldsymbol{\alpha}_2)\mathrm{e}^{\mathrm{i}Kr_{12}}|CDJ'M'\rangle, \tag{3.19}$$

can be obtained by using Eq.(3.7) and Eq.(3.12) together with the following identity

$$\frac{\mathrm{e}^{iKr_{12}}}{r_{12}} = \mathrm{i}K\sum_{\nu=0}^{\infty}(2\nu+1)j_\nu(Kr_<)(n_\nu(Kr_>) - \mathrm{i}j_\nu(Kr_>))\boldsymbol{C}^\nu(1)\cdot\boldsymbol{C}^\nu(2), \tag{3.20}$$

to give

$$\begin{aligned} V_{12\text{Møller}} &= \langle ABJM|\frac{e^2}{r_{12}}(1 - \boldsymbol{\alpha}_1 \cdot \boldsymbol{\alpha}_2)\mathrm{e}^{\mathrm{i}Kr_{12}}|CDJ'M'\rangle \\ &= \delta_{JJ'}\delta_{MM'}\sum_{\nu=0}^{\infty} M_C^\nu(ABCD;JM)R_C^\nu(ABCD) \\ &+ \delta_{JJ'}\delta_{MM'}\sum_{\nu\beta\beta'} M_M^{\nu\beta\beta'}(ABCD;JM)R_M^\nu(A\beta, B-\beta', C-\beta, D\beta'), \end{aligned} \tag{3.21}$$

where the angular parts $M_C^\nu(ABCD;JM)$ and $M_M^{\nu\beta\beta'}(ABCD;JM)$ are given by Eq.(3.8) and Eq.(3.13) respectively. The radial integrals $R_C^\nu(ABCD)$ and $R_M^\nu(A\beta, B-\beta', C-\beta, D\beta')$ are given by Eq.(3.9) and

Eq.(3.14) respectively with the change,

$$\frac{r_<^\nu}{r_>^{\nu+2}} \rightarrow -[\nu] K j_\nu(Kr_<)(n_\nu(Kr_>) - \mathrm{i} j_\nu(Kr_>)), \tag{3.22}$$

according to Eq.(3.20). In the above $K = |E_C - E_A|/c = |E_D - E_B|/c$ which pertains to the onshell matrix elements. For the off-shell matrix elements we follow the method adopted by Fontes [1] and use the operator derived by Mittleman [110–112],

$$V_{12\text{Møller}} \quad = \quad 1/2\left(V_{12\text{Møller}}(K_{AC}) + V_{12\text{Møller}}(K_{BD})\right), \tag{3.23}$$

where $K_{AC} = |E_C - E_A|/c$ and $K_{BD} = |E_D - E_B|/c$.

3.3 Results

3.3.1 Excitation cross sections for hydrogenlike targets with $Z = 50$ and $Z = 100$

In order to check our computer code we initially performed first-order "Born-Oppenheimer" (BO) calculations where the exchange of projectile and target electrons is included but only the first term on the right hand side in the set of Lippmann-Schwinger equations (4.22) is kept. Our results for $1s - 2s$, $1s - 2p_{1/2}$, and $1s - 2p_{3/2}$ electron impact excitation cross sections for both $Z = 50$ and $Z = 100$ are in excellent agreement to within $1 - 2\%$ with the first-order BO calculations of Fontes et al. [1], as illustrated in Tables 3.1 and 3.2. Calculations of Walker [108], and Moores and Pindzola [113]) (not presented in Tables 3.1 and 3.2) are in similarly good agreement with our results.

We then performed full close-coupling RCCC calculations by solving the Lippmann-Schwinger equation (4.22) for (i) Coulomb and then (ii) Coulomb+Breit interactions and found that the full RCCC and first-order BO excitation cross sections at both $Z = 50$ and $Z = 100$ were within $1 - 2\%$ for most transitions, and differed at most by 3.6% for the $1s - 2p_{1/2}$ transition with $Z = 100$. Thus, as shown in Tables 3.1 and 3.2, the RCCC method produces practically the same results as first-order calculations for highly charged ions.

The full RCCC calculations that include the Møller interaction are pro-

hibitively time consuming due to the spherical Bessel and Neumann functions that must be generated for both on and off-shell radial matrix elements. Thus, on the grounds that in both the Coulomb and Coulomb+Breit cases the full RCCC and first-order results are practically the same we restricted our Møller interaction calculations to those in which the RCCC code was run in the first-order mode.

Table 3.1: Scaled (Z^4Q) excitation cross sections (Q) in units of πa_0^2, for $n = 1$ to $n = 2$ transitions in a hydrogenlike ion with $Z = 50$ at incident electron energy equal to the ionization energy, $E_I = 35$ keV. The present RCCC and first-order Born-Oppenheimer (BO) calculations are described in the text and compared with the results of Fontes et al. [1]. The number of partial waves used in the calculations are given by J.

Transition	J		Coulomb	Coulomb+Breit	Møller
$1s - 2s$		Fontes *et al.*	0.4438	0.5064	0.5082
	5	BO	0.4439	0.5066	0.5083
	5	RCCC	0.4399	0.5042	
$1s - 2p_{1/2}$		Fontes *et al.*	0.5536	0.5428	0.5466
	9	BO	0.5537	0.5396	0.5492
	9	RCCC	0.5500	0.5296	
$1s - 2p_{3/2}$		Fontes *et al.*	1.0127	0.9829	0.9934
	9	BO	1.0138	0.9783	0.9900
	9	RCCC	1.0065	0.9619	

Table 3.2: As in Table 3.1 but for $Z = 100$ ($E_I = 162$ keV).

Transition	J		Coulomb	Coulomb+Breit	Møller
$1s - 2s$		Fontes *et al.*	0.8269	1.2514	1.2816
	5	BO	0.8283	1.2526	1.2781
	5	RCCC	0.8350	1.2629	
$1s - 2p_{1/2}$		Fontes *et al.*	0.5227	0.7173	0.8040
	8	BO	0.5229	0.7226	0.8006
	8	RCCC	0.5039	0.7037	
$1s - 2p_{3/2}$		Fontes *et al.*	0.5940	0.6241	0.7068
	9	BO	0.5977	0.6238	0.7155
	9	RCCC	0.5972	0.6355	

3.3.2 Polarization of the Lyman-α_1 line

We present in this section results of our calculations of electron scattering from hydrogenlike Ti^{21+}, Ar^{17+}, Fe^{25+} and U^{91+} ions. The structure model for all considered ions was generated by diagonalizing the target Hamiltonian in a Dirac L-spinor basis (see [114]) consisting of 17s, 17p, 17d, 17f, and 17g states using an exponential fall off parameter $\lambda = Z$, where Z is the nuclear charge. Such a model leads to the states up to principle quantum number $n = 5$ laying in the bound-state spectrum with the rest providing square integrable discretization of the target continuum.

Close-coupling RCCC calculations have been performed across a wide energy range by solving the Lippmann-Schwinger equation (4.22) for (i) Coulomb and then (ii) Coulomb+Breit interactions. We have found that the full RCCC results are generally in good agreement ($\approx 5\%$) for all considered target ions with first-order "Born-Oppenheimer" (BO) calculations. Given the apparent lack of interchannel coupling we will normally present results for first-order BO calculations and give brief comments for the cases where interchannel coupling plays a more important role. In all results presented the term "Breit" implies Coulomb+Breit interactions incorporated together.

Magnetic sublevel excitation cross sections of the $2p_{3/2}$ state from the ground $1s_{1/2}$ state given by Eq. (2.58) are required to determine the polarization of the $2p_{3/2} \to 1s_{1/2}$ line. These cross sections are related to the polarization by the following expression [115]

$$P = \frac{3(\sigma_{1/2} - \sigma_{3/2})}{3\sigma_{3/2} + 5\sigma_{1/2}}, \tag{3.24}$$

where σ_{m_f} is the cross section for excitation to a magnetic sublevel given by Eq. (2.58).

Cascades from the high-lying excited levels (up to $n = 5$) to the $2p_{3/2}$ state can affect the polarization of the $2p_{3/2} \to 1s_{1/2}$ line. We will refer to the cross section and polarization obtained without account of cascades as direct and those obtained with account of cascades as apparent. We take into account the cascades by considering the contribution to the $2p_{3/2}$ state magnetic sublevel cross section σ_{m_f} from an upper lying state n with cross section σ_{m_n} to be

$$\sigma_{m_f}^{\mathrm{casc},m_n} = \sigma_{m_n} b(n,f) \langle j_f m_f 1q | j_n m_n \rangle^2, \tag{3.25}$$

where $\langle j_f m_f 1q | j_n m_n \rangle$ is a Clebsh-Gordan coefficient and $b(n, f)$ is the branching ratio for dipole radiative decay from the upper level n to the lower level f. By applying this formula to all possible radiative decay paths and summing over all bound states we obtain an estimate of the total cascade correction

$$\sigma_{m_f}^{\rm app} = \sigma_{m_f} + \sum_n \sum_{m_n} \sigma_{m_f}^{{\rm casc},m_n}. \tag{3.26}$$

The direct plus cascades values of magnetic sublevel $2p_{3/2}$ state (apparent) cross sections $\sigma_{m_f}^{\rm app}$ are then used in calculation of polarization via Eq. (3.24). This scheme has been used with good results in a number of our previous publications [116–118]. A more sophisticated account of cascades can be done via the collision-radiative kinetic model [119, 120]. This model, however, reduces to our approach if all step-wise electron excitation and deexcitation processes are neglected, which is a good approximation in the case of EBIT experiments due to the low ion density.

In Fig. 3.1 and Table 3.4 we present results of our calculations for the polarization of Lyman-α_1 emission line of Ar^{17+},Ti^{21+}, and Fe^{25+} ions. Our calculations for direct polarization (no cascade corrections) with Coulomb potential are in good agreement with previous Coulomb potential distorted-wave calculations of Reed and Chen [121] and results of distorted-wave code of Zhang et al. [122] reported by Robbins et al. [3]. Similarly to previous calculations [123], we found little difference between the polarization of the three considered ions when results are presented in threshold units. The $1s_{1/2} \rightarrow 2p_{3/2}$ energy thresholds for each ion are presented in Table 3.3.

The cascades provide approximately equal contributions to each of the $m_f = 3/2$ and $m_f = 1/2$ magnetic sublevel cross sections, and the effect of the cascades on polarization of the Lyman-α_1 line proved to be minor. This can be seen in Fig. 3.1 by comparing Coulomb potential direct and apparent polarizations. We estimate that cascades corrections lead to about 10% depolarization of the radiation.

We find that the cascade effects are of similar magnitude for both Coulomb and Breit potential calculations. Hence, only cascade corrected (apparent) results are presented for the latter calculations. Our Breit potential calculations show substantial difference from the Coulomb potential calculations and are in very good agreement with the experimental results of Nakamura et al. [2] for Ti^{21+}, Robbins et al. [3] for Ar^{17+} and Fe^{25+} ions,

Table 3.3: $1s_{1/2} \rightarrow 2p_{3/2}$ energy thresholds for Ar^{17+}, Ti^{21+}, and Fe^{25+} ions.

	Threshold (eV)
Ar^{17+}	3324.1
Ti^{21+}	4979.1
Fe^{25+}	6977.9

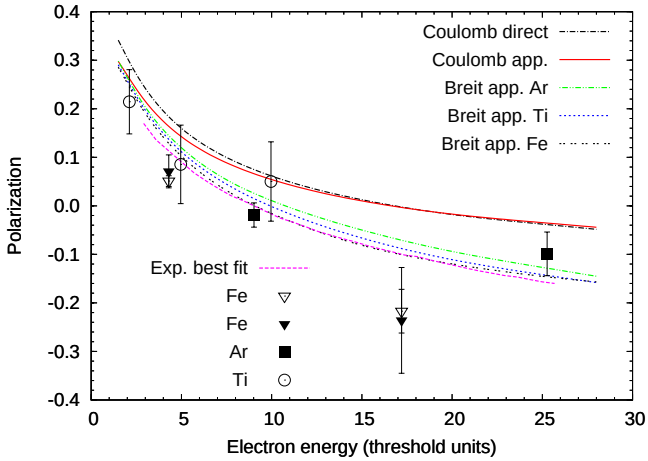

Figure 3.1: Polarization of Lyman-α_1 emission line of Ar^{17+},Ti^{21+}, and Fe^{25+}. Present calculations are compared with experimental data of Nakamura et al. [2] and Robbins et al. [3]. Presented Coulomb potential calculations are for Ti^{21+} ions (results for Ar^{17+} and Fe^{25+} ions are practically the same). The two sets of experimental results for Fe^{25+} pertain to the two experiments outlined in Robbins et al. [3].

and in particular with the line of best fit to experimental data as presented by Robbins et al. [3]. At low energies an account of channel coupling and in particular coupling to the ionization continuum has only a minor effect on the direct cross section and polarization, however it reduces the effect of cascading and brings the direct and apparent cross sections closer together.

The difference between Coulomb potential and Breit potential calculations is greater at larger energies. This is consistent with expected increasing effect of relativistic corrections with the increase of incident electron energy.

Similarly, at larger energies we can see the change of polarization with the change of nuclear charge (variation of polarization between Ar^{17+},Ti^{21+},

Table 3.4: Cascade corrected (apparent) and direct polarization results for Lyman-α_1 for Ar^{17+}, Ti^{21+}, and Fe^{25+} ions compared to experimental measurements of Nakamura et al. [2] for Ti^{21+}, and Robbins et al. [3] for Ar^{17+} and Fe^{25+}. The two sets of experimental results for Fe^{25+} labeled (a) and (b) pertain to the two experiments outlined in Robbins et al. [3].

Energy (keV)		Coulomb	Breit	Expt
Ar^{17+}				
30	app.	$+0.063$	$+0.027$	-0.019 ± 0.025
	dir.	$+0.070$	$+0.031$	
84	app.	-0.051	-0.128	-0.099 ± 0.045
	dir.	-0.056	-0.144	
Ti^{21+}				
10.6	app.	$+0.262$	$+0.250$	$+0.214 \pm 0.066$
	dir.	$+0.296$	$+0.283$	
24.7	app.	$+0.143$	$+0.113$	$+0.085 \pm 0.081$
	dir.	$+0.161$	$+0.127$	
49.6	app.	$+0.055$	-0.0009	$+0.050 \pm 0.082$
	dir.	$+0.062$	-0.0003	
Fe^{25+}				
30	app.	$+0.165$	$+0.128$	$+0.071 \pm 0.034$[a]
				$+0.051 \pm 0.011$[b]
	dir.	$+0.186$	$+0.145$	
120	app.	$+0.0073$	-0.102	-0.236 ± 0.109[a]
				-0.217 ± 0.045[b]
	dir.	$+0.0095$	-0.114	

and Fe^{25+} ions) . We have also performed calculations using the Møller potential and found only minor differences from Breit potential calculations at large incident electron energies for these ions.

The effect of the Breit interaction and cascades on the $2p_{3/2}$ state integrated cross section is illustrated in Fig. 3.2 for the Ti^{21+} ion. We find that cascading plays a relatively larger role for cross sections compared to its effect on the line polarization, especially at lower energies. However, the relativistic corrections to the Coulomb interaction cannot be distinguished for these intermediately charged ions. In Fig. 3.3 we present direct magnetic sublevel cross sections for $2p_{3/2}$ state calculated with the Coulomb and Breit potentials. Account of Breit relativistic corrections leads to a slight increase of the cross sections, with the cross section for the $m = 1/2$ sublevel being affected more than for the $m = 3/2$ sublevel. It is this difference that is em-

phasized in the calculation of the polarization of Lyman-α_1 emission line and makes measurements of polarization a sensitive test of relativistic effects in electron-ion scattering. Relativistic corrections to the Coulomb interaction

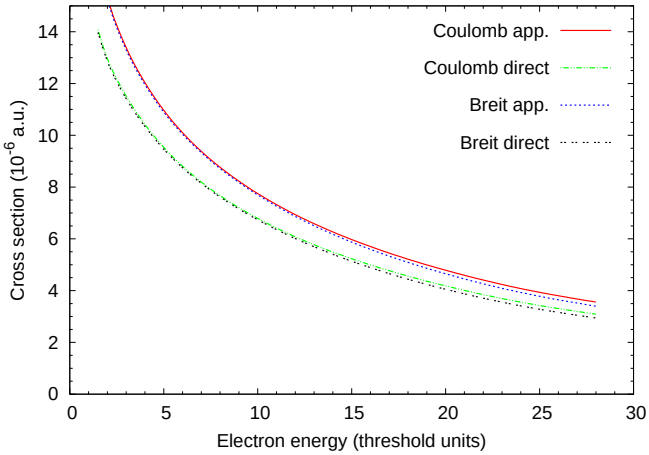

Figure 3.2: Direct and apparent cross sections for excitation of the $2p_{3/2}$ state of Ti^{21+}. Present calculations are described in the text.

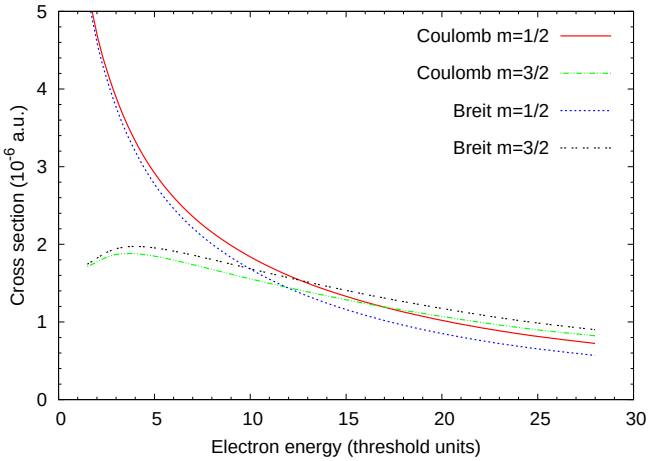

Figure 3.3: Magnetic sublevel direct cross sections for excitation of the $2p_{3/2}$ state of Ti^{21+}. Present calculations are described in the text.

become more important as the charge of an ion increases. It is, therefore, interesting to investigate the electron scattering from hydrogenlike U^{91+} ion. The EBIT experiment of Marrs et al. [6] concentrated on measurements of

total ionization cross section (see next Section). A new experiment at GSI Darmstadt [124] is expected to determine the Lyman-α_1 line polarization.

In support of this experiment we have conducted calculation of e-U^{91+} scattering. Direct and apparent cross sections for excitation of the $2p_{3/2}$ state are presented in Fig. 3.4. We find good agreement with previous calculations of $2s_{1/2}$, $2p_{1/2}$, and $2p_{3/2}$ direct cross sections by Moores and Pindzola [113], and Fontes et al. [1], performed with Coulomb, Breit, and Møller potentials. Account of Breit relativistic corrections does not change the cross section substantially while account of the Møller interaction leads to a much stronger effect. Cascade corrections proved to be very large ranging from about 50% at lower energies to 30% at larger energies.

In Fig. 3.5 we present our predictions for the polarization of the Lyman-α_1 emission line of U^{91+}. As expected an account of relativistic corrections leads to a large change in polarization. Calculations with the Coulomb potential lead to polarization that varies little across the considered energy range from one to six times the excitation threshold. Both Breit and Møller relativistic corrections lead to polarization that changes significantly more across the same energy range. At low energies the Breit and Møller potential results converge to the same polarization values which are different to the Coulomb potential results. At large energies the Breit and Møller potential results diverge with the Møller potential results showing much larger variation across the energy range. Cascading leads to substantial depolarization of the radiation. Its effect is much larger for the U^{91+} ion than for the lower charged ions considered. Given such a large effect a more accurate account of cascading via the collision-radiative kinetic model [119, 120] seems to be warranted. This will be investigated in the future. We note, however, that regardless of the accuracy of the cascading accounted for in the present work, our calculations predict a clear distinction between calculations of Lyman-α_1 emission line polarization with Coulomb, Breit, and Møller potentials. The difference between these calculations appears to be sufficiently large to be observed in experiment.

3.3.3 Ionization cross section of U^{91+}

In the RCCC method to obtain the total ionization cross section we sum over all the excitation cross sections that correspond to excitation of pseudostates

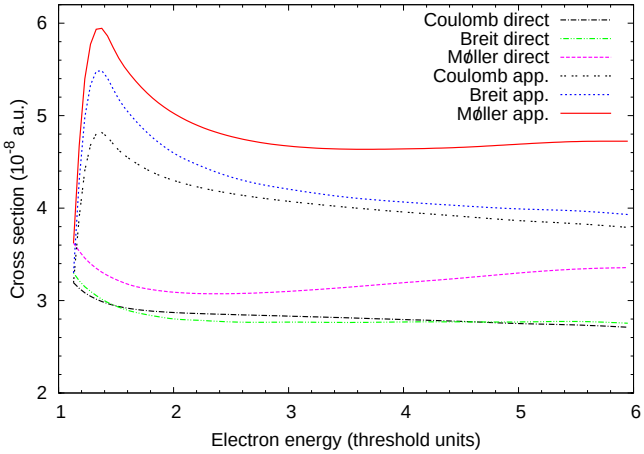

Figure 3.4: Direct and apparent cross sections for excitation of the $2p_{3/2}$ state of U^{91+}. Present calculations are described in the text.

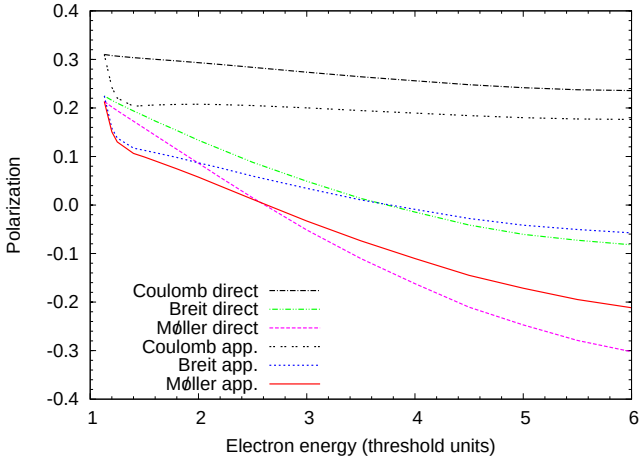

Figure 3.5: Polarization of Lyman-α_1 emission line of U^{91+}. Present calculations are described in the text.

above the ionization threshold

$$\sigma_{\text{ioniz}} = \sum_{f:0\leq\epsilon_f\leq E} \sigma_{fi}, \tag{3.27}$$

where ϵ_f is the energy of the pseudostate and E is the total energy of the system.

When the RCCC code is run in first-order mode the total ionization cross section is instead obtained using

$$\sigma^{\rm BO}_{\rm ioniz} = \sum_{f:0\leq\epsilon_f\leq E/2} \sigma^{\rm BO}_{fi}, \tag{3.28}$$

where the sum only extends up to $E/2$. This is required in order to avoid double counting of pseudostates that represent the continuum. This method seems to be inconsistent with Eq.(3.27) employed in the full RCCC method, however it has been demonstrated [125] that $\sigma_{fi}(\epsilon_f) \to 0$ for $\epsilon_f > E/2$ with an increasing number of states, N. That is, $\sigma_{fi}(\epsilon_f)$ converges to a step function as the number of states used in the calculation increases and this is a consequence of inter-channel coupling in the RCCC method. The effect of double counting the pseudostates in first-order total ionization cross section calculations is demonstrated for the Coulomb interaction case in Fig. 3.6, where it can be seen that the U^{91+} total ionization cross section for the 1s electron is not in agreement with the full RCCC results if double counting occurs, whereas when double counting is avoided the first-order calculations are in excellent agreement with the full RCCC calculations. We

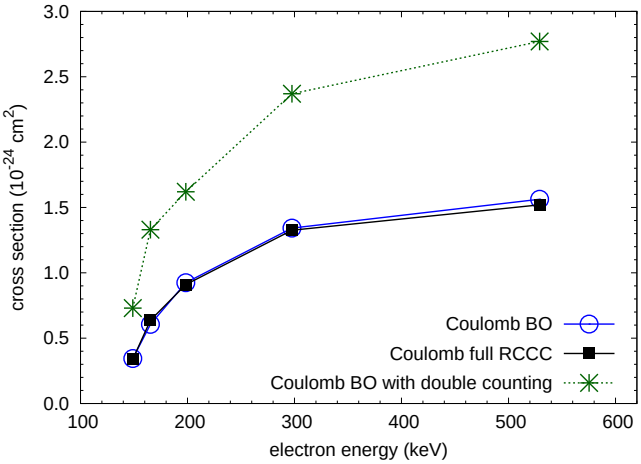

Figure 3.6: U^{91+} total ionization cross section for the 1s electron calculated with the Coulomb interaction. Full close-coupling (RCCC) results are compared to the first-order Born-Oppenheimer (BO) results obtained with and without account for double counting.

have performed first-order BO total ionization cross section calculations for

U^{91+} with (i) Coulomb and (ii) Møller interactions included and we found excellent agreement with the corresponding results of Fontes et al. [5], as shown in Fig. 3.7. In the RCCC method the continuum is modeled by pseudostates generated from an asymptotic nuclear charge of $Z - 1$. This differs from the calculations of Fontes et al. [5] where the continuum states are generated from a nuclear charge Z. However for a highly charged target with large Z the difference is apparently minimal. We have also found that

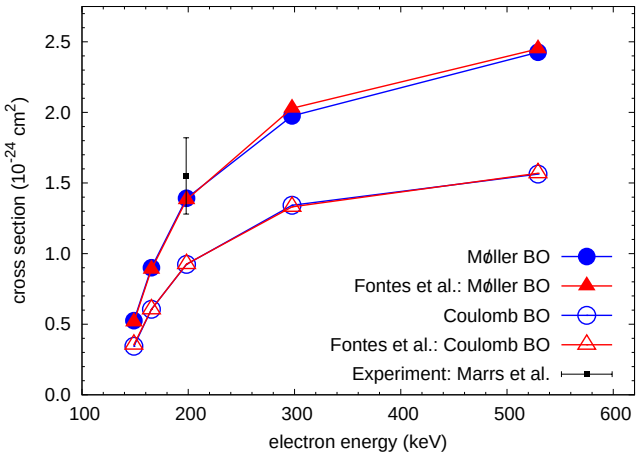

Figure 3.7: U^{91+} total ionization cross section for the 1s electron. Present results are compared with the first-order BO calculations of Fontes et al. [5], and the experimental results of Marrs et al. [6].

the effects of distortion of the target charge distribution (represented by the choice of U in Eq. (2.26)) were negligible. This can be readily understood by noting that the distorting potential U is only minor compared to the U^{91+} Coulomb potential.

The results presented in Fig. 3.7 include the exchange of projectile and target electrons. It has been highlighted by Moores and Reed [126] and Fontes et al. [127] that the account of the exchange of projectile and target electrons in the calculations of the U^{91+} 1s total ionization cross section leads to only minimal changes in the case of the Coulomb interaction, but has a significant effect in the case of the Breit and Møller interactions and is crucial in achieving agreement with the experiment of Marrs et al. [6]. We indeed found this to be the case as illustrated in Fig. 3.8. It is interesting to note that even though the account of the exchange leads to only a minor

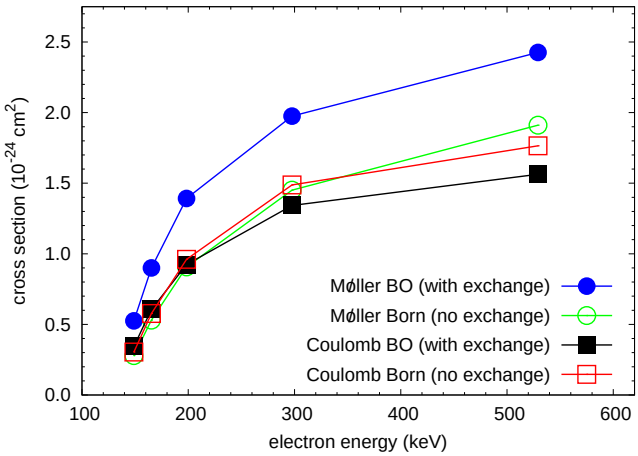

Figure 3.8: First-order U^{91+} total ionization cross section calculations for the 1s electron illustrating the effects of the exchange of projectile and target electrons.

change in the U^{91+} 1s total ionization cross section for the Coulomb interaction, it does not mean that the exchange scattering is negligible. This is illustrated in Fig. 3.9 for the ionization spin asymmetries [128]. Large values of the ionization spin asymmetries indicate the importance of the exchange scattering not only for the Breit and Møller potentials but also for the Coulomb potential.

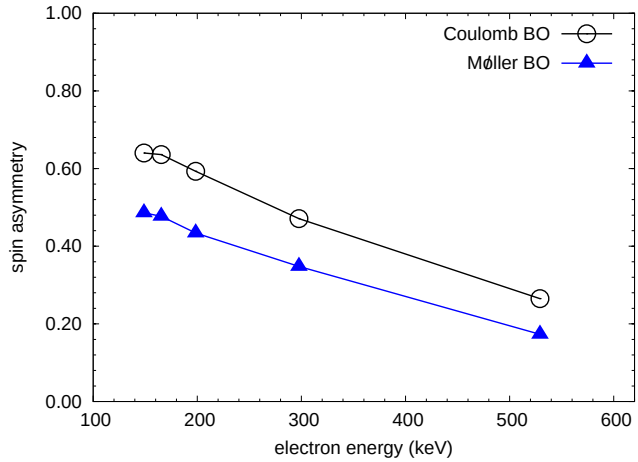

Figure 3.9: U^{91+} ionization spin asymmetries for the 1s electron.

Chapter 4

RCCC method for quasi two-electron targets

In this Chapter we present the extension of the relativistic convergent close-coupling method to accommodate two electron and quasi-two electron targets. We apply the theory to electron scattering from mercury and obtain differential and integrated cross sections for elastic and inelastic scattering. We compare with previous nonrelativistic CCC calculations and for a number of transitions obtained significantly better agreement with experiment. The RCCC method is able to resolve structure in the integrated cross sections for the energy regime in the vicinity of the excitation thresholds for the $(6s6p)^3P_{0,1,2}$ states. These cross sections are associated with the formation of negative ion (Hg^-) resonances that could not be resolved with the non-relativistic CCC method. The RCCC results are compared with experiment and other relativistic theories.

4.1 Overview of electron-mercury scattering

Electron-mercury scattering serves as a testing ground [129] for relativistic theories due to its high atomic number, $Z = 80$. Furthermore, electron-mercury scattering plays an important practical role in the physics of fluorescent and high intensity discharge lamps [130–132]. The main source of light from these lamps is the 254 nm UV radiation emitted when the $(6s6p)^3P_1^o$ state decays to the $(6s^2)^1S_0$ ground state. This optical transition is a clear indication of a break-down of the nonrelativistic approximation

due to the strong spin-orbit interaction in mercury resulting in a significant singlet-triplet mixture for the mercury $(6s6p)^3P_1^o$ and $(6s6p)^1P_1^o$ states. In Hg fluorescent lamps this 254nm radiation is absorbed by a phosphor coating which in turn emits visible light.

Accurate plasma physics modeling of mercury based lamps requires detailed information on a large number of electron impact excitation cross sections involving transitions between various states. Compilation of e-Hg cross sections obtained from swarm data by Rockwood [133] is widely used in plasma modeling to date even though more recent measurements for a number of transitions [15, 16] are found to be in large disagreement with the former data. Given the difficulty in obtaining the comprehensive set of cross sections by experiment alone, a theoretical description of e-Hg scattering plays an important role in verifying the accuracy of the currently used cross sections, and also establishing a new accurate set of e-Hg cross sections.

Previously the nonrelativistic CCC method has been applied to the calculation of e-Hg scattering [14]. The most important relativistic effects were taken into account approximately by transformation of the scattering amplitudes to an intermediate coupling scheme which allowed cross sections to be obtained for a wide range of transitions. While generally there was good agreement between the CCC results and available experimental data there were a number of cases where the CCC results were either in disagreement with experiment (e.g., elastic scattering DCS at 15 eV) or could not be reliably applied to calculation of particular transitions due to the inaccuracy of the approximate treatment of relativistic effects (e.g., excitation of$(6s6p)^3P_j^o$ fine-structure sublevels near the excitation threshold). With the development of the RCCC method we are now in a position to perform e-Hg calculations without any approximation in the treatment of relativistic effects both in target structure and scattering calculations.

There is a long history of previous experimental and theoretical studies of electron scattering from mercury. Experimentally, integrated cross sections in the excitation threshold region of the triplet $(6s6p)^3P_{0,1,2}^o$ states have been measured by Hanne et al. [8], Ottley and Kleinpoppen [9], Erdevdi et al. [10], Newman et al. [11], Borst [12] and Krause et al. [13]. Integrated excitation cross sections for excitation of the singlet $(6s6p)^1P_1^o$ state have been measured by Zubek et al. [15], Panajotović et al. [16],

and Peitzmann and Kessler [17]. Integrated cross sections for excitation of $(6s7s)^1S_0$ and $(6s7p)^1P_1^o$ states have been measured by Panajotović et al. [16], and angle differential cross sections for elastic scattering from the $(6s^2)^1S_0$ ground state have been measured by Zubek et al. [15] and Holtkamp et al. [18]. Angle differential cross sections at 15 eV for excitation of the triplet $(6s6p)^3P_{0,1,2}^o$ states and singlet $(6s6p)^1P_1^o$ state have been measured by Zubek et al. [15]. At 60 eV, angle differential cross sections for the $(6s6p)^3P_1^o$ and $(6s6p)^1P_1^o$ states have been measured by Panajotović et al. [16] and Peitzmann and Kessler [17]. Panajotović et al. [16] have also measured angle differential cross sections for the $(6s7s)^1S_0$ and $(6s7p)^1P_1^o$ states at this energy. Total cross section measurements have been obtained by Jost and Ohnemus [19], and elastic cross sections have been measured by Panajotović et al. [16], Zubek et al. [20], and Holtkamp et al. [18]. Elastic momentum transfer cross sections have been measured by Elford [134], England and Elford [22], and Panajotović et al. [16]. These play an important role in determining the electrical characteristics of discharge lamps. There are also extensive spin-dependent measurements for electron-mercury scattering [129].

On the theoretical side, in addition to the nonrelativistic CCC method employed by Fursa et al. [14], there have been many other attempts to model electron scattering from mercury. Some of these include potential scattering models by Walker [135], McEachran and Stauffer [136], Sienkiewicz [137], Sienkiewicz [138], and McEachran and Elford [21]. Haberland and Fritsche [139] used the generalized Kohn-Sham method. Close coupling calculations have also been performed: a five-state semi-relativistic Breit-Pauli R-matrix method has been used by Scott et al. [140], Bartschat et al. [141], and Bartschat [142] to calculate excitation cross sections of the $6s6p^1P_1$ and $6s6p^3P_{0,1,2}$ states. Wijesundera et al. [143] used a five state relativistic Dirac R-matrix method to study resonances and also calculated elastic cross sections and excitation cross sections for the $(6s6p)^3P_{0,1,2}$ states. The excitation of the $6s6p^1P_1$ state has been studied by Bartschat and Madison [144] using a semi-relativistic distorted-wave Born approximation and also by Srivastava et al. [145] using a fully relativistic distorted-wave method.

Recently, Zatsarinny and Bartschat [7] performed a 36 state Dirac B-spline R-matrix (DBSR) close-coupling calculation for electron scattering from mercury. They reported a significant improvement in agreement with

experiment over previous calculations especially at low and near threshold energies. Overall the DBSR calculations are in good agreement with the non-relativistic CCC results for incident electron energies above the threshold region. The important feature of the DBSR method is its ability to describe accurately the Hg target structure by allowing opening of the [Xe]$4f^{14}5d^{10}$ core. On other hand, in the CCC method (similar to practically all other calculations) the Hg atom was modeled as an atom with two active electrons above a frozen core [Xe]$4f^{14}5d^{10}$. With the uncertainty of the approximate treatment of relativistic effects in the CCC method now removed in the RCCC method, we can now investigate whether the frozen-core model of Hg is sufficient to provide an accurate description of scattering near the thresholds of the $(6s6p)^3P_{0,1,2}$ triplet states. Similarly, the new RCCC calculations of e-Hg scattering will also be able to verify the accuracy of our previous nonrelativistic calculations for the transitions that are strongly affected by relativistic effects.

This Chapter is organized as follows: the next section contains the formulation of the RCCC method applicable to two electron and quasi-two electron targets, and the following section presents RCCC results for integrated and angle differential cross sections for elastic and inelastic electron collisions with mercury. Also presented are total, elastic and momentum transfer cross sections. Atomic units are assumed throughout.

4.2 RCCC method for two-electron targets

Application of the RCCC method to electron scattering from two electron and quasi two-electron targets follows a similar scheme as described in Chapter 2 for quasi-hydrogenlike targets, however significant modifications are required for the V-matrix elements.

The target Hamiltonian is diagonalized in a Dirac L-spinor basis and then the obtained target states are used as an expansion basis to generate a set of coupled Lippmann-Schwinger equations for the electron-atom/ion scattering system. The latter are solved in momentum space for the T-matrix elements from which the cross sections are calculated.

For the case of electron scattering from mercury, the target atom is modeled as a quasi-two electron atom consisting of two valence electrons above an inert [Xe]$4f^{14}5d^{10}$ frozen core. The next two sections outline the

calculation of the target states and then the theory required to set up and solve the coupled Lippmann-Schwinger equations for the scattering problem.

4.2.1 Target structure

Calculation of target wavefunctions and energy levels for two valence electron above an inert [Xe]$4f^{14}5d^{10}$ frozen core involves the three steps listed below:

1. The [Xe]$4f^{14}5d^{10}$ frozen core orbitals $\{\varphi_c\}$ are calculated with the GRASP package [82] that employs a relativistic self-consistent field Dirac-Fock procedure.

2. The Hg^+ one electron Hamiltonian,

$$H_i = c\,\boldsymbol{\alpha}\cdot\boldsymbol{p}_i + \beta mc^2 + V_i, \tag{4.1}$$

is then diagonalized with a Dirac L-spinor basis [86],

$$\begin{aligned} f^{\mathrm{L/S}}_{n_r\kappa}(r) &= \left[\frac{n_r!(2\gamma+n_r)}{2N_{n_r\kappa}(N_{n_r\kappa}-\kappa)\Gamma(2\gamma+n_r)}\right]^{1/2}(2\lambda r)^{\gamma}e^{-\lambda r} \\ &\quad\times\left(-(1-\delta_{n_r,0})L^{2\gamma}_{n_r-1}(2\lambda r)\pm\frac{N_{n_r\kappa}-\kappa}{n_r+2\gamma}L^{2\gamma}_{n_r}(2\lambda r)\right), \end{aligned} \tag{4.2}$$

with the method outlined in detail in Chapter 2 for quasi-one electron targets. Briefly, V_i is the interaction of one of the valence electrons with a closed core and is a sum of a frozen-core Dirac-Fock potential V^{FC} and a polarization potential V^{pol},

$$V_i = V^{\mathrm{FC}} + V^{\mathrm{pol}}. \tag{4.3}$$

The non-local V^{FC} potential is defined as a sum of local (direct) $V^{\mathrm{FC}}_{\mathrm{d}}$ and non-local (exchange) terms,

$$V_i = V^{\mathrm{FC}}_{\mathrm{d}} + V^{\mathrm{FC}}_{\mathrm{e}}, \tag{4.4}$$

with

$$V_{\rm d}^{\rm FC}\phi(\boldsymbol{r}_i) = \left(-\frac{Z}{r}+\sum_{\varphi_{\rm c}}\int d^3r'\frac{|\varphi_{\rm c}(\boldsymbol{r'})|^2}{|\boldsymbol{r}-\boldsymbol{r'}|}\right)\phi(\boldsymbol{r}_i), \tag{4.5}$$

$$V_{\rm e}^{\rm FC}\phi(\boldsymbol{r}_i) = -\sum_{\varphi_{\rm c}}\int d^3r'\frac{\varphi_{\rm c}(\boldsymbol{r'})^*\phi(\boldsymbol{r'_i})}{|\boldsymbol{r}-\boldsymbol{r'}|}\varphi_{\rm c}(\boldsymbol{r}). \tag{4.6}$$

3. The set of electron orbitals $\{\phi_\alpha\}$ so obtained are used to perform standard configuration-interaction calculations [34] to obtain a set of Hg target states.

In this last step, the method employed to perform the configuration interaction calculation is similar to that described in detail by Fursa and Bray [34] with the exception that the jj coupling scheme is utilized in the relativistic formulation. Therefore the Hg target states are expressed as

$$\Phi_n(\boldsymbol{r}_1,\boldsymbol{r}_2)=\sum_{\alpha\beta}C_{\alpha\beta}^{(n)}\langle\boldsymbol{r}_1\boldsymbol{r}_2|\phi_\alpha(1)\phi_\beta(2):J_{T_n}m_n\pi_n\rangle, \tag{4.7}$$

where the configuration interaction coefficients $C_{\alpha\beta}^{(n)}$ satisfy

$$C_{\alpha\beta}^{(n)}=(-1)^{j_\alpha+j_\beta-J_n}C_{\beta\alpha}^{(n)}, \tag{4.8}$$

to ensure antisymmetry of the two electron target states. The parity of the target states is $\pi=(-1)^{l_\alpha+l_\beta}$ and

$$|j_\alpha j_\beta:J_nm_n\rangle=\sum_{m_\alpha m_\beta}C^{J_nm_n}_{j_\alpha m_\alpha j_\beta m_\beta}|j_\alpha m_\alpha j_\beta m_\beta\rangle, \tag{4.9}$$

where $C^{J_nm_n}_{j_\alpha m_\alpha j_\beta m_\beta}$ is a Clebsch-Gordan coefficient. The target states $\Phi_n(\boldsymbol{r}_1,\boldsymbol{r}_2)$ satisfy

$$\langle\Phi_{n'}|H_T|\Phi_n\rangle=\epsilon_n\delta_{n'n}, \tag{4.10}$$

where

$$H_{\rm T}=H_1+H_2+V_{12}, \tag{4.11}$$

with

$$V_{12}=1/|\boldsymbol{r}_1-\boldsymbol{r}_2|+V^{\rm diel}(\boldsymbol{r}_1,\boldsymbol{r}_2), \tag{4.12}$$

and the Dirac Hamiltonian for each electron, H_i, is given by Eq. 4.1. The phenomenological one-electron $V^{\rm pol}$ and two-electron $V^{\rm diel}$ core polarization potentials allow us to take into account more accurately the effect of closed inert shells on the active electron [14]. The cut-off radii $r_{\rm c}^{\rm pol}$ and $r_{\rm c}^{\rm diel}$ of these potentials are chosen to obtain the best representation of target state energies and oscillator strength, while the static dipole polarazability of the inert core α_c is taken either from experiment or accurate calculations. In the case of mercury we chose $\alpha_c = 8.4$, $r_{\rm c}^{\rm pol} = 2.235$ and $r_{\rm c}^{\rm diel} = 2.3$.

Using a Dirac L-spinor basis, Eq. (4.2), consisting of 35 functions for each value of $\kappa = l$ and $\kappa = -l - 1$ for $l = 0, 1, 2, 3$ with an exponential fall-off parameter of 3.5, we diagonalized the Hg^+ Hamiltonian for each value of κ and obtained a set of Hg^+ one electron orbitals $\{\phi_\alpha\}$. These orbitals are then used to perform standard two-electron CI calculations. Similar to our previous nonrelativistic calculations we find that the mercury bound states are well-described in a model where the inner electron is limited to the $6s$ and $6p$ orbitals of the Hg^+ ion. The energy levels obtained for the first 15 lowest lying states are listed in Table 4.1 and are found to be in good agreement with the experimental energies in the NIST database [4]. Further check of the target wavefunction accuracy is provided by optical oscillator strengths. The experimental value for the $(6s6p)^1P_1^o$ oscillator strength is 1.16 and it is in good agreement with our result of 1.20, while for the $(6s6p)^3P_1^o$ state the experimental value of 0.024 is lower than our result of 0.038. The ground state static dipole polarizability of the mercury atom is dominated by the $(6s6p)^1P_1^o$ state and in our structure model has a value of $\alpha_d = 22.6$ which is similar to the value obtained in nonrelativistic CCC calculations [14] but is significantly lower than the experimental value of $\alpha_d = 34.4$ [146]. This difference arises from opening of the $5d^{10}$ shell which is not allowed in the present model and can lead to inaccuracy in the calculated cross sections (see [14] for further discussion).

In the consequent scattering calculations we have used two models: the 29 state model (RCC) that includes only bound states in the close-coupling expansion and a 193 state model (RCCC) which in addition has a large number of positive energy states (relative to the Hg^+ ground state). This allows us to model coupling to ionization channels.

Table 4.1: Energy levels of the first 15 Hg states calculated by diagonalizing the target in the RCCC method. Experimental levels listed by NIST [4] are also shown.

Configuration	Term	J	parity	Energy (eV)	Expt. [4]
$6s^2$	$^1S_0$	0.0	1	0.000	0.000
$6s6p$	$^3P_0^o$	0.0	-1	4.706	4.667
$6s6p$	$^3P_1^o$	1.0	-1	4.926	4.887
$6s6p$	$^3P_2^o$	2.0	-1	5.577	5.461
$6s6p$	$^1P_1^o$	1.0	-1	6.549	6.704
$6s7s$	$^3S_1$	1.0	1	7.775	7.730
$6s7s$	$^1S_0$	0.0	1	8.000	7.926
$6s7p$	$^3P_0^o$	0.0	-1	8.648	8.619
$6s7p$	$^3P_1^o$	1.0	-1	8.667	8.637
$6s7p$	$^3P_2^o$	2.0	-1	8.763	8.829
$6s7p$	$^1P_1^o$	1.0	-1	8.872	8.839
$6s6d$	$^3D_1$	1.0	1	8.869	8.845
$6s6d$	$^1D_2$	2.0	1	8.876	8.844
$6s6d$	$^3D_3$	3.0	1	8.883	8.856
$6s6d$	$^3D_2$	2.0	1	8.887	8.852
Ionization limit				10.447	10.438

4.2.2 Coupled relativistic Lippmann-Schwinger equations

Once the target states are obtained the next step is to use them to generate a set of coupled relativistic Lippmann-Schwinger equations for the scattering problem. The total scattering wave function for the system satisfies

$$(E - H)|\Psi_i^{(+)}\rangle = 0, \tag{4.13}$$

where the superscript (+) denotes incoming plane- or Coulomb-wave and outgoing spherical-wave boundary conditions. We denote the initial target state as Φ_i and the projectile momentum by k_i.

The total Hamiltonian for the scattering system is

$$H = H_{\rm T} - H_0 - V_{01} - V_{02}, \tag{4.14}$$

where the subscript 0 denotes the projectile electron, 1 and 2 denote the electrons in the two electron target, and $H_{\rm T}$ is given by Eq. (4.11).

The projectile Hamiltonian is given by

$$H_0 = c\,\boldsymbol{\alpha}\cdot\boldsymbol{p}_0 + \beta mc^2 + V_0. \tag{4.15}$$

To ensure antisymmetry of the total wave function in accordance with the Pauli exclusion principle, we perform a multichannel expansion of the total wavefunction in the following way

$$\begin{aligned}\Psi_i^{N(+)}(\boldsymbol{r}_0,\boldsymbol{r}_1,\boldsymbol{r}_2) &= (1-P_{01}-P_{02})\psi_i^{N(+)}(\boldsymbol{r}_0,\boldsymbol{r}_1,\boldsymbol{r}_2) &(4.16)\\ &= (1-P_{01}-P_{02})\sum_{n=1}^{N} f_n^N(\boldsymbol{r}_0)\Phi_n^N(\boldsymbol{r}_1,\boldsymbol{r}_2), &(4.17)\end{aligned}$$

where P_{0i} is the space exchange operator. The RCCC method utilizes the completeness of the Dirac L spinor basis used in the diagonalization of the target,

$$\lim_{N\to\infty}\Psi^{N(+)}(\boldsymbol{r}_0,\boldsymbol{r}_1,\boldsymbol{r}_2) = \Psi^{(+)}(\boldsymbol{r}_0,\boldsymbol{r}_1,\boldsymbol{r}_2). \tag{4.18}$$

Substituting Eq. (4.16) and Eq. (4.14) into Eq. (4.13) we obtain

$$\begin{aligned}(E^{(+)} - c\,\boldsymbol{\alpha}\cdot\boldsymbol{p}_0 - \beta mc^2 - U_0 - H_{\rm T} - U_0)\Psi^{N(+)}(\boldsymbol{r}_0,\boldsymbol{r}_1,\boldsymbol{r}_2)&\\ = V\Psi^{N(+)}(\boldsymbol{r}_0,\boldsymbol{r}_1,\boldsymbol{r}_2),&\end{aligned} \tag{4.19}$$

where

$$V = V_0 - U_0 + V_{01} + V_{02} + (E-H)(P_{01}+P_{02}). \tag{4.20}$$

The introduction of an arbitrary short range (distorting) potential, U_0, is used as a numerical technique to reduce the required computational resources; however, the results are independent of U_0. This rearrangement is such that the asymptotic (large r_0) Hamiltonian is

$$H_{\rm a} = c\,\boldsymbol{\alpha}\cdot\boldsymbol{p}_0 + \beta mc^2 + U_0 + H_{\rm T}. \tag{4.21}$$

The asymptotic Hamiltonian is used to generate the Green's function for the total wavefunction, as described in detail in Chapter 2, and the Green's function is then used to generate a set of coupled relativistic Lippmann-Schwinger equations in momentum space for each total angular momentum J and parity Π of the system

$$T_{fi}^{\Pi J}(k_f\kappa_f, k_i\kappa_i) = V_{fi}^{\Pi J}(k_f\kappa_f, k_i\kappa_i) + \sum_n \sum_\kappa \!\!\!\!\!\!\int dk \frac{V_{fn}^{\Pi J}(k_f\kappa_f, k\kappa) T_{ni}^{\Pi J}(k\kappa, k_i\kappa_i)}{E - \epsilon_n^N - \epsilon_{k'} + i0}. \tag{4.22}$$

The direct and exchange V-matrix elements appearing in Eq. (4.20) for electron scattering from a two electron target in the RCCC method differ from their nonrelativistic counterparts due to the fact that the LS coupling scheme is employed in the nonrelativistic case [34], whereas spin and orbital angular momenta are not decoupled in the relativistic case. Therefore we present here the explicit forms of the direct and exchange matrix elements used in the solution of the set of relativistic Lippmann-Schwinger equations, Eq. (4.22).

In a manner similar to the nonrelativistic case for two electron targets [34, 147] we may separate the V operator in Eq. (4.20) as

$$V = (V_0 - U_0 + 2V_{01}) + 2(E - H_{\rm T} - H_0 - V_{01} - V_{02})P_{01}. \tag{4.23}$$

The first term is the direct matrix element, and the second term is the exchange matrix element.

We use the CI representation of the two electron target wave functions to express the matrix elements

$$\begin{aligned} & \langle j_0' k_0'(0), \Phi_{n'} : J' M_{J'} | V | j_0 k_0(0), \Phi_n : J M_J \rangle \\ = & \sum_{\alpha,\beta,\gamma,\delta} C_{\alpha\beta}^{(n')} C_{\gamma\delta}^{(n)} \\ \times & \langle j_0' k_0'(0), \phi_\alpha(1)\phi_\beta(2)(J_T') : J' M_{J'} | V | j_0 k_0(0), \phi_\gamma(1)\phi_\delta(2)(J_T) : J M_J \rangle. \end{aligned} \tag{4.24}$$

4.2.3 Direct matrix element

The direct matrix element is associated with the first term in Eq. (4.23), which has the multipole expansion

$$V^{\rm D} = V_0 - U_0 + 2V_{01}$$

$$= \sum_{\nu} v_\nu(r_0, r_1) \boldsymbol{C}^\nu(0) \cdot \boldsymbol{C}^\nu(1), \tag{4.25}$$

where

$$v_\nu(r_0, r_1) = -\delta_0^\nu \left(\frac{Z}{r_0} + U_0(r_0) \right) + 2\frac{r_<^\nu}{r_>^{\nu+1}}, \tag{4.26}$$

and $\boldsymbol{C}^\nu$ is a renormalized spherical harmonic.

Using standard tensor algebra relations [148] the direct matrix element for each configuration pair reduces to

$$\begin{aligned}
& \langle j_0' k_0'(0), \phi_\alpha(1)\phi_\beta(2)(J_T') : J' M_{J'} | \sum_\nu v_\nu \boldsymbol{C}^\nu(0) \cdot \boldsymbol{C}^\nu(1) \\
\times \quad & |j_0 k_0(0), \phi_\gamma(1)\phi_\delta(2)(J_T) : J M_J \rangle \\
= \quad & \frac{1}{\pi} \sqrt{\frac{(\epsilon_{k'} + c^2)(\epsilon_k + c^2)}{\epsilon_{k'}\epsilon_k}} \langle \phi_\beta | \phi_\delta \rangle \delta_{JJ'} \delta_{M_J M_{J'}} \left\{ \begin{array}{ccc} j_0' & J_T' & J' \\ J_T & j_0 & \nu \end{array} \right\} \langle j_0' || \boldsymbol{C}^\nu(0) || j_0 \rangle \\
\times \quad & \hat{J}_T' \hat{J}_T \delta_{j_\beta j_\delta} (-1)^{j_\alpha + j_\beta + J_T + \nu + J_T' + j_0 + J'} \left\{ \begin{array}{ccc} j_\beta & j_\alpha & J_T' \\ \nu & J_T & j_\gamma \end{array} \right\} \langle J_\alpha || \boldsymbol{C}^\nu(1) || J_\gamma \rangle \\
\times \quad & \int \mathrm{d}r_0 \int \mathrm{d}r_1 \Big[\sum_\nu v_\nu(r_0, r_1) \left(\, f_{\kappa_0'}^U(r_0) f_{\kappa_0}^U(r_0) + f_{-\kappa_0'}^L(r_0) f_{-\kappa_0}^L(r_0) \, \right) \\
\times \quad & \left(\, \phi_{\kappa_\alpha}^U(r_1) \phi_{\kappa_\gamma}^U(r_1) + \phi_{-\kappa_\alpha}^L(r_1) \phi_{-\kappa_\gamma}^L(r_1) \, \right) \Big],
\end{aligned} \tag{4.27}$$

where U and L denote the upper and lower components of the Dirac spinors, and where

$$\langle \phi_\beta | \phi_\delta \rangle = \int \mathrm{d}r_2 \left(\phi_{\kappa_\beta}^U(r_2) \phi_{\kappa_\delta}^U(r_2) + \phi_{-\kappa_\beta}^L(r_2) \phi_{-\kappa_\delta}^L(r_2) \right), \tag{4.28}$$

with

$$\hat{J} = \sqrt{2J+1}. \tag{4.29}$$

4.2.4 Exchange matrix elements

The exchange matrix element is associated with the second term in Eq. (4.23),

$$V^{\mathrm{E}} = 2(E - H_{\mathrm{T}} - H_0 - V_{01} - V_{02}) P_{01}. \tag{4.30}$$

We separate the calculation of the exchange matrix element into a number of steps.

$V_{01}P_{01}$ matrix elements

The first exchange matrix element for each configuration pair is

$$\langle j_0' k_0'(0), \phi_\alpha(1)\phi_\beta(2)(J_T') : J' M_{J'} | V_{01} P_{01} | j_0 k_0(0), \phi_\gamma(1)\phi_\delta(2)(J_T) : J M_J \rangle, \tag{4.31}$$

where

$$V_{01} = \sum_\nu \frac{r_<^\nu}{r_>^{\nu+1}} \boldsymbol{C}^\nu(0) \cdot \boldsymbol{C}^\nu(1). \tag{4.32}$$

We apply the space exchange operator P_{01} to the right hand side and then recouple the angular momenta on the right hand side using

$$|j_0, j_\gamma j_\delta(J_T) : J\rangle = \sum_j \hat{j}\hat{J}_T (-1)^{j_0 + J_T + J_\gamma + j} \left\{ \begin{array}{ccc} j_0 & j_\delta & j \\ j_\gamma & J & J_T \end{array} \right\} |j_\gamma, j_0 j_\delta(j) : J\rangle, \tag{4.33}$$

to obtain

$$\begin{aligned}
& \langle j_0' k_0'(0), \phi_\alpha(1)\phi_\beta(2)(J_T') : J' M_{J'} | V_{01} | j_0 k_0(1), \phi_\gamma(0)\phi_\delta(2)(J_T) : J M_J \rangle \\
= \;& \frac{1}{\pi} \sqrt{\frac{(\epsilon_{k'} + c^2)(\epsilon_k + c^2)}{\epsilon_{k'}\epsilon_k}} \langle \phi_\beta | \phi_\delta \rangle \delta_{JJ'} \delta_{M_J M_{J'}} \delta_{j_\beta j_\delta} \hat{j}\hat{J}_T \hat{j}\hat{J}_T' \\
\times \;& (-1)^{j_0 + J_T + 2j_\gamma + 2j + J_T' + J' + j_\alpha + j_\beta + \nu} \\
\times \;& \left\{ \begin{array}{ccc} j_0 & j_\delta & j \\ j_\gamma & J & J_T \end{array} \right\} \left\{ \begin{array}{ccc} j_0' & J_T' & J' \\ j & j_\gamma & \nu \end{array} \right\} \left\{ \begin{array}{ccc} j_\beta & j_\alpha & J_T' \\ \nu & j & j_0 \end{array} \right\} \\
\times \;& \langle j_0' || \boldsymbol{C}^\nu(0) || J_\gamma \rangle \langle J_\alpha || \boldsymbol{C}^\nu(1) || j_0 \rangle \\
\times \;& \int \mathrm{d}r_0 \int \mathrm{d}r_1 \Big[\sum_{\nu j} \frac{r_<^\nu}{r_>^{\nu+1}} \Big(\; f_{\kappa_0'}^U(r_0) \phi_{\kappa_\gamma}^U(r_0) + f_{-\kappa_0'}^L(r_0) \phi_{-\kappa_\gamma}^L(r_0) \; \Big) \\
\times \;& \Big(\; \phi_{\kappa_\alpha}^U(r_1) f_{\kappa_0}^U(r_1) + \phi_{-\kappa_\alpha}^L(r_1) f_{-\kappa_0}^L(r_1) \; \Big) \Big].
\end{aligned} \tag{4.34}$$

$V_{02}P_{01}$ matrix elements

The second exchange matrix element for each configuration pair is

$$\langle j_0' k_0'(0), \phi_\alpha(1)\phi_\beta(2)(J_T') : J' M_{J'} | V_{02} P_{01} | j_0 k_0(0), \phi_\gamma(1)\phi_\delta(2)(J_T) : J M_J \rangle, \tag{4.35}$$

where

$$V_{02} = \sum_{\nu} \frac{r_<^{\nu}}{r_>^{\nu+1}} \boldsymbol{C}^{\nu}(0) \cdot \boldsymbol{C}^{\nu}(2). \tag{4.36}$$

We apply P_{01} to the right hand side but this time it is convenient to recouple the angular momenta on the left hand side to obtain

$$\begin{aligned}
& \langle j_0' k_0'(0), \phi_\alpha(1)\phi_\beta(2)(J_T') : J' M_{J'} | V_{02} | j_0 k_0(1), \phi_\gamma(0)\phi_\delta(2)(J_T) : J M_J \rangle \\
= \;& \frac{1}{\pi} \sqrt{\frac{(\epsilon_{k'} + c^2)(\epsilon_k + c^2)}{\epsilon_{k'} \epsilon_k}} \langle \phi_\alpha | j_0 k_0 \rangle \hat{J}_T \hat{J}_T' \\
\times \;& (-1)^{j_0' + J_T' + j_\alpha + j_\beta + j_\gamma} \\
\times \;& \left\{ \begin{array}{ccc} j_0' & j_\beta & J_T \\ j_\alpha & J' & J_T' \end{array} \right\} \left\{ \begin{array}{ccc} j_0' & j_\beta & J_T \\ j_\delta & j_\gamma & \nu \end{array} \right\} \\
\times \;& \langle j_0' || \boldsymbol{C}^{\nu}(0) || j_\gamma \rangle \langle j_\beta || \boldsymbol{C}^{\nu}(2) || j_\delta \rangle \\
\times \;& \int \mathrm{d}r_0 \int \mathrm{d}r_2 \Big[\sum_{\nu} \frac{r_<^{\nu}}{r_>^{\nu+1}} \Big(\; f_{\kappa_0'}^U(r_0) \phi_{\kappa_\gamma}^U(r_0) + f_{-\kappa_0'}^L(r_0) \phi_{-\kappa_\gamma}^L(r_0) \; \Big) \\
\times \;& \Big(\; \phi_{\kappa_\beta}^U(r_2) \phi_{\kappa_\delta}^U(r_2) + \phi_{-\kappa_\beta}^L(r_2) \phi_{-\kappa_\delta}^L(r_2) \; \Big) \Big].
\end{aligned} \tag{4.37}$$

$V_{12}P_{01}$ matrix elements

The third exchange matrix element for each configuration pair is

$$\langle j_0' k_0'(0), \phi_\alpha(1)\phi_\beta(2)(J_T') : J' M_{J'} | V_{12} P_{01} | j_0 k_0(0), \phi_\gamma(1)\phi_\delta(2)(J_T) : J M_J \rangle, \tag{4.38}$$

where

$$V_{12} = \sum_{\nu} \frac{r_<^{\nu}}{r_>^{\nu+1}} \boldsymbol{C}^{\nu}(1) \cdot \boldsymbol{C}^{\nu}(2). \tag{4.39}$$

We apply P_{01} to the right hand side and recouple the angular momenta on the right hand side to obtain

$$\begin{aligned}
& \langle j_0' k_0'(0), \phi_\alpha(1)\phi_\beta(2)(J_T') : J' M_{J'} | V_{12} | j_0 k_0(1), \phi_\gamma(0)\phi_\delta(2)(J_T) : J M_J \rangle \\
= \;& \frac{1}{\pi} \sqrt{\frac{(\epsilon_{k'} + c^2)(\epsilon_k + c^2)}{\epsilon_{k'} \epsilon_k}} \langle j_0' k' | \phi_\gamma \rangle \hat{J}_T' \hat{J}_T \\
\times \;& (-1)^{2j_0 + J_T + j_\gamma + j_\beta} \\
\times \;& \left\{ \begin{array}{ccc} j_0 & j_\delta & J_T' \\ j_\gamma & J & J_T \end{array} \right\} \left\{ \begin{array}{ccc} j_\alpha & j_\beta & J_T' \\ j_\delta & j_0 & \nu \end{array} \right\} \\
\times \;& \langle j_\alpha || \boldsymbol{C}^{\nu}(1) || j_0 \rangle \langle j_\beta || \boldsymbol{C}^{\nu}(2) || j_\delta \rangle
\end{aligned}$$

$$\times \quad \int \mathrm{d}r_1 \int \mathrm{d}r_2 \Big[\sum_\nu \frac{r_<^\nu}{r_>^{\nu+1}} \Big(\ \phi^U_{\kappa_\alpha}(r_1) f^U_{\kappa_0}(r_1) + \phi^L_{-\kappa_\alpha}(r_1) f^L_{-\kappa_0}(r_1) \ \Big)$$
$$\times \quad \Big(\ \phi^U_{\kappa_\beta}(r_2) \phi^U_{\kappa_\delta}(r_2) + \phi^L_{-\kappa_\beta}(r_2) \phi^L_{-\kappa_\delta}(r_2) \ \Big) \Big]. \tag{4.40}$$

$(E - H_0 - H_1 - H_2)P_{01}$ matrix elements

The last exchange matrix element for each configuration interaction pair is

$$\begin{aligned} & \langle j'_0 k'_0(0), \phi_\alpha(1)\phi_\beta(2)(J'_T) : J' M_{J'} | (E - H_0 - H_1 - H_2) P_{01} \\ \times \quad & | j_0 k_0(0), \phi_\gamma(1)\phi_\delta(2)(J_T) : J M_J \rangle. \end{aligned} \tag{4.41}$$

We apply P_{01} to the right hand side to obtain

$$\begin{aligned} & \langle j'_0 k'_0(0), \phi_\alpha(1)\phi_\beta(2)(J'_T) : J' M_{J'} | (E - H_0 - H_1 - H_2) \\ \times \quad & | j_0 k_0(1), \phi_\gamma(0)\phi_\delta(2)(J_T) : J M_J \rangle \\ & = \frac{1}{\pi} \sqrt{\frac{(\epsilon_{k'} + c^2)(\epsilon_k + c^2)}{\epsilon_{k'} \epsilon_k}} \Big(\hat{J}'_T \hat{J}_T (-1)^{j_0 + J_T + j_\gamma + J'_T} \begin{Bmatrix} j_0 & j_\delta & J'_T \\ j_\gamma & J & J_T \end{Bmatrix} \\ & \times \Big[\langle \phi_\alpha | j_0 k \rangle \langle \phi_\beta | \phi_\delta \rangle \langle j'_0 k' | \phi_\gamma \rangle [E(1-\theta) - \epsilon_{k'} - \epsilon_k] \\ & - \langle \phi_\alpha | j_0 k \rangle \langle \phi_\beta | \phi_\delta \rangle \langle j'_0 k' | (V_0 - U_0) | \phi_\gamma \rangle \\ & - \langle j'_0 k' | \phi_\gamma \rangle \langle \phi_\beta | \phi_\delta \rangle \langle \phi_\alpha | (V_1 - U_1) | j_0 k \rangle \\ & - \langle j'_0 k' | \phi_\gamma \rangle \langle \phi_\alpha | j_0 k \rangle \langle \phi_\beta | (H_2) | \phi_\delta \rangle \Big] \\ & - E\theta \langle j'_0 k' | I_0^N | j_0 k \rangle \langle \phi_\beta | \phi_\delta \rangle \langle \phi_\alpha | \phi_\gamma \rangle \Big). \end{aligned} \tag{4.42}$$

The parameter θ has been introduced in a manner similar to the nonrelativistic case to ensure the numerical stability and uniqueness of the T matrix, as outlined by Fursa and Bray [34]. The projection operator $I_n^N = \sum_n |\phi_n\rangle\langle\phi_n|$ is made from the configuration interaction single particle states.

The numerical calculation of the V-matrix elements and the solution of the coupled relativistic Lippmann-Schwinger equations is achieved with a parallelized computer code that employs a hybrid OpenMP-MPI scheme. Standard ScaLAPACK routines [149] solve the set of linear equations (the coupled Lippmann-Schwinger equations) given by Eq. (4.22) for the T-

matrix elements. Calculations were done with 20 partial waves and then the analytical Born subtraction technique (see Chapter 2) was used to account for higher partial waves. Observables such as cross sections can be calculated from the T-matrix elements using the equations specified in Chapter 2.

4.3 Results

4.3.1 Integrated cross sections for excited states

As discussed in the previous section we have performed calculations in two models: RCC and RCCC. We found that for incident electron energies below 8 eV the inclusion of the continuum states made negligible difference to the calculated cross sections and so we will present only RCC results at these low energies.

We begin by presenting integrated cross sections for the $(6s6p)^3P^o_{0,1,2}$ states of mercury at low energies. Calculation of these cross sections at energies close to excitation threshold was not possible with the nonrelativistic CCC method. Fig. 5.1 shows the RCCC integrated cross section for the excitation of the $(6s6p)^3P^o_0$ triplet state. In the energy regime near the excitation threshold of these states the cross sections are dominated by the formation of negative ion (Hg^-) resonant states [150, 151]. There is excellent agreement between the RCCC results and the DBSR calculations of Zatsarinny and Bartschat [7]. The RCCC results are also generally in good agreement with the measurements of Hanne et al. [8]. Note, in Table 4.1 the RCCC energies for the triplet states slightly differ (< 0.12 eV) from the experimental values and therefore the position of the resonances had to be offset in the figures by the same amount in order to align with the experimental position of the resonances.

Fig. 4.2 shows the integrated cross section for excitation of the $(6s6p)^3P^o_1$ triplet state. The RCCC results are in very good agreement with both the DBSR calculations of Zatsarinny and Bartschat [7] and the measurements of Ottley and Kleinpoppen [9], and Erdevdi et al. [10].

The integrated cross section for excitation of the $(6s6p)^3P^o_2$ triplet state is shown in Fig. 4.3. Once again very good agreement is found between the RCCC results and DBSR results [7] and also the measurements of Hanne et al. [8], Newman et al. [11], Borst [12] and Krause et al. [13]; however in the region between 6.5 eV and 7.5 eV the RCCC results are slightly lower

than the DBSR results and experiment. We verified the convergence of our calculations at this energy region. A possible explanation for the discrepancy is likely to be related to the error in the $^1P_1^o - {}^3P_2$ energy difference for our target model which leads to a loss of flux to the $^1P_1^o$ state which opens at 0.25 eV below the correct energy.

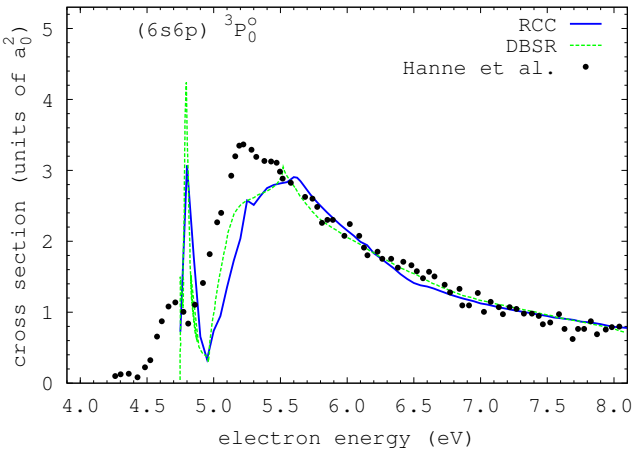

Figure 4.1: RCCC integrated excitation cross section for the $(6s6p)^3P_0^o$ state. Also shown are DBSR results [7], and experimental results due to Hanne et al. [8].

The integrated cross section for electron impact excitation of the singlet $(6s6p)^1P_1^o$ state is shown in Fig. 4.4. The difference between the RCC and RCCC calculations in this figure for intermediate and higher projectile energies gives an indication of the importance of coupling to the target continuum. The RCC calculation includes only the 29 discrete states and the cross section is higher by approximately 20% at the cross section maximum than that obtained by the full RCCC calculation. In the vicinity of 8.6 eV very small resonance structures are present in the $(6s6p)^1P_1^o$ cross section for both the RCCC and DBSR results.

In Fig. 4.5 we present integrated cross sections for the $(6s6p)^3P_1^o$ state over a large energy range. We can see a substantial difference between present RCCC results and nonrelativistic CCC results. This difference signifies the importance of an accurate account of relativistic effects for this transition. The present RCCC results are in good agreement with the experimental estimate of this cross section by Zubek et al. [15] and Panajotović

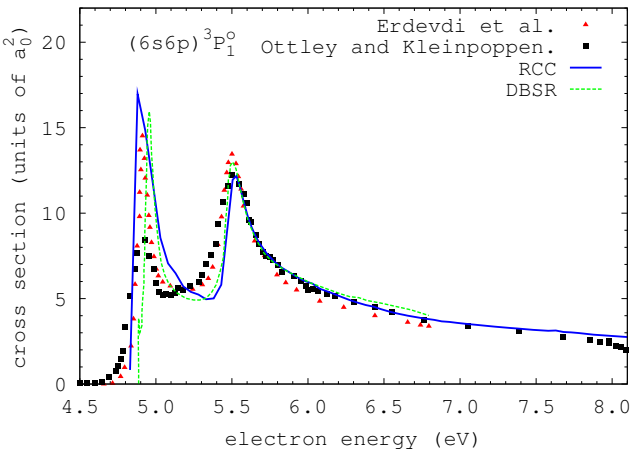

Figure 4.2: RCCC integrated excitation cross section for the $(6s6p)^3P_1^o$ state. Also shown are DBSR results [7], and experimental results due to Ottley and Kleinpoppen [9], and Erdevdi et al. [10].

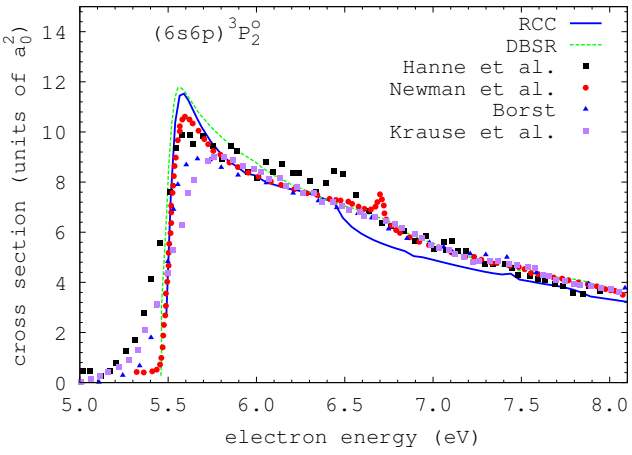

Figure 4.3: RCCC integrated excitation cross section for the $(6s6p)^3P_2^o$ state. Also shown are DBSR results [7], and experimental results due to Hanne et al. [8], Newman et al. [11], Borst [12], and Krause et al. [13].

et al. [16]. Similar to the nonrelativistic results we find that coupling to ionization channels plays a relatively minor role as RCCC and RCC results are close (except in the 20-40 eV energy range). However, interchannel coupling plays a major role for this transition. The first-order approximation cross section, labeled RCCC-Born in Fig. 4.5, will be strongly dependent on

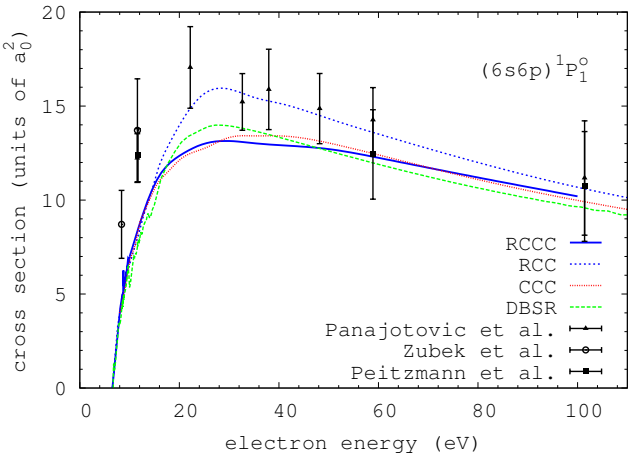

Figure 4.4: RCCC integrated excitation cross section for the singlet $(6s6p)^1P_1^o$ state. Also shown are nonrelativistic CCC results [14], DBSR results [7], and experimental results due to Zubek et al. [15], Panajotović et al. [16], and Peitzmann and Kessler [17].

the value for the optical oscillator strength. Given that the RCCC structure model for the $(6s6p)^3P_1^o - (6s^2)^1S^0$ transition has an optical oscillator strength value larger by about 50% than the experimental value, we find that the RCCC-Born result significantly overestimates the experiment. The good agreement between RCCC results and experiment is a confirmation that high-order scattering effects are dominant for this transition.

Integrated cross sections for excitation of the $(6s7s)^1S_0$ and $(6s7p)^1P_1^o$ states are presented in Fig. 4.6. We find good agreement with our previous nonrelativistic CCC calculations. For these much smaller cross sections the coupling to the ionization continuum proved to be significantly more important as comparison between RCCC and RCC results clearly shows. A similar conclusion was drawn on the basis of nonrelativistic CCC calculations [14]. We can conclude that for these states relativistic effects play a minor role.

4.3.2 Angle differential cross sections for elastic and inelastic scattering

Angle differential cross sections for elastic scattering from the $(6s^2)^1S_0$ ground state of mercury are presented in Fig. 4.7. While our previous non-

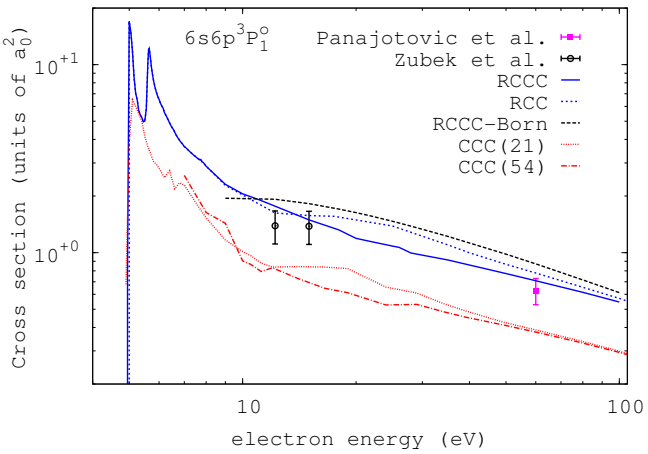

Figure 4.5: RCCC integrated excitation cross section for the singlet $(6s6p)^3P_1^o$ state. Also shown are nonrelativistic CCC results [14], experimental results due to Zubek et al. [15], Panajotović et al. [16], and Peitzmann and Kessler [17].

relativistic CCC calculations had difficulty in describing the elastic cross section at 15 eV (the minima were too deep), the RCCC differential cross section does not have such a problem and is in very good agreement with experiment [15] and also DBSR calculations [7]. As the incident electron energy increases to 25 and 35 eV we observe nearly perfect agreement between theoretical and experimental results [18]. At 9 eV we observe good agreement between all theoretical results and experiment at forward scattering angles. However, the region around the cross section minimum (100°-120°) proved to be particularly sensitive to the details of theoretical models, with none of the available theories being in agreement with experiment. In Fig. 4.8 we present angle differential cross sections at 15 and 60 eV for the$(6s6p)^3P_1^o$ and $(6s6p)^1P_1^o$ states. Excellent agreement is obtained with the measurements of Zubek et al. [15] for the $(6s6p)^1P_1^o$ and $(6s6p)^3P_1^o$ states at 15 eV. It is well known that the cross section for the $(6s6p)^1P_1^o$ state is strongly dependent on the accuracy of the optical oscillator strength for this transition [14] with channel coupling effects playing a rather minor role. For the $(6s6p)^3P_1^o$ state the situation apparently is quite different. The optical oscillator strength values in RCCC and DBSR calculations differ by a factor of two (0.038 and 0.018, respectively), however a similar difference in

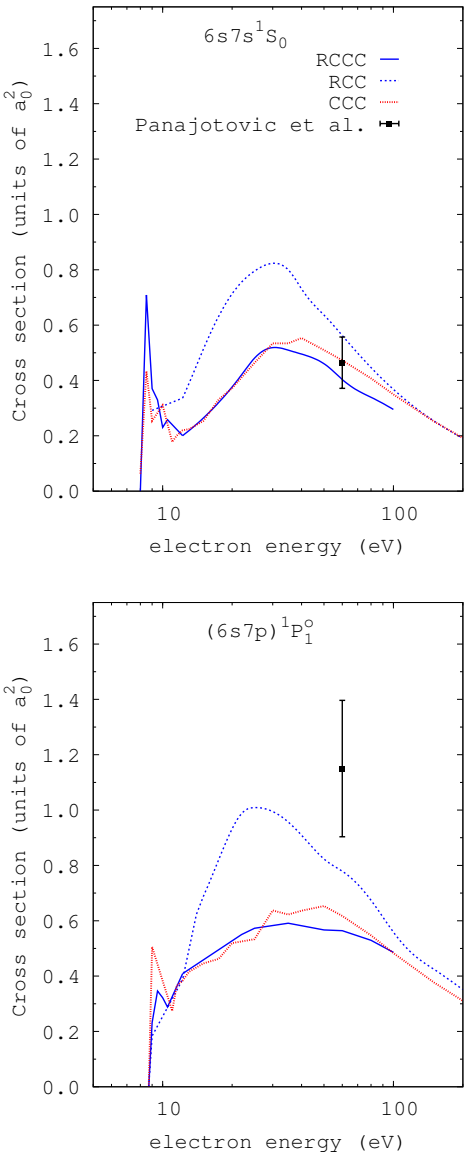

Figure 4.6: RCCC and nonrelativistic CCC [14] integrated cross sections for excitation of the $(6s7s)^1S_0$ and $(6s7p)^1P_1^o$ states. Experiment is due to Panajotović et al. [16].

differential cross sections can be observed only at forward scattering angles. Due to a small value of optical oscillator strength for this intercombinational transition an adequate account of the interchannel coupling becomes more important. Additionally, the difference between nonrelativistic and present

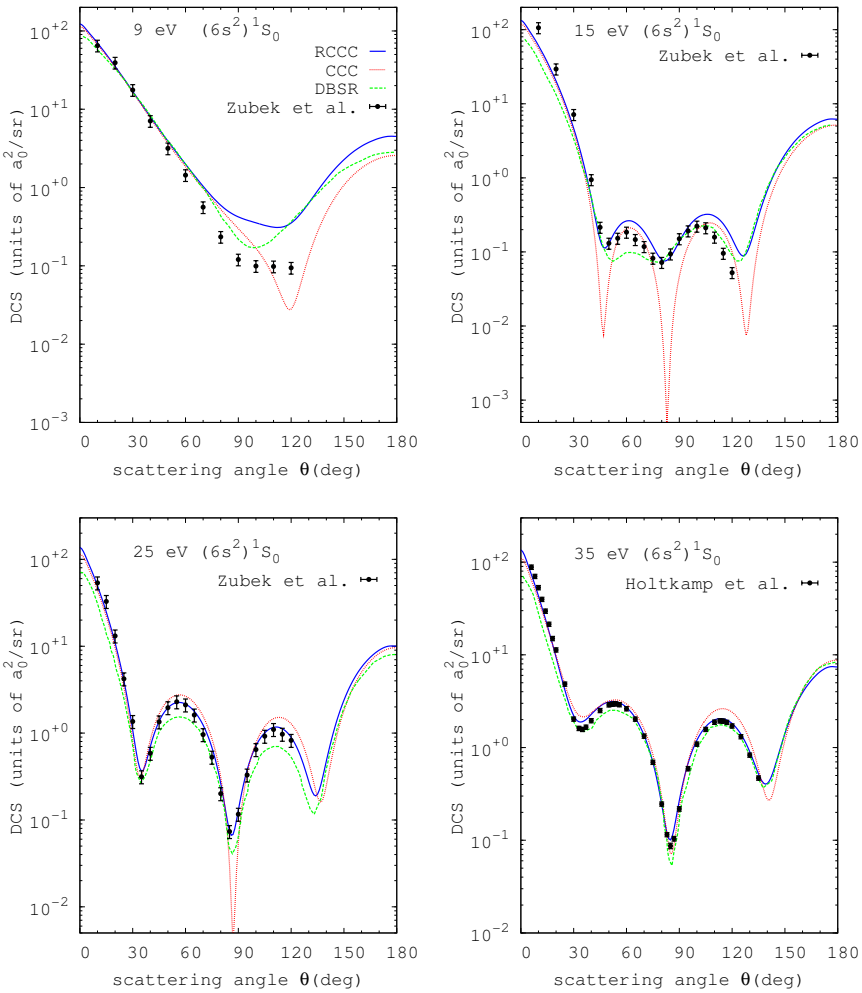

Figure 4.7: RCCC angle differential cross sections for elastic scattering from the $(6s^2)^1S_0$ ground state. Also shown are nonrelativistic CCC results [14], DBSR results [7], and experimental results due to Zubek et al. [15] and Holtkamp et al. [18].

relativistic RCCC results for this transition is an indication of the importance of an accurate treatment of relativistic effects in the calculation of target wave functions and the scattering process. As the incident electron energy increases to 60 eV we observe perfect agreement between all theoretical models (RCCC, CCC, DBSR) and experiment for the $(6s6p)^1P_1^o$ state.

For the $(6s6p)^3P_1^o$ state theoretical results are in good agreement except for small scattering angles, while the experimental results of Panajotović et al. [16] seem to be systematically higher. This situation is interesting as it contradicts the usual assumption that at this relatively large energy the singlet component of the target wave function would be dominant and therefore the $(6s6p)^1P_1^o$ and $(6s6p)^3P_1^o$ state cross sections are related simply by a multiplicative constant. It is worthwhile to note that this constant is not just a ratio of optical oscillator strength (1.16 and 0.024 are the experimental values for the $(6s6p)^1P_1^o$ and $(6s6p)^3P_1^o$ states respectively) as the difference in excitation thresholds should be also taken into account, which produces a cross section ratio coefficient of 18.7 (strictly valid for forward scattering only). However, rescaled in this way, the $(6s6p)^1P_1^o$ cross section of Panajotović et al. [16] would be lower than their measured $(6s6p)^3P_1^o$ state cross section, except for forward scattering angles. We note also that as the RCCC value for the $(6s6p)^3P_1^o$ state optical oscillator strength (0.038) is larger than the experimental value (0.024), and the DBSR value (0.018) is smaller than the experimental value, one would expect that the RCCC differential cross section for the $(6s6p)^3P_1^o$ state would overestimate the experiment while the DBSR results would underestimate it. In fact this behavior is observed only at small scattering angles. This suggests that channel coupling effects are still important at intermediate and large scattering angles at 60 eV and that they are captured adequately by the present theoretical methods. On the other hand the measurements of the $(6s6p)^3P_1^o$ state differential cross section [16] seem to be too high and a fresh look at the normalization procedure appears to be warranted.

In Fig. 4.9 we present differential cross sections for $(6s6p)^3P_0^o$ and $(6s6p)^3P_2^o$ states at 15 eV. We can see that nonrelativistic and relativistic CCC results are in reasonably good agreement, which supports the conclusion made by Fursa et al. [14] that this transition is governed mostly by the exchange scattering. Our results are in good agreement with measurements of Zubek et al. [15]. The results of DBSR calculations are somewhat larger than our results and experiment, which as discussed in [7] is most likely related to the lack of coupling to ionization channels in the DBSR model.

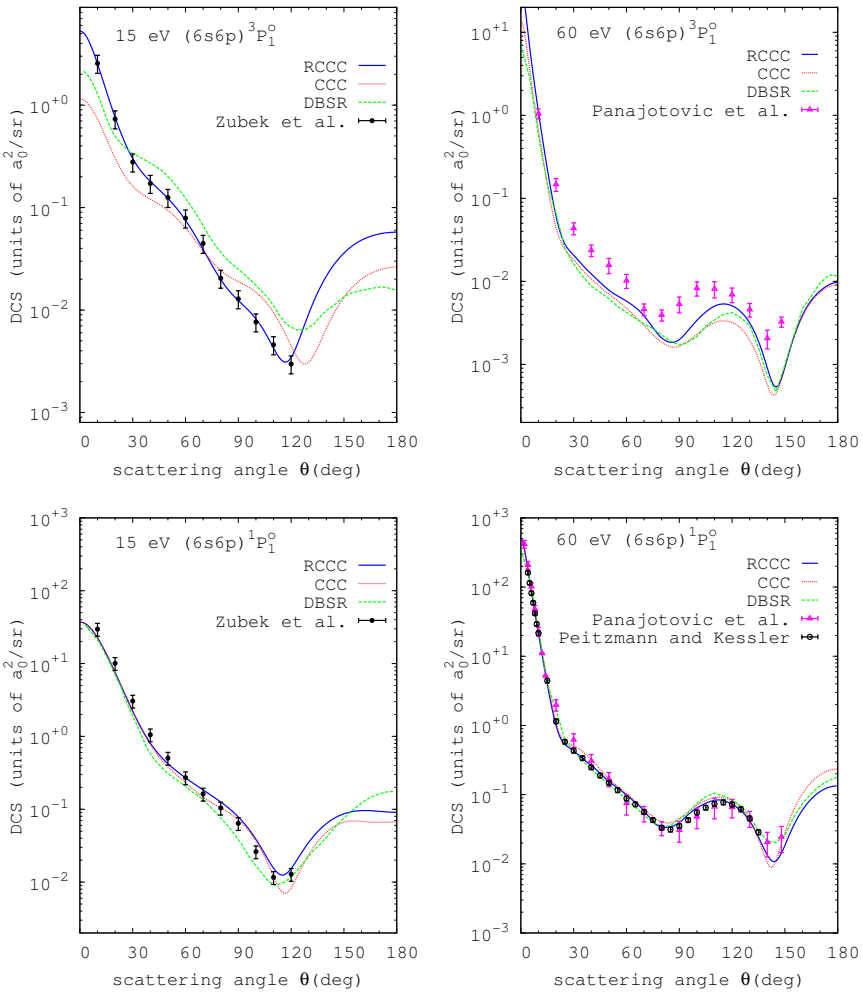

Figure 4.8: RCCC angle differential cross sections at 15 and 60 eV for the $(6s6p)^3P_1^o$ state and $(6s6p)^1P_1^o$ state. Also shown are nonrelativistic CCC results [14], DBSR results [7], and experiment due to Zubek et al. [15], Panajotović et al. [16], and Peitzmann and Kessler [17].

RCCC angle differential cross sections for the $(6s7s)^1S_0$ and $(6s7p)^1P_1^o$ states at 60 eV are shown in Fig. 4.10. The differential cross section for the $(6s7s)^1S_0$ state measured by Panajotović et al. [16] displays three minima which both the RCCC and CCC calculations predict in very good agreement with experiment [16]. Interestingly, both the RCCC and CCC differential

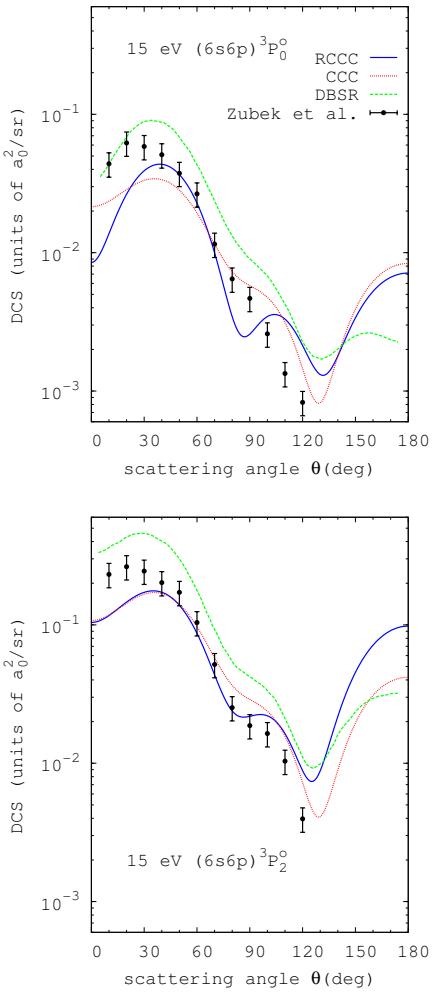

Figure 4.9: RCCC angle differential cross sections at 15 eV for the $(6s6p)^3P_0^o$ and $(6s6p)^3P_2^o$ states. Also shown are nonrelativistic CCC results [14], DBSR results [7], and experimental results due to Zubek et al. [15].

cross sections predict a very sharp first minimum. In contrast to the elastic scattering cross section (e.g., 15 eV) this appears to be a genuine feature which might be difficult to obtain experimentally due to finite angular resolution. The RCCC and CCC results are in excellent agreement for the differential cross section of the $(6s7p)^1P_1^o$ state and are also in excellent agreement with experiment [16], except for the angles near 150 degrees at

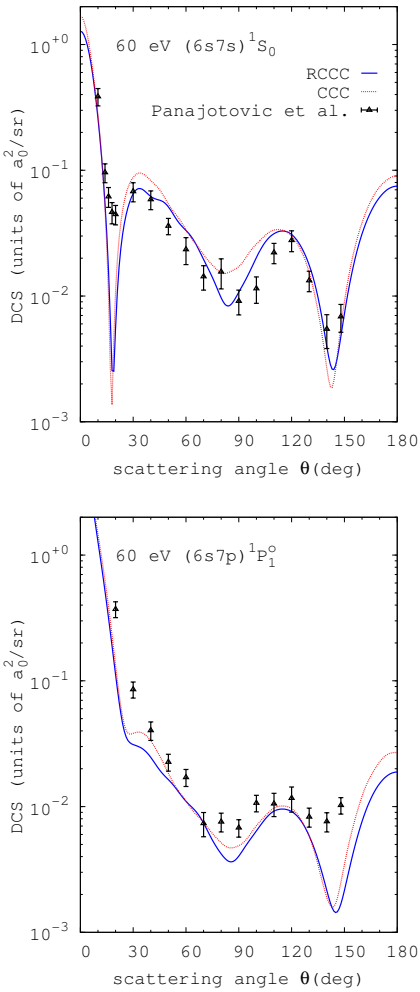

Figure 4.10: RCCC angle differential cross sections at 60 eV for the $(6s7s)^1S_0$ and $(6s7p)^1P_1^o$ states. Also shown are nonrelativistic CCC results [14] and experiment due to Panajotović et al. [16]

the second minimum in the cross section where the RCCC results are lower than the experimental values in the region of the minimum.

4.3.3 Total, elastic, and momentum transfer cross sections

In Fig. 4.11 we present the total cross section for electron scattering from the $(6s^2)^1S_0$ ground state of mercury, that is, the summed contribution from elastic, excitation and ionization channels. We find that at energies above 2 eV the RCCC, CCC and DBSR calculations are in excellent agreement with each other. We have also presented in this figure (below 4 eV) results of calculations by McEachran and Elford [21] who used the polarized orbitals method with addition of a dynamic distortion potential (labeled RDD). At low energies all theoretical results have qualitatively similar behavior (maximum at about 0.4-0.5 eV) but show large variations in the cross section shape and absolute values. The difficulties in a theoretical description of low-energy e-Hg scattering have been recently highlighted by Zatsarinny and Bartschat [7] and the present theoretical results should be considered with a degree of caution. The experiment of Jost and Ohnemus [19] shows good qualitative agreement with the RCCC results in terms of the shape of the cross section and location of minima and maxima, however the experimental cross section is consistently larger across all energies.

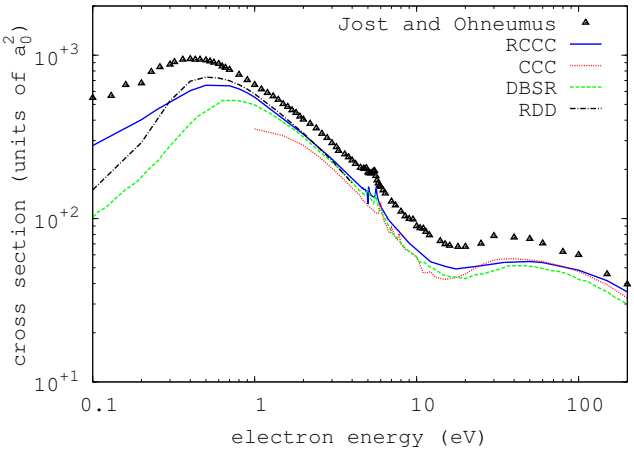

Figure 4.11: RCCC total cross section for scattering from the $(6s^2)^1S_0$ ground state of mercury. Also shown are nonrelativistic CCC results [14], DBSR results [7], and experiment due to Jost and Ohnemus [19].

In Fig. 4.12 we present the elastic cross section. We find good agreement between the RCCC and CCC results and very good agreement with experimental estimates of elastic cross sections of Holtkamp et al. [18], Panajotović

et al. [16] and Zubek et al. [20]. Compared to other calculations, we note that the cross section minimum at 20 eV in RCCC calculations is much shallower than in the DBSR and RDD models and in better agreement with experiment.

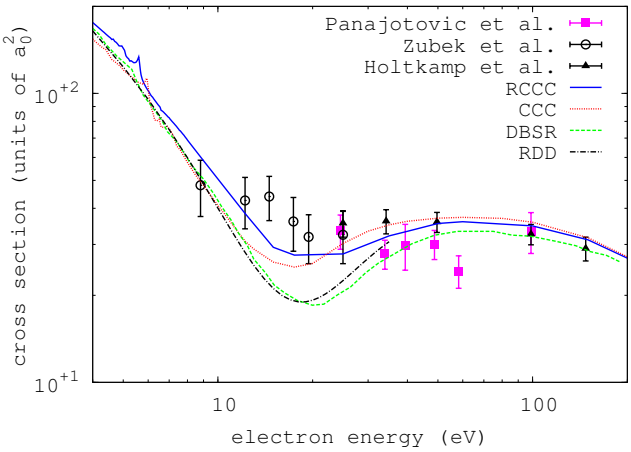

Figure 4.12: RCCC elastic cross section for scattering from the $(6s^2)^1S_0$ ground state of mercury. Also shown are nonrelativistic CCC results [14], DBSR results [7], and experimental results due to Panajotović et al. [16], Zubek et al. [20], and Holtkamp et al. [18].

The RCCC elastic momentum transfer cross section for electron scattering on the ground state of mercury is presented in Fig. 4.13. At low energies, similar to the elastic integrated cross section, there is wide variation in the results of theoretical methods. The results of the RDD method are in excellent agreement with the experiment of England and Elford [22] for the momentum transfer cross section but, interestingly, not for the integrated cross section. This suggests a possible inconsistency between the measurements of Jost and Ohnemus [19] and England and Elford [22]. At energies above 1 eV RCCC, CCC, DBSR and RDD results are in good agreement. Compared to experimental estimates of Panajotović et al. [16] we find that apart from the two lowest experimental points (at 15 eV and 25 eV) the experiment is systematically lower than the theoretical results.

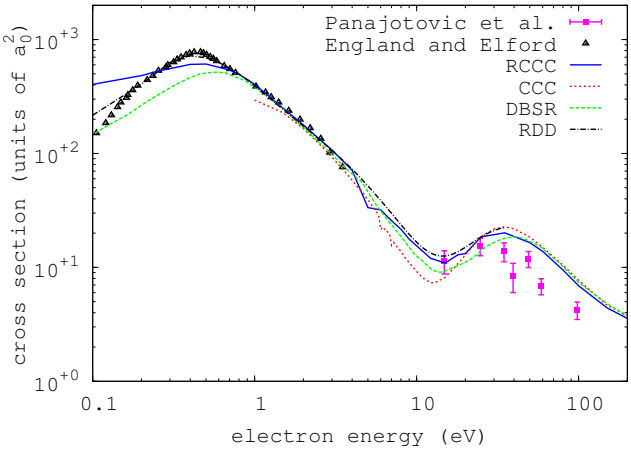

Figure 4.13: RCCC elastic momentum transfer section for scattering from the $(6s^2)^1S_0$ ground state of mercury. Also shown are results of nonrelativistic CCC [14], DBSR [7] and RDD [21] calculations and experimental results due to England and Elford [22], and Panajotović et al. [16].

Chapter 5

Hybrid OpenMP-MPI Parallelization

In April 2010 the National Computational Infrastructure Facility commissioned a new supercomputer, a Sun/Oracle 'Vayu' system with over 11900 cpus. In order to run the RCCC code (approximately 40000 lines of Fortran) on the Vayu system a significant modification of the code was required: the parallelization scheme had to be converted from a pure OpenMP parallelization scheme based on shared memory, to a hybrid OpenMP-MPI parallelization scheme that employed both shared and distributed memory. This parallelization represents an emerging trend for using high performance supercomputing architectures.

Figure 5.1: The Vayu system: 11936 cpus in 1492 nodes with 8 cpus per node. Each node contains 24GB memory except for 48 nodes which have 48GB. Peak performance is 140TFlops

The cpus in the Vayu system are grouped into 'nodes', with 8 cpus per node. Each cpu has approximately 3GB of memory, therefore 24GB of memory is available on a single node. This 24GB can be shared by the processors on a single node, and therefore RCCC calculations requiring less than or equal to 24GB can be run on a single node using an OpenMP shared memory parallelization scheme. However for larger calculations with memory requirements exceeding 24GB, communication between nodes is necessary and this is not possible with OpenMP. Instead, MPI must be employed, where MPI stands for 'Message Passing Interface'. MPI can be thought of as the "assembly language" of parallel computing because explicit send and receive instructions between specified cpus can be implemented: it can be used on distributed memory systems with any number of processors. OpenMP on the other hand relies on shared memory and would be restricted to only 8 processors in a given node on the Vayu system. The disadvantage of using MPI is that existing code often has to be completely restructured if an MPI parallelization paradigm is to be employed. Parallelization with OpenMP, on the other hand is straightforward and achieved with a few simple directives.

MPI parallelization requires each cpu to run a copy of the program. Each cpu then performs different tasks in parallel, as required. This automatically presented a problem because each processor only has 3GB of available memory, whereas the RCCC program often exceeds this when the target structure and continuum waves are calculated. The solution to this issue was to employ a hybrid OpenMP-MPI parallelization scheme, where the first processor of every node calculates the target structure and continuum waves, given that the first processor of each node can utilize the full 24GB of available shared memory on each node. The next step in the process is to split the channel pairs evenly across the nodes, and then employ OpenMP parallelization *within* each node to calculate the V matrix elements. Following this, the system of linear equations (the Lippmann-Schwinger equation for the scattering system) is solved using MPI parallelization by employing ScaLAPACK routines [149]: in this step *all* the processors across *all* nodes are employed. The solution to the system of linear equations gives the T matrix elements for the scattering problem.

Finally, after the T matrix elements are calculated, the first process of the first node is used to calculate observable quantities, such as cross sections,

from the T matrix elements.

A schematic algorithm of the hybrid OpenMP-MPI parallelization scheme for the RCCC code is outlined below. A note on terminology: usually one processor is associated with one MPI process, but this is variable.

Algorithm for Hybrid OpenMP-MPI RCCC

1. Call 'm' nodes, with 'n' processes per node.
2. **First process of each node** calculates target wavefunctions and continuum wavefunctions.
3. **Begin do loops** over total angular momentum and parity for the scattering system:
   (a) Channel pairs are calculated and distributed evenly among the nodes.
   (b) **Using OpenMP multithreading** within each node, calculate the V matrix elements for the channel pairs within each node.
   (c) **Using MPI message passing**, solve the system of linear equations (the Lippmann-Schwinger equations) using ScaLAPACK routines that employ all processes across all nodes.
   (d) **Using only the first process of the first node**, calculate observables such as partial wave cross sections from the T matrix elements, and print V matrix elements, T matrix elements, and observables to file.
4. **End do loops** over total angular momentum and parity.
5. **Using only the first process of the first node**, calculate the total cross section and other observables, and write to file.

The memory requirements for a calculation can be estimated by calculating the size of the largest arrays used in the RCCC code. There are three such arrays: (1) arrays that store the target wavefunctions, (2) arrays that store the continuum wavefunctions, and (3) the arrays that store the V-matrix elements. Both the target wavefunctions and continuum wave functions have upper and lower components due to the use of relativistic

Dirac spinors. These array elements are declared as double-precision (8 bytes) and therefore the memory requirements can be calculated with the equations listed in Table 5.1.

Array	Variable Type	Memory (GB)
Target wavefunctions	real	$\frac{n_t \times n_r \times 2 \times 8}{10^9}$
Continuum wavefunctions	real	$\frac{n_c \times n_r \times 2 \times 8}{10^9}$
V-matrix	real	$\frac{n_c \times n_c \times 8}{10^9}$

Table 5.1: Memory requirements for the largest arrays in the RCCC code, where n_t is the number of target wavefunctions, n_c is the number of continuum wavefunctions, n_r is the number of radial grid points, and each double precision real array element requires 8 bytes of memory. The factor of 2 in the target and continuum wavefunction memory requirements is due to the fact that each relativistic wavefunction has upper and lower components.

The hybrid OpenMP-MPI scheme will use the above three arrays as follows:

1. The target and continuum wavefunction memory requirements will be *replicated* on each node.

2. The V-matrix memory requirements will be *distributed* across the nodes.

That is, for m nodes, the total memory for these three arrays will be

$$\begin{aligned} & m \times (\text{memory for target wavefunctions}) \\ + \quad & m \times (\text{memory for continuum wavefunctions}) \\ + \quad & (\text{memory for } V \text{ matrix elements}) \end{aligned} \tag{5.1}$$

In the ScaLAPACK routines additional large temporary arrays will be allocated when the V-matrix array is distributed across all processes in block-cyclic format for the most efficient solution of the system of linear equations. These additional temporary arrays will have memory requirements equivalent to the V-matrix array.

The primary goal of the conversion from OpenMP to the hybrid OpenMP-MPI scheme was not to perform a given calculation faster using more cpus, but instead to allow calculations with memory requirements

greater than the 24GB available on one node to run at all. This is particularly necessary for two-electron targets where a large number of configurations are possible for the target states. Nevertheless, the conversion to a hybrid OpenMP-MPI scheme has not only enabled large calculations to be performed, but calculations of a given size can also be performed in less time if more cpus are used. Table 5.2 illustrates the decrease in time for the calculation of V-matrix elements and solution of the linear equations using ScaLAPACK routines for a test calculation. The test calculation involved the zeroth partial wave for electron scattering on a two-electron target with 301 target states. The V matrix size was 37944×37944.

Table 5.2: Time for calculation of V-matrix elements and ScaLAPACK routines for a test calculation.

No. cpus	V-matrix elements (s)	ScaLAPACK routines (s)
8	3194	450
16	1545	230
24	1020	162

Compared to the initial calculation using 8 cpus, this illustrates that increasing the number of cpus by a factor of 2 (i.e. 16 cpus) reduces the computation time both for the V-matrix elements and ScaLAPACK routines by approximately a factor of 2. Similarly, increasing the number of cpus by a factor of 3 (i.e. 24 cpus) reduces the computational times by a factor of approximately 3.

Chapter 6

Conclusion

Three main accomplishments have been demonstrated in this thesis:

- The relativistic convergent close-coupling method has been extended to include the Breit and Møller interactions. The method has been applied to calculation of the polarization of the Lyman-α_1 line of Ti^{21+}, Ar^{17+}, and Fe^{25+} ions. We have shown that account of the Breit relativistic correction to the Coulomb interaction resolves the discrepancy between theory and EBIT experiments [2, 3]. Predictions for U^{91+} polarization of the Lyman-α_1 line have been presented. Large differences between calculations with Coulomb, Breit and Møller potentials have been found. We have verified the accuracy of our electron-U^{91+} scattering calculations that include Breit and Møller relativistic corrections by finding good agreement with U^{91+} 1s ionization cross section measurements of Marrs et al. [6] and previous first-order calculations.

- The RCCC method has been extended to accommodate quasi two-electron targets and the theory has been applied to electron scattering from mercury which is modeled as an atom with two active valence electrons above an inert ion core. Comparison with our previous study of electron-Hg scattering using the non-relativistic CCC method [14] confirmed the accuracy of the presented results for most of the considered transitions. In a number of cases where there was discrepancy between CCC and experimental results (e.g., elastic DCS at 15 eV and ICS for $(6s6sp)^3P_1^o$ state) we find that the fully relativistic approach is in much better agreement with experiment. For scattering at energies close to $(6s6p)^3P_{0,1,2}^o$ state thresholds, where non-relativistic methods

like CCC cannot be applied, our RCCC method finds very good agreement with DBSR calculations and experiment.

- The third main accomplishment was the conversion of the RCCC computer code from an OpenMP to a hybrid OpenMP-MPI parallelization scheme. This allowed for large calculations to be performed on the Vayu 11900 cpu computer at the National Computational Infrastructure Facility. Scaling of the computational time has also been demonstrated: increasing the number of cpus by a factor of 'n' decreases the computational time for the V-matrix elements and ScaLAPACK routines by a corresponding factor of 'n'.

The extended capabilities of the RCCC method are of interest to researchers in Germany and the USA. Theory and experiment both play vital roles in the development of scattering techniques, and the RCCC method provides a solid theoretical foundation for scattering processes involving a wide range of electron projectile energies and a wide range of atomic and ionic targets.

Appendix A

Normalization of Relativistic Partial Waves

Considering the normalization of positive energy free continuum states, we need to show

$$\begin{aligned}\langle \boldsymbol{k}\mu + | \boldsymbol{k}'\mu' + \rangle &= \delta_{\mu\mu'}\delta(\boldsymbol{k}-\boldsymbol{k}') \\ &= \delta_{\mu\mu'}\frac{1}{k^2}\delta(k-k')\delta(\Omega_{\boldsymbol{k}}-\Omega_{\boldsymbol{k}'}),\end{aligned} \tag{A.1}$$

where

$$\int \delta(\boldsymbol{k})\mathrm{d}^3\boldsymbol{k} = 1, \tag{A.2}$$

and

$$\mathrm{d}^3\boldsymbol{k} = k^2\mathrm{d}k\mathrm{d}\Omega_{\boldsymbol{k}}, \tag{A.3}$$

$$\mathrm{d}\Omega_{\boldsymbol{k}} = \sin\theta\mathrm{d}\theta\mathrm{d}\phi, \tag{A.4}$$

$$\delta(\boldsymbol{k}) = \frac{1}{k^2}\delta(k)\delta(\Omega_{\boldsymbol{k}}), \tag{A.5}$$

$$\delta(\Omega_{\boldsymbol{k}}) = \frac{\delta(\theta)\delta(\phi)}{\sin\theta}. \tag{A.6}$$

Now

$$\langle \boldsymbol{k}\mu + | \boldsymbol{k}'\mu' + \rangle = \int \mathrm{d}^3\boldsymbol{r}\langle \boldsymbol{k}\mu + | \boldsymbol{r}\rangle\langle \boldsymbol{r}| \boldsymbol{k}'\mu' + \rangle, \tag{A.7}$$

and we use

$$\begin{aligned}\langle \boldsymbol{r}|\boldsymbol{k}\mu+\rangle &= \sum_{\kappa m_j}\left[\mathrm{i}^l C^{jm_j}_{l(m_j-\mu)\frac{1}{2}\mu} Y_l^{m_j-\mu}(\hat{\boldsymbol{k}})\right]\left[\sqrt{\frac{2}{\pi}}\sqrt{\frac{\epsilon_k+c^2}{2\epsilon_k}}\right] \\ &\times \begin{pmatrix} j_l(kr)\chi_\kappa^{m_j} \\ \frac{\mathrm{i}ckS_\kappa}{\epsilon_k+c^2} j_{\bar{l}}(kr)\chi_{-\kappa}^{m_j}\end{pmatrix},\end{aligned} \tag{A.8}$$

to obtain

$$\begin{aligned}\langle \boldsymbol{k}\mu+|\boldsymbol{k}'\mu'+\rangle &= \int \mathrm{d}^3\boldsymbol{r}\sum_{\kappa m_j}\left[(-\mathrm{i})^l C^{jm_j}_{l(m_j-\mu)\frac{1}{2}\mu} Y_l^{m_j-\mu}(\hat{\boldsymbol{k}})\right]\left[\sqrt{\frac{2}{\pi}}\sqrt{\frac{\epsilon_k+c^2}{2\epsilon_k}}\right] \\ &\times \left(j_l(kr)\chi_\kappa^{m_j\dagger}, \tfrac{-\mathrm{i}ckS_\kappa}{\epsilon_k+c^2} j_{\bar{l}}(kr)\chi_{-\kappa}^{m_j}\right) \\ &\times \sum_{\kappa' m_{j'}}\left[\mathrm{i}^{l'} C^{j'm_{j'}}_{l'(m_{j'}-\mu')\frac{1}{2}\mu'} Y_{l'}^{*m_{j'}-\mu'}(\hat{\boldsymbol{k}}')\right]\left[\sqrt{\frac{2}{\pi}}\sqrt{\frac{\epsilon_{k'}+c^2}{2\epsilon_{k'}}}\right] \\ &\times \begin{pmatrix} j'_l(k'r)\chi_{\kappa'}^{m_{j'}} \\ \frac{\mathrm{i}ck'S_{\kappa'}}{\epsilon_{k'}+c^2} j_{\bar{l'}}(k'r)\chi_{-\kappa'}^{m_{j'}}\end{pmatrix}.\end{aligned} \tag{A.9}$$

Now using $\mathrm{d}^3\boldsymbol{r} = r^2\mathrm{d}r\mathrm{d}\Omega_{\boldsymbol{r}}$ and the following expressions

$$\chi_\kappa^{m_j} = \sum_\mu C^{jm_j}_{lm_l\frac{1}{2}\mu} Y_l^{m_j-m_s}(\hat{\boldsymbol{r}})\chi^\mu, \tag{A.10}$$

$$\sum_{jm_j} C^{jm_j}_{lm_l\frac{1}{2}\mu} C^{jm_j}_{l'm_{l'}\frac{1}{2}\mu'} = \delta_{m_l,m_{l'}}\delta_{\mu,\mu' a}, \tag{A.11}$$

and

$$\int Y_{l'}^{m_{l'}}(\hat{\boldsymbol{r}}) Y_l^{m_l}(\hat{\boldsymbol{r}})\mathrm{d}\Omega_{\boldsymbol{r}} = \delta_{l'l}\delta_{m_l,m_{l'}a}, \tag{A.12}$$

we obtain

$$\begin{aligned}\langle \boldsymbol{k}\mu+|\boldsymbol{k}'\mu'+\rangle &= \delta_{\mu\mu'}\int r^2\mathrm{d}r\sum_{\kappa m_j}\left[(-\mathrm{i})^l Y_l^{*m_j-\mu}(\hat{\boldsymbol{k}})\right]\left[\sqrt{\frac{2}{\pi}}\sqrt{\frac{\epsilon_k+c^2}{2\epsilon_k}}\right] \\ &\times \left(j_{l'}(kr), \tfrac{-\mathrm{i}ckS_{\kappa'}}{\epsilon_k+c^2} j_{\bar{l'}}(kr)\right) \\ &\times \left[(\mathrm{i})^l Y_l^{*m_j-\mu'}(\hat{\boldsymbol{k}}')\right]\left[\sqrt{\frac{2}{\pi}}\sqrt{\frac{\epsilon_{k'}+c^2}{2\epsilon_{k'}}}\right]\begin{pmatrix} j_l(k'r) \\ \frac{\mathrm{i}ck'S_\kappa}{\epsilon_{k'}+c^2} j_{\bar{l}}(k'r)\end{pmatrix}.\end{aligned} \tag{A.13}$$

Now we use

$$\sum_{lm_l} Y_l^{m_l}(\hat{\boldsymbol{k}}) Y_l^{*m_l}(\hat{\boldsymbol{k}}') = \delta(\Omega_{\boldsymbol{k}} - \Omega_{\boldsymbol{k}'}), \tag{A.14}$$

and

$$\frac{2}{\pi} \int r^2 \mathrm{d}r j_l(kr) j_{l'}(k'r) = \frac{1}{k^2} \delta(k - k'), \tag{A.15}$$

to obtain

$$\begin{aligned}
\langle \boldsymbol{k}\mu + | \boldsymbol{k}'\mu' + \rangle &= \delta_{\mu\mu'} \frac{1}{k^2} \delta(k - k') \delta(\Omega_{\boldsymbol{k}} - \Omega_{\boldsymbol{k}'}) \frac{\epsilon_k + c^2}{2\epsilon_k} \\
&\quad \times \left(1 + \frac{c^2 k^2}{(\epsilon_k + c^2)^2} \right) \\
&= \delta_{\mu\mu'} \frac{1}{k^2} \delta(k - k') \delta(\Omega_{\boldsymbol{k}} - \Omega_{\boldsymbol{k}'}) \frac{\epsilon_k + c^2}{2\epsilon_k} \\
&\quad \times \left(\frac{\epsilon_k^2 + 2\epsilon_k c^2 + c^4 + c^2 k^2}{(\epsilon_k + c^2)^2} \right) \\
&= \delta_{\mu\mu'} \frac{1}{k^2} \delta(k - k') \delta(\Omega_{\boldsymbol{k}} - \Omega_{\boldsymbol{k}'}) \frac{\epsilon_k + c^2}{2\epsilon_k} \\
&\quad \times \left(\frac{\epsilon_k^2 + 2\epsilon_k c^2 + \epsilon_k^2}{(\epsilon_k + c^2)^2} \right) \\
&= \delta_{\mu\mu'} \frac{1}{k^2} \delta(k - k') \delta(\Omega_{\boldsymbol{k}} - \Omega_{\boldsymbol{k}'})
\end{aligned} \tag{A.16}$$

as required.

Appendix B

Partial Wave Relativistic Lippmann-Schwinger Equation

In Eq. (2.44) a factor of

$$(-i)^L (i)^{L'} e^{i\eta_\kappa} e^{i\eta_{\kappa'}} \sqrt{\frac{\epsilon_k + c^2}{\pi \epsilon_k}} \sqrt{\frac{\epsilon_{k'} + c^2}{\pi \epsilon_{k'}}}, \tag{B.1}$$

with $\eta_\kappa = \sigma_\kappa + \delta_\kappa$, was absorbed into the matrix element for convenience of presentation. Here a complete derivation of the partial-wave Lippmann-Schwinger equation is presented in which all such factors (and also factors of 2, π etc) are kept; this enables comparison with the computer code.

In equation Eq. (2.41) we absorb the factor of $\frac{1}{r}$ into the ket $|u^m_{\kappa,k}\rangle$ to obtain

$$|\boldsymbol{k}^{(\pm)}\mu+\rangle \;=\; \sqrt{\frac{\epsilon_k + c^2}{\pi \epsilon_k}} \sum_{\kappa,m} i^L C^{jm}_{Lm-\mu,\frac{1}{2}\mu} Y^{*m-\mu}_L(\boldsymbol{k}) e^{\pm i(\sigma_\kappa+\delta_\kappa)} \frac{1}{k} |u^m_{\kappa,k}\rangle, \tag{B.2}$$

A partial wave expansion for the V matrix elements in terms of positive energy continuum waves can be performed as follows

$$\langle \boldsymbol{k}^{(-)}_f \mu_f + \phi_f | V | \boldsymbol{k}^{(+)}_i \mu_i + \phi_i \rangle \;=\; \frac{2}{\pi} \frac{1}{k_i k_f} \sqrt{\frac{\epsilon_f + c^2}{2\epsilon_f}} \sqrt{\frac{\epsilon_i + c^2}{2\epsilon_i}}$$

$$
\begin{aligned}
&\times \sum_{\kappa_f m_{j_f} \kappa_i m_{j_i}} \Bigg[\left(\mathrm{e}^{-\mathrm{i}(\delta_{\kappa_f}+\sigma_{\kappa_f})} \right)^* \mathrm{e}^{\mathrm{i}(\delta_{\kappa_i}+\sigma_{\kappa_i})} \\
&\times (-\mathrm{i})^{l_f} \mathrm{i}^{l_i} C^{j_f m_{j_f}}_{l_f m_{l_f} \frac{1}{2} \mu_f} C^{j_i m_{j_i}}_{l_i m_{l_i} \frac{1}{2} \mu_i} \\
&\times Y_{l_f}^{m_{j_f}-\mu_f}(\hat{\boldsymbol{k}}_f) Y_{l_i}^{*m_{j_i}-\mu_i}(\hat{\boldsymbol{k}}_i) \\
&\times \langle u_{\kappa_f m_{j_f}} \phi_f | V | u_{\kappa_i m_{j_i}} \phi_i \rangle \Bigg].
\end{aligned}
\tag{B.3}
$$

We couple the target state and projectile state to a total angular momentum state $|\Pi J M_J\rangle$ where J and M_J are the total angular momentum of the scattering system and its projection, $\Pi = \pi(-1)^L$ is the total parity, with π the parity of the target state

$$
\begin{aligned}
\langle u_{\kappa_f m_{j_f}} \phi_f | V | u_{\kappa_i m_{j_i}} \phi_i \rangle &= \sum_{J \Pi M_J} C^{J M_J}_{j_f m_{j_f} j_{tf} m_{j_{tf}}} C^{J M_J}_{j_i m_{j_i} j_{ti} m_{j_{ti}}} \\
\times \langle (u_{\kappa_f m_{j_f}} \phi_f) : \Pi J M_J | \quad V \quad & | (u_{\kappa_i m_{j_i}} \phi_i) : \Pi J M_J \rangle.
\end{aligned}
\tag{B.4}
$$

with a corresponding expression for the T matrix elements. The variable j_t represents the angular momentum of the target state.

Substituting Eq.(B.4) into Eq.(B.3) the partial wave expansion of the V matrix element becomes

$$
\begin{aligned}
\langle \boldsymbol{k}_f^{(-)} \mu_f + \phi_f | V | \boldsymbol{k}_i^{(+)} \mu_i + \phi_i \rangle &= \frac{2}{\pi} \frac{1}{k_i k_f} \sqrt{\frac{\epsilon_f + c^2}{2\epsilon_f}} \sqrt{\frac{\epsilon_i + c^2}{2\epsilon_i}} \\
&\times \sum_{\kappa_f m_{j_f} \kappa_i m_{j_i} J \Pi M_J} \Bigg[\left(\mathrm{e}^{-\mathrm{i}(\delta_{\kappa_f}+\sigma_{\kappa_f})} \right)^* \mathrm{e}^{\mathrm{i}(\delta_{\kappa_i}+\sigma_{\kappa_i})} \\
&\times (-\mathrm{i})^{l_f} \mathrm{i}^{l_i} C^{j_f m_{j_f}}_{l_f m_{l_f} \frac{1}{2} \mu_f} C^{j_i m_{j_i}}_{l_i m_{l_i} \frac{1}{2} \mu_i} \\
&\times Y_{l_f}^{m_{j_f}-\mu_f}(\hat{\boldsymbol{k}}_f) Y_{l_i}^{*m_{j_i}-\mu_i}(\hat{\boldsymbol{k}}_i) \\
&\times C^{J M_J}_{j_f m_{j_f} j_{tf} m_{j_{tf}}} C^{J M_J}_{j_i m_{j_i} j_{ti} m_{j_{ti}}} \\
&\times \langle (u_{\kappa_f m_{j_f}} \phi_f) : \Pi J M_J | V | (u_{\kappa_i m_{j_i}} \phi_i) : \Pi J M_J \rangle \Bigg].
\end{aligned}
\tag{B.5}
$$

Now substitute Eq.(B.5) and a corresponding expression for T into the three

dimensional Lippmann-Schwinger equation, Eq.(2.36) to obtain

$$
\begin{aligned}
&\sum_{\kappa_f m_{j_f} \kappa_i m_{j_i} J \Pi M_J} \Bigg[\left(\mathrm{e}^{-\mathrm{i}(\delta_{\kappa_f}+\sigma_{\kappa_f})} \right)^* \mathrm{e}^{\mathrm{i}(\delta_{\kappa_i}+\sigma_{\kappa_i})} \\
&\times (-\mathrm{i})^{l_f} \mathrm{i}^{l_i} C^{j_f m_{j_f}}_{l_f m_{l_f} \frac{1}{2} \mu_f} C^{j_i m_{j_i}}_{l_i m_{l_i} \frac{1}{2} \mu_i} Y^{m_{j_f}-\mu_f}_{l_f}(\hat{\boldsymbol{k}}_f) Y^{*m_{j_i}-\mu_i}_{l_i}(\hat{\boldsymbol{k}}_i) \\
&\times C^{JM_J}_{j_f m_{j_f} j_{tf} m_{j_{tf}}} C^{JM_J}_{j_i m_{j_i} j_{ti} m_{j_{ti}}} \langle (u_{\kappa_f m_{j_f}} \phi_f) : \Pi J M_J | T | (u_{\kappa_i m_{j_i}} \phi_i) : \Pi J M_J \rangle \Bigg] \\
&\times \frac{2}{\pi} \sqrt{\frac{\epsilon_f + c^2}{2\epsilon_f}} \sqrt{\frac{\epsilon_i + c^2}{2\epsilon_i}} \\
&= \sum_{\kappa_f m_{j_f} \kappa_i m_{j_i} J \Pi M_J} \Bigg[\left(\mathrm{e}^{-\mathrm{i}(\delta_{\kappa_f}+\sigma_{\kappa_f})} \right)^* \mathrm{e}^{\mathrm{i}(\delta_{\kappa_i}+\sigma_{\kappa_i})} (-\mathrm{i})^{l_f} \mathrm{i}^{l_i} C^{j_f m_{j_f}}_{l_f m_{l_f} \frac{1}{2} \mu_f} C^{j_i m_{j_i}}_{l_i m_{l_i} \frac{1}{2} \mu_i} \\
&\times Y^{m_{j_f}-\mu_f}_{l_f}(\hat{\boldsymbol{k}}_f) Y^{*m_{j_i}-\mu_i}_{l_i}(\hat{\boldsymbol{k}}_i) \\
&\times C^{JM_J}_{j_f m_{j_f} j_{tf} m_{j_{tf}}} C^{JM_J}_{j_i m_{j_i} j_{ti} m_{j_{ti}}} \langle (u_{\kappa_f m_{j_f}} \phi_f) : \Pi J M_J | V | (u_{\kappa_i m_{j_i}} \phi_i) : \Pi J M_J \rangle \Bigg] \\
&\times \frac{2}{\pi} \frac{1}{k_i k_f} \sqrt{\frac{\epsilon_f + c^2}{2\epsilon_f}} \sqrt{\frac{\epsilon_i + c^2}{2\epsilon_i}} \\
&+ \sum_{\kappa_{n'} m_{j_{n'}}} \sum\!\!\!\!\!\!\int_{\boldsymbol{k}',\mu'} k'^2 \mathrm{d}k' \mathrm{d}\Omega_{\boldsymbol{k}'} \sum_{\kappa_f m_{j_f} \kappa' m_{j'} J M_J} \Bigg[\mathrm{e}^{-\mathrm{i}\delta_{\kappa_f}} \mathrm{e}^{+\mathrm{i}\delta_{\kappa'}} (-\mathrm{i})^{l_f} \mathrm{i}^{l'} C^{j_f m_{j_f}}_{l_f m_{l_f} \frac{1}{2} \mu_f} C^{j' m_{j'}}_{l' m_{l'} \frac{1}{2} \mu'} \\
&\times Y^{m_{j_f}-\mu_f}_{l_f}(\hat{\boldsymbol{k}}_f) Y^{*m_{j'}-\mu'}_{l'}(\hat{\boldsymbol{k}}') \\
&\times C^{JM_J}_{j_f m_{j_f} j_{tf} m_{j_{tf}}} C^{JM_J}_{j' m_{j'} j_n m_{j_n}} \langle (u_{\kappa_f m_{j_f}} \phi_f) : \Pi J M_J | V | (u_{\kappa' m_{j'}} \phi_{n'}) : \Pi J M_J \rangle \Bigg] \\
&\times \frac{2}{\pi} \frac{1}{k_i k'} \sqrt{\frac{\epsilon_f + c^2}{2\epsilon_f}} \sqrt{\frac{\epsilon' + c^2}{2\epsilon'}} \\
&\times \frac{1}{E - \epsilon^N_{n'} - \epsilon_{k'} + \mathrm{i}0} \\
&\times \sum_{\kappa' m_{j'} \kappa_i m_{j_i} J' L' M'_J} \Bigg[\mathrm{e}^{-\mathrm{i}\delta_{\kappa'}} \mathrm{e}^{+\mathrm{i}\delta_{\kappa_i}} (-\mathrm{i})^{l'} \mathrm{i}^{l_i} C^{j' m_{j'}}_{l' m_{l'} \frac{1}{2} \mu'} C^{j_i m_{j_i}}_{l_i m_{l_i} \frac{1}{2} \mu_i} \\
&\times Y^{m_{j'}-\mu'}_{l'}(\hat{\boldsymbol{k}}') Y^{*m_{j_i}-\mu_i}_{l_i}(\hat{\boldsymbol{k}}_i) \\
&\times C^{J', M_{J'}}_{j' m_{j'} j_{tn} m_{j_{tn}}} C^{J', M_{J'}}_{j_i m_{j_i} j_{ti} m_{j_{ti}}} \langle (u_{\kappa' m_{j'}} \phi_{n'}) : \Pi' J' M_{J'} | T | (u_{\kappa_i m_{j_i}} \phi_i) : \Pi' J' M_{J'} \rangle \Bigg] \\
&\times \frac{2}{\pi} \frac{1}{k' k_f} \sqrt{\frac{\epsilon' + c^2}{2\epsilon'}} \sqrt{\frac{\epsilon_i + c^2}{2\epsilon_i}}. \qquad \text{(B.6)}
\end{aligned}
$$

Note $m_{l'} = m_{j'} - \mu'$ and $m_{l'} = m_{j'} - \mu'$, therefore using the three relations

$$\int Y_{l'}^{m_{j'}-\mu'}(\hat{\boldsymbol{k}}')Y_{l'}^{m_{j'}-\mu'}(\hat{\boldsymbol{k}}')\mathrm{d}\Omega_{\boldsymbol{k}'} = \delta_{l'l'}\delta_{m_{j'}m_{j'}}, \tag{B.7}$$

$$\sum_{\mu'} C^{j'm_{j'}}_{l'(m'_j-\mu')\frac{1}{2}\mu} C^{j'm_{j'}}_{l'(m_{j'}-\mu')\frac{1}{2}\mu'} = \delta_{j'j'}\delta_{m_{j'}m_{j'}}, \tag{B.8}$$

and

$$\sum_{m_{j'}m_{j_{n'}}} C^{Jm_J}_{j'm_{j'}j_{n'}m_{j_{n'}}} C^{J'm_{J'}}_{j'm_{j'}j_{n'}m_{j_{n'}}} = \delta_{JJ'}\delta_{m_Jm_{J'}}, \tag{B.9}$$

we have

$$\begin{aligned}
&\sum_{\kappa_f m_{j_f}\kappa_i m_{j_i} J\Pi M_J}\Bigg[\left(\mathrm{e}^{-\mathrm{i}(\delta_{\kappa_f}+\sigma_{\kappa_f})}\right)^*\mathrm{e}^{\mathrm{i}(\delta_{\kappa_i}+\sigma_{\kappa_i})}(-\mathrm{i})^{l_f}\mathrm{i}^{l_i}C^{j_fm_{j_f}}_{l_fm_{l_f}\frac{1}{2}\mu_f}C^{j_im_{j_i}}_{l_im_{l_i}\frac{1}{2}\mu_i}\\
\times\;& Y_{l_f}^{m_{j_f}-\mu_f}(\hat{\boldsymbol{k}}_f)Y_{l_i}^{*m_{j_i}-\mu_i}(\hat{\boldsymbol{k}}_i)C^{JM_J}_{j_fm_{j_f}j_{tf}m_{j_{tf}}}C^{JM_J}_{j_im_{j_i}j_{ti}m_{j_{ti}}}\\
\times\;& \langle(u_{\kappa_f m_{j_f}}\phi_f):\Pi JM_J|T|(u_{\kappa_i m_{j_i}}\phi_i):\Pi JM_J\rangle\Bigg]\frac{2}{\pi}\frac{1}{k_ik_f}\sqrt{\frac{\epsilon_f+c^2}{2\epsilon_f}}\sqrt{\frac{\epsilon_i+c^2}{2\epsilon_i}}\\
=\;&\sum_{\kappa_f m_{j_f}\kappa_i m_{j_i} J\Pi M_J}\Bigg[\left(\mathrm{e}^{-\mathrm{i}(\delta_{\kappa_f}+\sigma_{\kappa_f})}\right)^*\mathrm{e}^{\mathrm{i}(\delta_{\kappa_i}+\sigma_{\kappa_i})}(-\mathrm{i})^{l_f}\mathrm{i}^{l_i}C^{j_fm_{j_f}}_{l_fm_{l_f}\frac{1}{2}\mu_f}C^{j_im_{j_i}}_{l_im_{l_i}\frac{1}{2}\mu_i}\\
\times\;& Y_{l_f}^{m_{j_f}-\mu_f}(\hat{\boldsymbol{k}}_f)Y_{l_i}^{*m_{j_i}-\mu_i}(\hat{\boldsymbol{k}}_i)C^{JM_J}_{j_fm_{j_f}j_{tf}m_{j_{tf}}}C^{JM_J}_{j_im_{j_i}j_{ti}m_{j_{ti}}}\\
\times\;& \langle(u_{\kappa_f m_{j_f}}\phi_f):\Pi JM_J|V|(u_{\kappa_i m_{j_i}}\phi_i):\Pi JM_J\rangle\Bigg]\frac{2}{\pi}\frac{1}{k_ik_f}\sqrt{\frac{\epsilon_f+c^2}{2\epsilon_f}}\sqrt{\frac{\epsilon_i+c^2}{2\epsilon_i}}\\
+\;&\sum_{\kappa_{n'}}\sum\!\!\!\!\!\!\int_{\boldsymbol{k}'}\mathrm{d}k'\sum_{\kappa_f m_{j_f}\kappa_i m_{j_i} J\Pi M_J}\Bigg[\left(\mathrm{e}^{-\mathrm{i}(\delta_{\kappa_f}+\sigma_{\kappa_f})}\right)^*\mathrm{e}^{\mathrm{i}(\delta_{\kappa_i}+\sigma_{\kappa_i})}(-\mathrm{i})^{l_f}\mathrm{i}^{l_i}C^{j_fm_{j_f}}_{l_fm_{l_f}\frac{1}{2}\mu_f}C^{j_im_{j_i}}_{l_im_{l_i}\frac{1}{2}\mu_i}\\
\times\;& Y_{l_f}^{m_{j_f}-\mu_f}(\hat{\boldsymbol{k}}_f)Y_{l_i}^{*m_{j_i}-\mu_i}(\hat{\boldsymbol{k}}_i)C^{JM_J}_{j_fm_{j_f}j_{tf}m_{j_{tf}}}C^{JM_J}_{j_im_{j_i}j_{ti}m_{j_{ti}}}\\
\times\;& \frac{2}{\pi}\frac{1}{k_ik_f}\sqrt{\frac{\epsilon_f+c^2}{2\epsilon_f}}\sqrt{\frac{\epsilon'+c^2}{2\epsilon'}}\frac{2}{\pi}\sqrt{\frac{\epsilon'+c^2}{2\epsilon'}}\sqrt{\frac{\epsilon_i+c^2}{2\epsilon_i}}\\
\times\;& \langle(u_{\kappa_f m_{j_f}}\phi_f):\Pi JM_J|V|(u_{\kappa' m_{j'}}\phi_{n'}):\Pi JM_J\rangle\\
\times\;& \frac{1}{E-\epsilon^N_{n'}-\epsilon_{k'}+\mathrm{i}0}\\
\times\;& \langle(u_{\kappa'' m_{j''}}\phi_{n'}):\Pi JM_{J'}|T|(u_{\kappa_i m_{j_i}}\phi_i):\Pi JM_{J'}\rangle\Bigg].
\end{aligned} \tag{B.10}$$

Equating the coefficients of

$$C^{j_f m_{j_f}}_{l_f m_{l_f} \frac{1}{2}\mu_f} C^{j_i m_{j_i}}_{l_i m_{l_i} \frac{1}{2}\mu_i} Y_{l_f}^{m_{j_f}-\mu_f}(\hat{\boldsymbol{k}}_f) Y_{l_i}^{*m_{j_i}-\mu_i}(\hat{\boldsymbol{k}}_i) C^{JM_J}_{j_f m_{j_f} j_{tf} m_{j_{tf}}} C^{JM_J}_{j_i m_{j_i} j_{ti} m_{j_{ti}}} \tag{B.11}$$

for each term in the sum, we have a set of Lippmann-Schwinger equations for each symmetry (ΠJ)

$$\begin{aligned}
& (-\mathrm{i})^{l_f}\mathrm{i}^{l_i}\left(\mathrm{e}^{-\mathrm{i}(\delta_{\kappa_f}+\sigma_{\kappa_f})}\right)^* \mathrm{e}^{\mathrm{i}(\delta_{\kappa_i}+\sigma_{\kappa_i})} \\
\times\ & \langle (u_{\kappa_f m_{j_f}}\phi_f) : \Pi J M_J | T | (u_{\kappa_i m_{j_i}}\phi_i) : \Pi J M_J \rangle \\
\times\ & \frac{2}{\pi}\frac{1}{k_i k_f}\sqrt{\frac{\epsilon_f + c^2}{2\epsilon_f}}\sqrt{\frac{\epsilon_i + c^2}{2\epsilon_i}} \\
=\ & (-\mathrm{i})^{l_f}\mathrm{i}^{l_i}\left(\mathrm{e}^{-\mathrm{i}(\delta_{\kappa_f}+\sigma_{\kappa_f})}\right)^* \mathrm{e}^{\mathrm{i}(\delta_{\kappa_i}+\sigma_{\kappa_i})} \\
\times\ & \langle (u_{\kappa_f m_{j_f}}\phi_f) : \Pi J M_J | V | (u_{\kappa_i m_{j_i}}\phi_i) : \Pi J M_J \rangle \\
\times\ & \frac{2}{\pi}\frac{1}{k_i k_f}\sqrt{\frac{\epsilon_f + c^2}{2\epsilon_f}}\sqrt{\frac{\epsilon_i + c^2}{2\epsilon_i}} \\
+\ & (-\mathrm{i})^{l_f}\mathrm{i}^{l_i}\left(\mathrm{e}^{-\mathrm{i}(\delta_{\kappa_f}+\sigma_{\kappa_f})}\right)^* \mathrm{e}^{\mathrm{i}(\delta_{\kappa_i}+\sigma_{\kappa_i})} \sum_{\kappa_{n'}} \int\!\!\!\!\!\!\int_{\boldsymbol{k}'} \mathrm{d}k' \\
\times\ & \frac{2}{\pi}\frac{1}{k_i k_f}\sqrt{\frac{\epsilon_f + c^2}{2\epsilon_f}}\sqrt{\frac{\epsilon' + c^2}{2\epsilon'}}\frac{2}{\pi}\sqrt{\frac{\epsilon' + c^2}{2\epsilon'}}\sqrt{\frac{\epsilon_i + c^2}{2\epsilon_i}} \\
\times\ & \langle (u_{\kappa_f m_{j_f}}\phi_f) : \Pi J M_J | V | (u_{\kappa_{n'} m_{j_{n'}}}\phi_{n'}) : \Pi J M_J \rangle \\
\times\ & \frac{1}{E - \epsilon^N_{n'} - \epsilon_{k'} + \mathrm{i}0} \\
\times\ & \langle (u_{\kappa_{n'} m_{j_{n'}}}\phi_{n'}) : \Pi J M_{J'} | T | (u_{\kappa_i m_{j_i}}\phi_i) : \Pi J M_{J'} \rangle .
\end{aligned} \tag{B.12}$$

The complex phase factors

$$(-\mathrm{i})^{l_f}\mathrm{i}^{l_i}\left(\mathrm{e}^{-\mathrm{i}(\delta_{\kappa_f}+\sigma_{\kappa_f})}\right)^* \mathrm{e}^{\mathrm{i}(\delta_{\kappa_i}+\sigma_{\kappa_i})} \tag{B.13}$$

cancel on both sides of the equation and we are left with

$$\begin{aligned}
& \langle (u_{\kappa_f m_{j_f}}\phi_f) : \Pi J | T | (u_{\kappa_i m_{j_i}}\phi_i) : \Pi J \rangle \\
\times\ & \frac{2}{\pi}\frac{1}{k_i k_f}\sqrt{\frac{\epsilon_f + c^2}{2\epsilon_f}}\sqrt{\frac{\epsilon_i + c^2}{2\epsilon_i}} \\
=\ & \langle (u_{\kappa_f m_{j_f}}\phi_f) : \Pi J | V | (u_{\kappa_i m_{j_i}}\phi_i) : \Pi J \rangle
\end{aligned}$$

$$
\begin{aligned}
\times \quad & \frac{2}{\pi}\frac{1}{k_i k_f}\sqrt{\frac{\epsilon_f + c^2}{2\epsilon_f}}\sqrt{\frac{\epsilon_i + c^2}{2\epsilon_i}}. \\
+ \quad & \sum_{\kappa_{n'}}\sum\!\!\!\!\!\!\int_{\boldsymbol{k}'} \mathrm{d}k' \\
\times \quad & \frac{2}{\pi}\frac{1}{k_i k_f}\sqrt{\frac{\epsilon_f + c^2}{2\epsilon_f}}\sqrt{\frac{\epsilon' + c^2}{2\epsilon'}}\frac{2}{\pi}\sqrt{\frac{\epsilon' + c^2}{2\epsilon'}}\sqrt{\frac{\epsilon_i + c^2}{2\epsilon_i}} \\
\times \quad & \langle (u_{\kappa_f m_{j_f}}\phi_f) : \Pi J | V | (u_{\kappa_{n'} m_{j_{n'}}}\phi_{n'}) : \Pi J \rangle \\
\times \quad & \frac{1}{E - \epsilon^N_{n'} - \epsilon_{k'} + \mathrm{i}0} \\
\times \quad & \langle (u_{\kappa_{n'} m_{j_{n'}}}\phi_{n'}) : \Pi J | T | (u_{\kappa_i m_{j_i}}\phi_i) : \Pi J \rangle.
\end{aligned}
\tag{B.14}
$$

The quantum number M_J has been dropped from the above equation because the spherical symmetry of the scattering system ensures that the matrix elements are independent of the value of M_J.

Defining

$$
\begin{aligned}
T^{\Pi J}_{fi}(k_f\kappa_f, k_i\kappa_i) \quad = \quad & \langle (u_{\kappa_f m_{j_f}}\phi_f) : \Pi J | T | (u_{\kappa_i m_{j_i}}\phi_i) : \Pi J \rangle \\
\times \quad & \frac{2}{\pi}\frac{1}{k_i k_f}\sqrt{\frac{\epsilon_f + c^2}{2\epsilon_f}}\sqrt{\frac{\epsilon_i + c^2}{2\epsilon_i}},
\end{aligned}
\tag{B.15}
$$

and similarly for the V matrix element, we can write Eq. (B.14) in compact notation

$$
\begin{aligned}
T^{++}_{J\Pi}(k_f^{(-)}, k_i^{(+)})_{fi} \quad = \quad & V^{++}_{J\Pi}(k_f^{(-)}, k_i^{(+)})_{fi} \\
& + \sum_{n'}\sum\!\!\!\!\!\!\int_{k'} \mathrm{d}k' \frac{V^{++}_{J\Pi}(k_f^{(-)}, k'^{(-)})_{fn'} T^{++}_{J\Pi}(k'^{(-)}, k_i^{(+)})_{n'i}}{E - \epsilon^N_{n'} - \epsilon_{k'} + \mathrm{i}0}.
\end{aligned}
\tag{B.16}
$$

Appendix C

The S matrix, T matrix and Cross Section

It is important to note that the relativistic cross section differs from the non-relativistic cross section by a kinematical factor,

$$\left(\frac{\epsilon_{k_i}\epsilon_{k_f}}{m^2c^4}\right). \tag{C.1}$$

This appendix outlines the necessary steps required to derive expressions for the cross section in terms of the T matrix in both the non-relativistic and relativistic cases.

The interaction or collision process may be described by an operator, called the scattering operator or S matrix [152],

$$\Psi^{\text{out}} = S\Psi^{\text{in}}, \tag{C.2}$$

where Ψ^{in} and Ψ^{out} are the incoming and outgoing states. The S matrix is unitary, $S^\dagger S = 1$. Transition probabilities and cross sections can be obtained from the S matrix as follows:

Let the initial state be a free state $|i\rangle$ which is an eigenstate of a maximal set of observables (energy, momentum, spin etc). Now expand the out state into which $|i\rangle$ is transformed as a superposition of the members belonging to the specifying maximal set

$$|\Psi^{\text{out}}\rangle = \sum_n c_n|n\rangle. \tag{C.3}$$

The transition amplitude from $|i\rangle$ to some other specified $|f\rangle$ is given by

$$\begin{aligned} c_f &= \langle f|\Psi^{\text{out}}\rangle \\ &= \langle f|S|\Psi^{\text{in}}\rangle \\ &= \langle f|S|i\rangle \\ &= S_{fi}. \end{aligned} \tag{C.4}$$

The T matrix is introduced with the following rationale:

1. From S the unit operator is extracted to leave the part corresponding to transitions between different states.

2. Energy conservation is guaranteed between infinitely removed (in time or space) initial and final states, therefore an energy conserving factor $\delta(E_i - E_f)$ is introduced into the remaining part.

Thus we have

$$S_{fi} = \delta_{fi} - 2\pi\mathrm{i}\delta(E_i - E_f)T_{fi}, \tag{C.5}$$

where $T_{fi} = \langle f|T|i\rangle$ is the transition matrix (or "T matrix"), and the factor $2\pi\mathrm{i}$ has been introduced for convenience. The transition per unit time from a state $i \to f$ is

$$w_{i\to f} = \frac{|c_f|^2}{\tau} = \frac{|S_{fi}|^2}{\tau}. \tag{C.6}$$

Using the integral representation of the δ function

$$\delta(E_i - E_f) = \frac{1}{2\pi}\int_{-\infty}^{\infty} \mathrm{d}t\mathrm{e}^{\mathrm{i}(E_i - E_f)t/\hbar}, \tag{C.7}$$

we can write for $i \neq f$

$$S_{fi} = \lim_{\tau\to\infty} -T_{fi}\frac{\mathrm{i}}{\hbar}\int_{-\tau/2}^{\tau/2} \mathrm{d}t\mathrm{e}^{\mathrm{i}(E_i - E_f)t/\hbar}. \tag{C.8}$$

Thus we have

$$\begin{aligned} w_{i\to f} &= \frac{|S_{fi}|^2}{\tau} \\ &= \lim_{\tau\to\infty}\frac{|T_{fi}|^2}{\tau}\left|\frac{\mathrm{i}}{\hbar}\int_{-\tau/2}^{\tau/2} dt\mathrm{e}^{i(E_i - E_f)t/\hbar}\right|^2 \end{aligned}$$

$$\begin{aligned}
&= \lim_{\tau\to\infty} \frac{|T_{fi}|^2}{\tau} \left| \frac{\mathrm{i}}{\hbar} \left[\frac{\mathrm{e}^{i(E_i-E_f)t/\hbar}}{i(E_i-E_f)/\hbar} \right]_{\tau/2}^{\tau/2} \right|^2 \\
&= \lim_{\tau\to\infty} \frac{|T_{fi}|^2}{\tau} \left| \frac{2\sin((E_i-E_f)\tau/(2\hbar))}{(E_i-E_f)} \right|^2 \\
&= \lim_{\tau\to\infty} \frac{|T_{fi}|^2}{\tau} \frac{4\sin^2((E_i-E_f)\tau/(2\hbar))}{(E_i-E_f)^2} \\
&= \lim_{\tau\to\infty} |T_{fi}|^2 \frac{4\sin^2(\frac{\tau}{2\hbar}(E_i-E_f))}{\frac{\tau}{2\hbar}(E_i-E_f)^2} \frac{1}{2\hbar}.
\end{aligned} \tag{C.9}$$

Now we use the identity

$$\delta(x) = \frac{1}{\pi} \lim_{\alpha\to\infty} \frac{\sin^2(\alpha x)}{\alpha x^2}, \tag{C.10}$$

to obtain

$$w_{i\to f} = \frac{2\pi}{\hbar} \delta(E_i - E_f) |T_{fi}|^2 \quad , f \neq i. \tag{C.11}$$

We need the transition into a group of states centred at $E = E_f$. If the density of states f in the neighborhood of the energy E_f is denoted $\rho(E)$, then the transition probability into the group is

$$\begin{aligned}
w_{i\to f}^{\text{group}} &= \frac{2\pi}{\hbar} \int_{E_f - \mathrm{d}E/2}^{E_f + \mathrm{d}E/2} \delta(E_i - E_f) |T_{fi}|^2 \rho(E) \mathrm{d}E \\
&= \frac{2\pi}{\hbar} |T_{fi}|^2 \rho(E).
\end{aligned} \tag{C.12}$$

This takes the same form as the Golden rule derived from time dependent perturbation theory. However, unlike the Golden rule, which is an approximation, the above result is exact when the Lippmann-Schwinger equation is used to solve for the T matrix,

$$T = V + VGT. \tag{C.13}$$

C.1 Non-relativistic cross section

The probability per unit time for a transition from an initial state i to a final state f such that the momentum of the scattered particle lies in the

range $\boldsymbol{p}_f$ to $\boldsymbol{p}_f + d\boldsymbol{p}$ is

$$w_{fi} = \sum_f \frac{2\pi}{\hbar} |\langle f|T|i\rangle|^2 \delta(E_f - E_i)\rho_f, \tag{C.14}$$

where E_i and E_f represent the initial and final state of the whole system. The density of final states is obtained by first considering box normalized states: with $k_x = \frac{2\pi}{L} n_x$, and similarly for y and z, the number of final states between $\boldsymbol{k_f}$ and $\boldsymbol{k_f} + d\boldsymbol{k_f}$ is

$$\begin{aligned} \rho_f &= n^2 \mathrm{d}n\mathrm{d}\Omega \\ &= \frac{L^2 k_f^2}{(2\pi)^2} \frac{L}{2\pi} \mathrm{d}k_f \mathrm{d}\Omega. \end{aligned} \tag{C.15}$$

Now $\epsilon_f = \frac{\hbar^2 k_f^2}{2m}$ and therefore $\mathrm{d}\epsilon_f = \frac{\hbar^2 k_f}{m} dk_f$, so

$$\mathrm{d}k_f = \frac{m\mathrm{d}\epsilon_f}{\hbar^2 k_f}. \tag{C.16}$$

Thus the density of final states is

$$\rho_f = \frac{L^2 k_f^2}{(2\pi)^2} \frac{L}{2\pi} \frac{m\mathrm{d}\epsilon_f}{\hbar^2 k_f} \mathrm{d}\Omega. \tag{C.17}$$

The differential cross section is obtained by dividing the w_{fi} by the incident particle flux=velocity/volume= v/L^3, therefore

$$\begin{aligned} \mathrm{d}\sigma &= w_{fi}/(v/L^3) \\ &= \frac{1}{v/L^3} \sum_f \frac{2\pi}{\hbar} |\langle f|T|i\rangle|^2 \delta(E_f - E_i) \\ &\quad \times \frac{L^2 k_f^2}{(2\pi)^2} \frac{L}{2\pi} \frac{m\mathrm{d}\epsilon_f}{\hbar^2 k} \mathrm{d}\Omega. \end{aligned} \tag{C.18}$$

The sum over final states becomes an integral because they are continuous, and the delta function reduces the integration to one term,

$$\begin{aligned} \mathrm{d}\sigma &= \frac{1}{v/L^3} \int \frac{2\pi}{\hbar} |\langle f|T|i\rangle|^2 \delta(E_f - E_i) \\ &\quad \times \frac{L^2 k_f^2}{(2\pi)^2} \frac{L}{2\pi} \frac{m\mathrm{d}\epsilon_f}{\hbar^2 k_f} \mathrm{d}\Omega \end{aligned}$$

$$= \frac{1}{v/L^3}\frac{2\pi}{\hbar}|\langle f|T|i\rangle|^2\frac{L^2k_f^2}{(2\pi)^2}\frac{L}{2\pi}\frac{m}{\hbar^2k_f}\mathrm{d}\Omega. \tag{C.19}$$

The non-relativistic expression for the incident projectile velocity is

$$v = p_i/m = \hbar k_i/m, \tag{C.20}$$

thus we have

$$\begin{aligned}\frac{\mathrm{d}\sigma}{d\Omega} &= \frac{L^3m}{\hbar k_i}\frac{2\pi}{\hbar}|\langle f|T|i\rangle|^2\frac{L^2k_f^2}{(2\pi)^2}\frac{L}{2\pi}\frac{m}{\hbar^2k_f} \\ &= \frac{k_f}{k_i}L^6\left|\frac{m}{2\pi\hbar^2}\langle f|T|i\rangle\right|^2. \end{aligned}\tag{C.21}$$

Note, for delta function normalization of continuum waves the L^3 is replaced by $(2\pi)^3$ and we obtain

$$\frac{d\sigma}{d\Omega} = \tfrac{k_f}{k_i}\left|\tfrac{(2\pi)^2m}{\hbar^2}\langle f|T|i\rangle\right|^2. \tag{C.22}$$

It is convenient to introduce a scattering amplitude, f_{fi}, which is defined by

$$\frac{d\sigma}{d\Omega} = \tfrac{k_f}{k_i}\left|f_{fi}\right|^2. \tag{C.23}$$

Therefore,

$$\left|f_{fi}\right|^2 = \left|\tfrac{(2\pi)^2m}{\hbar^2}\langle f|T|i\rangle\right|^2. \tag{C.24}$$

f_{fi} is defined up to a phase, which is chosen to agree with the derivation of potential scattering,

$$f_{fi} = -\tfrac{(2\pi)^2m}{\hbar^2}\langle f|T|i\rangle. \tag{C.25}$$

C.2 Relativistic cross section

The derivation of the expression for the relativistic cross section proceeds as per the non-relativistic case, however the velocity of the incident projectile is determined from the relativistic energy-momentum relation

$$\epsilon_k = \frac{mc^2}{\sqrt{1-v^2/c^2}},$$

$$\begin{aligned}
\Rightarrow 1 - v^2/c^2 &= m^2c^4/\epsilon_k^2 \\
\Rightarrow v &= c\sqrt{1 - m^2c^4/\epsilon_k^2} \\
\Rightarrow v &= c^2 p/\epsilon_k \\
\Rightarrow v &= c^2\hbar k/\epsilon_k. \qquad \text{(C.26)}
\end{aligned}$$

Now

$$\begin{aligned}
\epsilon_k^2 &= p^2c^2 + m^2c^4 \\
\Rightarrow \epsilon_k &= \sqrt{p^2c^2 + m^2c^4} \\
\Rightarrow \mathrm{d}\epsilon_k &= 1/2(p^2c^2 + m^2c^4)^{-1/2} 2pc^2 \mathrm{d}p \\
\Rightarrow \mathrm{d}\epsilon_k &= \frac{c^2 p}{\epsilon_k}\mathrm{d}p \\
\Rightarrow \mathrm{d}p &= \frac{\epsilon_k \mathrm{d}\epsilon_k}{c^2 p} \\
\Rightarrow \mathrm{d}k &= \frac{\epsilon_k \mathrm{d}\epsilon_k}{\hbar^2 c^2 k}. \qquad \text{(C.27)}
\end{aligned}$$

Proceeding as in the non-relativistic case

$$w_{fi} = \sum_f \frac{2\pi}{\hbar}|\langle f|T|i\rangle|^2 \delta(E_f - E_i)\rho_f, \qquad \text{(C.28)}$$

where

$$\begin{aligned}
\rho_f &= n^2 \mathrm{d}n\mathrm{d}\Omega \\
&= \frac{L^2 k_f^2}{(2\pi)^2}\frac{L}{2\pi}\mathrm{d}k_f \mathrm{d}\Omega \\
&= \frac{L^2 k_f^2}{(2\pi)^2}\frac{L}{2\pi}\frac{\epsilon_{k_f}\mathrm{d}\epsilon_{k_f}}{\hbar^2 c^2 k_f}\mathrm{d}\Omega. \qquad \text{(C.29)}
\end{aligned}$$

The differential cross section is obtained by dividing the w_{fi} by the incident particle flux=velocity/volume= v/L^3, therefore

$$\begin{aligned}
\mathrm{d}\sigma &= w_{fi}/(v/L^3) \\
&= \frac{1}{v/L^3}\sum_f \left(\frac{2\pi}{\hbar}|\langle f|T|i\rangle|^2 \delta(E_f - E_i)\frac{L^2 k_f^2}{(2\pi)^2}\frac{L}{2\pi}\frac{\epsilon_{k_f}\mathrm{d}\epsilon_{k_f}}{\hbar^2 c^2 k_f}\mathrm{d}\Omega\right). \qquad \text{(C.30)}
\end{aligned}$$

The sum over final states becomes an integral because they are continuous, and the delta function reduces the integration to one term,

$$\begin{aligned} \mathrm{d}\sigma &= \frac{1}{v/L^3}\int \frac{2\pi}{\hbar}|\langle f|T|i\rangle|^2\delta(E_f-E_i)\frac{L^2k_f^2}{(2\pi)^2}\frac{L}{2\pi}\frac{\epsilon_{k_f}\mathrm{d}\epsilon_{k_f}}{\hbar^2c^2k_f}\mathrm{d}\Omega \\ &= \frac{1}{v/L^3}\frac{2\pi}{\hbar}|\langle f|T|i\rangle|^2\frac{L^2k_f^2}{(2\pi)^2}\frac{L}{2\pi}\frac{\epsilon_{k_f}}{\hbar^2c^2k_f}\mathrm{d}\Omega. \end{aligned} \tag{C.31}$$

Now we use Eq.(C.26) for the relativistic velocity and we have

$$\begin{aligned} \frac{\mathrm{d}\sigma}{\mathrm{d}\Omega} &= \frac{L^3\epsilon_{k_i}}{c^2\hbar k_i}\frac{2\pi}{\hbar}|\langle f|T|i\rangle|^2\frac{L^2k_f^2}{(2\pi)^2}\frac{L}{2\pi}\frac{\epsilon_{k_f}}{\hbar^2c^2k_f} \\ &= \frac{k_f}{k_i}L^6\left|\frac{m}{2\pi\hbar^2}\langle f|T|i\rangle\right|^2\left(\frac{\epsilon_{k_i}\epsilon_{k_f}}{m^2c^4}\right). \end{aligned} \tag{C.32}$$

Thus the relativistic cross section differs from the non-relativistic cross section Eq.(C.21) by a factor

$$\left(\frac{\epsilon_{k_i}\epsilon_{k_f}}{m^2c^4}\right). \tag{C.33}$$

Usually periodic boundary conditions are employed in which $L^3 = (2\pi)^3$, and therefore in atomic units ($\hbar = m = 1$) Eq. (C.32) becomes

$$\frac{\mathrm{d}\sigma}{\mathrm{d}\Omega} = (2\pi)^4\left(\frac{\epsilon_{k_i}\epsilon_{k_f}}{c^4}\right)\frac{k_f}{k_i}|\langle f|T|i\rangle|^2. \tag{C.34}$$

C.3 Scattering amplitude

For electron scattering on atoms or ions we can write the differential cross section, Eq. (C.32),

$$\frac{\mathrm{d}\sigma}{\mathrm{d}\Omega} = (2\pi)^4\left(\frac{\epsilon_{k_i}\epsilon_{k_f}}{c^4}\right)\frac{k_f}{k_i}\left|\langle \boldsymbol{k}_f^{(-)}\mu_f+\phi_f|T|\boldsymbol{k}_i^{(+)}\mu_i+\phi_i\rangle\right|^2. \tag{C.35}$$

Using Eq.(B.5) for the partial wave expansion of the T matrix element and taking the initial projectile momentum $\boldsymbol{k}_i$ along the $\hat{z}$ direction and thus with $(\theta,\phi) = (0,0)$ so that

$$Y_{l_i}^{m_{l_i}}(\hat{\boldsymbol{k}}_i) = \sqrt{\frac{2l_i+1}{4\pi}}\delta_{m_{l_i},0}, \tag{C.36}$$

we have

$$\begin{aligned}\langle \boldsymbol{k}_f^{(-)}\mu_f+\phi_f|T|\boldsymbol{k}_i^{(+)}\mu_i+\phi_i\rangle &= \frac{2}{\pi}\frac{1}{k_f k_i}\sum_{\kappa_f m_{j_f}\kappa_i m_{j_i} J\Pi M_J}\left(\mathrm{e}^{-\mathrm{i}\eta_{\kappa_f}}\right)^*\mathrm{e}^{\mathrm{i}\eta_{\kappa_i}}(-\mathrm{i})^{l_f}\mathrm{i}^{l_i}\\ &\times \sqrt{\frac{\epsilon_f+c^2}{2\epsilon_f}}\sqrt{\frac{\epsilon_i+c^2}{2\epsilon_i}}\\ &\times C^{j_f m_{j_f}}_{l_f m_{l_f}\frac{1}{2}\mu_f}C^{j_i m_{j_i}}_{l_i m_{l_i}\frac{1}{2}\mu_i}C^{JM_J}_{j_f m_{j_f} j_{t_f} m_{j_{t_f}}}C^{JM_J}_{j_i m_{j_i} j_{t_i} m_{j_{t_i}}}\\ &\times Y_{l_f}^{m_{l_f}}(\hat{\boldsymbol{k}})\sqrt{\frac{2l_i+1}{4\pi}}\delta_{m_{l_i},0}\\ &\times \langle(u_{\kappa_f m_j}\phi_f):J,M_J|T|(u_{\kappa_i m_j}\phi_i):J,M_J\rangle.\end{aligned} \tag{C.37}$$

Using Eq.(B.15) we have

$$\begin{aligned}\langle \boldsymbol{k}_f^{(-)}\mu_f+\phi_f|T|\boldsymbol{k}_i^{(+)}\mu_i+\phi_i\rangle &= \sum_{\kappa_f m_{j_f}\kappa_i m_{j_i} J\Pi M_J}\mathrm{e}^{\mathrm{i}\eta_{\kappa_f}}\mathrm{e}^{\mathrm{i}\eta_{\kappa_i}}(-\mathrm{i})^{l_f}\mathrm{i}^{l_i}\\ &\times C^{j_f m_{j_f}}_{l_f m_{l_f}\frac{1}{2}\mu_f}C^{j_i m_{j_i}}_{l_i 0\frac{1}{2}\mu_i}C^{JM_J}_{j_f m_{j_f} j_{t_f} m_{j_{t_f}}}C^{JM_J}_{j_i m_{j_i} j_{t_i} m_{j_{t_i}}}\\ &\times Y_{l_f}^{m_{l_f}}(\hat{\boldsymbol{k}})\sqrt{\frac{2l_i+1}{4\pi}}T^{\Pi J}_{fi}(k_f\kappa_f,k_i\kappa_i),\end{aligned} \tag{C.38}$$

where J is the total angular momentum of the system, j_i and j_f are the initial and final total angular moment of the projectile respectively, and j_{t_i} and j_{t_f} are the initial and final angular momentum of the target respectively.

For a given initial projectile state with fixed μ_i we have a fixed $m_{j_i}=\mu_i+m_{l_i}$ since $m_{l_i}=0$. We therefore have a fixed value of $M_J=m_{j_i}+m_{j_{t_I}}$ for a given initial target state with fixed $m_{j_{t_i}}$. M_J is a conserved quantum number (the system is spherically symmetric) and therefore for a given final target state with fixed m_{j-t_f} we must also have fixed m_{j_f} for the projectile. Thus for a given initial pair $(\mu_i,m_{j_{t_i}})$ and final pair $(\mu_f,m_{j_{t_f}})$ of quantum numbers we can define the scattering amplitude

$$\begin{aligned}F^{\mu_f\mu_i}_{m_f m_i}(\theta) &= -\langle \boldsymbol{k}_f^{(-)}\mu_f+\phi_f|T|\boldsymbol{k}_i^{(+)}\mu_i+\phi_i\rangle\\ &= -\sum_{\kappa_f m_{j_f}\kappa_i m_{j_i} J\Pi}\mathrm{e}^{\mathrm{i}\eta_{\kappa_f}}\mathrm{e}^{\mathrm{i}\eta_{\kappa_i}}(-\mathrm{i})^{l_f}\mathrm{i}^{l_i}\end{aligned}$$

$$\begin{aligned} &\times \quad C^{j_f m_{j_f}}_{l_f m_{l_f} \frac{1}{2}\mu_f} C^{j_i m_{j_i}}_{l_i 0 \frac{1}{2}\mu_i} C^{JM_J}_{j_f m_{j_f} j_{t_f} m_{j_{t_f}}} C^{JM_J}_{j_i m_{j_i} j_{t_i} m_{j_{t_i}}} \\ &\times \quad Y^{m_{l_f}}_{l_f}(\hat{\boldsymbol{k}}) \sqrt{\frac{2l_i+1}{4\pi}} T^{\Pi J}_{fi}(k_f\kappa_f, k_i\kappa_i), \end{aligned} \tag{C.39}$$

where the minus sign is a convention chosen to agree with the scattering amplitude for potential scattering. Note, there are varying conventions on the factors of proportionality between the the scattering amplitude and the T-matrix. For instance, Bransden [153] defines the scattering amplitude as

$$F = -\left(\frac{1}{2\pi}\right) T, \tag{C.40}$$

and Goldberger and Watson [154] define it as

$$F = -(2\pi)^4 T. \tag{C.41}$$

Appendix D

Integrated Cross Section

D.1 Total cross section and partial wave integrated cross section

With the aid of Eq.(C.32) we have the total cross section for excitation to a particular state

$$\begin{aligned}\sigma_{fi} &= \int \mathrm{d}\Omega_{\boldsymbol{k}} \frac{\mathrm{d}\sigma}{\mathrm{d}\Omega} \\ &= \int \mathrm{d}\Omega_{\boldsymbol{k}} (2\pi)^4 \frac{k_f}{k_i} \frac{\epsilon_f \epsilon_i}{c^4} \left| T_{fi}^{++}(\boldsymbol{k}_f^{(-)} \mu_f, \boldsymbol{k}_i^{(+)} \mu_i) \right|^2 .\end{aligned} \tag{D.1}$$

For the case of unpolarized target atom and electron beams we sum over final states and average over initial states,

$$\begin{aligned}\sigma_{fi} &= \int \mathrm{d}\Omega_{\boldsymbol{k}} (2\pi)^4 \frac{k_f}{k_i} \frac{\epsilon_f \epsilon_i}{c^4} \\ &\times \frac{1}{2(2j_{\mathrm{target}_i}+1)} \sum_{\mu_f \mu_i m_{j_{t_f}} m_{j_{t_i}}} \left| T_{fi}^{++}(\boldsymbol{k}_f^{(-)} \mu_f, \boldsymbol{k}_i^{(+)} \mu_i) \right|^2 .\end{aligned} \tag{D.2}$$

Using Eq.(B.5) for the partial wave expansion of the T matrix element and taking the initial projectile momentum $\boldsymbol{k}_i$ along the $\hat{z}$ direction and thus

with $(\theta, \phi) = (0, 0)$ so that

$$Y_{l_i}^{m_{l_i}}(\hat{\boldsymbol{k}}_i) = \sqrt{\frac{2l_i+1}{4\pi}}\delta_{m_{l_i},0}, \tag{D.3}$$

we have

$$\begin{aligned}
\sigma_{fi} &= \int \mathrm{d}\Omega_{\boldsymbol{k}}(2\pi)^4 \frac{k_f}{k_i}\frac{\epsilon_f\epsilon_i}{c^4}\frac{1}{2(2j_{\mathrm{target}_i}+1)}\sum_{\mu_f\mu_i m_{j_{t_f}} m_{j_{t_i}}}\left|\frac{2}{\pi}\frac{1}{k_f k_i}\right. \\
&\times \sum_{\kappa_f m_{j_f}\kappa_i m_{j_i} J\Pi M_J}\left(\mathrm{e}^{-\mathrm{i}\eta_{\kappa_f}}\right)^* \mathrm{e}^{\mathrm{i}\eta_{\kappa_i}}(-\mathrm{i})^{l_f}\mathrm{i}^{l_i} \\
&\times \sqrt{\frac{\epsilon_f+c^2}{2\epsilon_f}}\sqrt{\frac{\epsilon_i+c^2}{2\epsilon_i}}C^{j_f m_{j_f}}_{l_f m_{l_f}\frac{1}{2}\mu_f}C^{j_i m_{j_i}}_{l_i m_{l_i}\frac{1}{2}\mu_i}C^{JM_J}_{j_f m_{j_f} j_{t_f} m_{j_{t_f}}}C^{JM_J}_{j_i m_{j_i} j_{t_i} m_{j_{t_i}}} \\
&\times Y_{l_f}^{m_{l_f}}(\hat{\boldsymbol{k}})\sqrt{\frac{2l_i+1}{4\pi}}\delta_{m_{l_i},0} \\
&\times \left.\langle(u_{\kappa_f m_j}\phi_f) : J, M_J|T|(u_{\kappa_i m_j}\phi_i) : J, M_J\rangle\right|^2.
\end{aligned} \tag{D.4}$$

Using Eq.(B.15) we have

$$\begin{aligned}
\sigma_{fi} &= \int \mathrm{d}\Omega_{\boldsymbol{k}}(2\pi)^4 \left(\frac{k_f}{k_i}\right)\left(\frac{\epsilon_f\epsilon_i}{c^4}\right)\frac{1}{2(2j_{\mathrm{target}_i}+1)}\sum_{\mu_f\mu_i m_{j_{t_f}} m_{j_{t_i}}} \\
&\times \left(\sum_{\kappa_f m_{j_f}\kappa_i m_{j_i} J\Pi M_J}\left(\mathrm{e}^{-\mathrm{i}\eta_{\kappa_f}}\right)^* \mathrm{e}^{\mathrm{i}\eta_{\kappa_i}}(-\mathrm{i})^{l_f}\mathrm{i}^{l_i}\right. \\
&\times C^{j_f m_{j_f}}_{l_f m_{l_f}\frac{1}{2}\mu_f}C^{j_i m_{j_i}}_{l_i m_{l_i}\frac{1}{2}\mu_i}C^{JM_J}_{j_f m_{j_f} j_{t_f} m_{j_{t_f}}}C^{JM_J}_{j_i m_{j_i} j_{t_i} m_{j_{t_i}}} \\
&\times \left. Y_{l_f}^{m_{l_f}}(\hat{\boldsymbol{k}})\sqrt{\frac{2l_i+1}{4\pi}}\delta_{m_{l_i},0}T^{\Pi J}_{fi}(k_f\kappa_f, k_i\kappa_i)\right) \\
&\times \left(\sum_{\kappa'_f m'_{j_f}\kappa'_i m'_{j_i} J'\Pi' M'_J}\left(\mathrm{e}^{-\mathrm{i}\eta_{\kappa'_f}}\right)^* \mathrm{e}^{\mathrm{i}\eta_{\kappa'_i}}(-\mathrm{i})^{l'_f}\mathrm{i}^{l'_i}\right. \\
&\times C^{j'_f m'_{j_f}}_{l'_f m'_{l_f}\frac{1}{2}\mu_f}C^{j'_i m'_{j_i}}_{l'_i m'_{l_i}\frac{1}{2}\mu_i}C^{J'M'_J}_{j'_f m'_{j_f} j_{t_f} m_{j_{t_f}}}C^{J'M'_J}_{j'_i m'_{j_i} j_{t_i} m_{j_{t_i}}} \\
&\times \left. Y_{l'_f}^{m'_{l_f}}(\hat{\boldsymbol{k}})\sqrt{\frac{2l'_i+1}{4\pi}}\delta_{m'_{l_i},0}T^{\Pi' J'}_{fi}(k_f\kappa'_f, k_i\kappa'_i)\right)^*,
\end{aligned} \tag{D.5}$$

where J is the total angular momentum of the system, j_i and j_f are the initial and final total angular moment of the projectile respectively, and j_{t_i} and j_{t_f} are the initial and final angular momentum of the target respectively. This equation can be simplified with the following equations that produce delta functions to collapse several of the sums

$$\int Y_{l_f}^{m_{l_f}}(\hat{\boldsymbol{k}}) Y_{l'_f}^{m'_{l_f}}(\hat{\boldsymbol{k}}) \mathrm{d}\Omega_{\boldsymbol{k}} = \delta_{l_f,l'_f}\delta_{m_{l_f},m'_{l_f}}, \tag{D.6}$$

and

$$\begin{aligned}
\sum_{m_{j_f}\mu_f} C^{j_f m_{j_f}}_{l_f m_{l_f}\frac{1}{2}\mu_f} C^{j'_f m'_{j_f}}_{l'_f m'_{l_f}\frac{1}{2}\mu_f} &= \sum_{m_{j_f}\mu_f} C^{j_f m_{j_f}}_{l_f m_{l_f}\frac{1}{2}\mu_f} C^{j'_f m'_{j_f}}_{l_f m_{l_f}\frac{1}{2}\mu_f} \\
&= \sum_{m_{j_f}\mu_f} C^{j_f m_{j_f}}_{l_f (m_{j_f}-\mu_f)\frac{1}{2}\mu_f} C^{j'_f m'_{j_f}}_{l_f (m_{j_f}-\mu_f)\frac{1}{2}\mu_f} \\
&= \delta_{j_f j'_f}\delta_{m_{j_f} m'_{j_f}},
\end{aligned} \tag{D.7}$$

which gives

$$\begin{aligned}
\sigma_{fi} &= (2\pi)^4 \left(\frac{k_f}{k_i}\right)\left(\frac{\epsilon_f \epsilon_i}{c^4}\right) \frac{1}{2(2j_{\mathrm{target}_i}+1)} \sum_{\mu_i m_{j_{t_f}} m_{j_{t_i}}} \\
&\times \Bigg(\sum_{\kappa_f m_{j_f} \kappa_i m_{j_i} J\Pi M_J} \mathrm{e}^{\mathrm{i}\eta_{\kappa_i}} \mathrm{i}^{l_i} \\
&\times C^{j_i m_{j_i}}_{l_i m_{l_i}\frac{1}{2}\mu_i} C^{JM_J}_{j_f m_{j_f} j_{t_f} m_{j_{t_f}}} C^{JM_J}_{j_i m_{j_i} j_{t_i} m_{j_{t_i}}} \\
&\times \sqrt{\frac{2l_i+1}{4\pi}} \delta_{m_{l_i},0} T^{\Pi J}_{fi}(k_f\kappa_f, k_i\kappa_i) \Bigg) \\
&\times \Bigg(\sum_{\kappa'_i m'_{j_i} J'\Pi' M'_J} \mathrm{e}^{\mathrm{i}\eta_{\kappa'_i}} \mathrm{i}^{l'_i} \\
&\times C^{j'_i m'_{j_i}}_{l'_i m'_{l_i}\frac{1}{2}\mu_i} C^{J'M'_J}_{j_f m_{j_f} j_{t_f} m_{j_{t_f}}} C^{J'M'_J}_{j'_i m'_{j_i} j_{t_i} m_{j_{t_i}}} \\
&\times \sqrt{\frac{2l'_i+1}{4\pi}} \delta_{m'_{l_i},0} T^{\Pi' J'}_{fi}(k_f\kappa'_f, k_i\kappa'_i) \Bigg)^*.
\end{aligned} \tag{D.8}$$

Now we use

$$\sum_{m_{j_f} m_{j_{t_f}}} C^{JM_J}_{j_f m_{j_f} j_{t_f} m_{j_{t_f}}} C^{J'M'_J}_{j_f m_{j_f} j_{t_f} m_{j_{t_f}}} = \delta_{JJ'}\delta_{M_J M_{J'}}, \tag{D.9}$$

to give

$$\begin{aligned}
\sigma_{fi} &= (2\pi)^4 \left(\frac{k_f}{k_i}\right)\left(\frac{\epsilon_f \epsilon_i}{c^4}\right) \frac{1}{2(2j_{\mathrm{target}_i}+1)} \sum_{\mu_i m_{j_{t_i}}} \\
&\times \Bigg(\sum_{\kappa_f \kappa_i m_{j_i} J \Pi M_J} \mathrm{e}^{\mathrm{i}\eta_{\kappa_i}} \mathrm{i}^{l_i} \\
&\times C^{j_i m_{j_i}}_{l_i m_{l_i} \frac{1}{2}\mu_i} C^{JM_J}_{j_i m_{j_i} j_{t_i} m_{j_{t_i}}} \\
&\times \sqrt{\frac{2l_i+1}{4\pi}} \delta_{m_{l_i},0} T^{\Pi J}_{fi}(k_f\kappa_f, k_i\kappa_i) \Bigg) \\
&\times \Bigg(\sum_{\kappa'_i m'_{j_i}} \mathrm{e}^{\mathrm{i}\eta_{\kappa'_i}} \mathrm{i}^{l'_i} \\
&\times C^{j'_i m'_{j_i}}_{l'_i m'_{l_i} \frac{1}{2}\mu_i} C^{JM_J}_{j'_i m'_{j_i} j_{t_i} m_{j_{t_i}}} \\
&\times \sqrt{\frac{2l'_i+1}{4\pi}} \delta_{m'_{l_i},0} T^{\Pi J}_{fi}(k_f\kappa_f, k_i\kappa'_i) \Bigg)^* .
\end{aligned} \tag{D.10}$$

The angular momentum algebra manipulations listed in Appendix E lead to further simplification. We apply Eq. (E.9) twice,

$$\begin{aligned}
C^{j_i m_{j_i}}_{l_i m_{l_i} \frac{1}{2}\mu_i} C^{JM_J}_{j_i m_{j_i} j_{t_i} m_{j_{t_i}}} &= (-1)^{l_i - m_{l_i}} \sqrt{\frac{2j_i+1}{2l_i+1}} C^{l_i,-m_{l_i}}_{j_i,-m_{j_i}\frac{1}{2}\mu_i} \\
&\times (-1)^{j_i - m_{j_i}} \sqrt{\frac{2J+1}{2j_i+1}} C^{j_i,-m_{j_i}}_{J,-M_J j_{t_i} m_{j_{t_i}}} \\
&= (-1)^{l_i - m_{l_i} + j_i - m_{j_i}} \sqrt{\frac{2J+1}{2l_i+1}} C^{l_i,-m_{l_i}}_{j_i,-m_{j_i}\frac{1}{2}\mu_i} C^{j_i,-m_{j_i}}_{J,-M_J j_{t_i} m_{j_{t_i}}},
\end{aligned} \tag{D.11}$$

and similarly

$$C^{j'_i m'_{j_i}}_{l'_i m'_{l_i} \frac{1}{2}\mu_i} C^{JM_J}_{j'_i m'_{j_i} j_{t_i} m_{j_{t_i}}} = (-1)^{l'_i - m'_{l_i} + j_i - m'_{j_i}} \sqrt{\frac{2J+1}{2l'_i+1}}$$

$$\times \quad C^{l_i',-m_{l_i}'}_{j_i',-m_{j_i}'\,\frac{1}{2}\mu_i} C^{j_i',-m_{j_i}'}_{J,-M_J j_{t_i} m_{j_{t_i}}}. \tag{D.12}$$

We therefore have

$$\begin{aligned}
\sigma_{fi} &= (2\pi)^4 \left(\frac{k_f}{k_i}\right)\left(\frac{\epsilon_f\epsilon_i}{c^4}\right)\frac{1}{2(2j_{\mathrm{target}_i}+1)}\sum_{\mu_i m_{j_{t_i}}}\left(\frac{2J+1}{4\pi}\right)\\
&\times \Bigg(\sum_{\kappa_f\kappa_i m_{j_i} J\Pi M_J} \mathrm{e}^{\mathrm{i}\eta_{\kappa_i}}\mathrm{i}^{l_i}\\
&\times \; C^{l_i,-m_{l_i}}_{j_i,-m_{j_i}\,\frac{1}{2}\mu_i} C^{j_i,-m_{j_i}}_{J,-M_J j_{t_i} m_{j_{t_i}}}\\
&\times \; \delta_{m_{l_i},0} T^{\Pi J}_{fi}(k_f\kappa_f, k_i\kappa_i)\Bigg)\\
&\times \Bigg(\sum_{\kappa_i' m_{j_i}'} \mathrm{e}^{\mathrm{i}\eta_{\kappa_i'}}\mathrm{i}^{l_i'}\\
&\times \; C^{l_i',-m_{l_i}'}_{j_i',-m_{j_i}'\,\frac{1}{2}\mu_i} C^{j_i',-m_{j_i}'}_{J,-M_J j_{t_i} m_{j_{t_i}}}\\
&\times \; \delta_{m_{l_i}',0} T^{\Pi J}_{fi}(k_f\kappa_f, k_i\kappa_i')\Bigg)^*.
\end{aligned} \tag{D.13}$$

Next we apply

$$\sum_{M_J m_{j_{t_i}}} C^{j_i,-m_{j_i}}_{J,-M_J j_{t_i} m_{j_{t_i}}} C^{j_i',-m_{j_i}'}_{J,-M_J j_{t_i} m_{j_{t_i}}} = \delta_{j_i j_i'}\delta_{m_{j_i} m_{j_i}'}, \tag{D.14}$$

and

$$\sum_{m_{j_i}\mu_i} C^{l_i,-m_{l_i}}_{j_i,-m_{j_i}\,\frac{1}{2}\mu_i} C^{l_i',-m_{l_i}'}_{j_i,-m_{j_i}\,\frac{1}{2}\mu_i} = \delta_{l_i l_i'}\delta_{m_{l_i} m_{l_i}'}, \tag{D.15}$$

to finally obtain

$$\begin{aligned}
\sigma_{fi} &= (2\pi)^4 \left(\frac{k_f}{k_i}\right)\left(\frac{\epsilon_f\epsilon_i}{c^4}\right)\left(\frac{2J+1}{4\pi}\right)\frac{1}{2(2j_{\mathrm{target}_i}+1)}\\
&\times \sum_{\kappa_f\kappa_i J\Pi}\left|T^{\Pi J}_{fi}(k_f\kappa_f, k_i\kappa_i)\right|^2.
\end{aligned} \tag{D.16}$$

Defining

$$\begin{aligned}\sigma_{fi}^{J\Pi} &= (2\pi)^4 \left(\frac{k_f}{k_i}\right)\left(\frac{\epsilon_f \epsilon_i}{c^4}\right)\left(\frac{2J+1}{4\pi}\right)\frac{1}{2(2j_{\mathrm{target}_i}+1)} \\ &\times \sum_{\kappa_f \kappa_i}\left|T_{fi}^{\Pi J}(k_f\kappa_f, k_i\kappa_i)\right|^2,\end{aligned} \tag{D.17}$$

we have

$$\sigma_{fi} = \sum_{J\Pi} \sigma_{fi}^{J\Pi}. \tag{D.18}$$

Appendix E

Angular Momentum Algebra

For scalar tensor operators the Wigner-Eckart theorem [155, 156] gives

$$\langle jm|T_0^0|jm\rangle = \frac{1}{\sqrt{2j+1}}\langle j||T^0||j\rangle, \tag{E.1}$$

where the double bar || denotes matrix elements independent of the projection quantum number, m.

The following identities are useful for the calculation of matrix elements [148],

$$\begin{aligned}\langle j_1 j_2; jm|U^k(1)\cdot V^k(2)|j_1' j_2'; j'm'\rangle &= \delta_{jj'}\delta_{mm'}(-1)^{j_2+j_1'+2k+j} \\ &\times \begin{Bmatrix} j_1 & j_2 & j \\ j_2' & j_1' & k \end{Bmatrix} \langle j_1||U^k||j_1'\rangle\langle j_2||V^k||j_2'\rangle,\end{aligned} \tag{E.2}$$

where

$$\begin{aligned}\langle j_1 j_2; j||U^k(1)||j_1' j_2'; j'\rangle &= \sqrt{(2j+1)(2j'+1)}\delta_{j_2 j_2'}(-1)^{j_1+j_2+j'+k} \\ &\times \begin{Bmatrix} j_2 & j_1 & j \\ k & j' & j_1' \end{Bmatrix} \times \langle j_1||U^k||j_1'\rangle,\end{aligned} \tag{E.3}$$

and

$$\begin{aligned}\langle j_1 j_2; j||V^k(2)||j_1' j_2'; j'\rangle &= \sqrt{(2j+1)(2j'+1)}\delta_{j_1 j_1'}(-1)^{j_1'+j+k+j_2'} \\ &\times \begin{Bmatrix} j_1 & j & j_2 \\ k & j_2' & j' \end{Bmatrix} \times \langle j_2||V^k||j_2'\rangle.\end{aligned} \tag{E.4}$$

In the calculation of exchange matrix elements for two electron targets the following identity is useful,

$$|j_0, j_\gamma j_\delta(J_T) : J\rangle = \sum_j \hat{j}\hat{J}_T(-1)^{j_0+J_T+J_\gamma+j} \left\{ \begin{array}{ccc} j_0 & j_\delta & j \\ j_\gamma & J & J_T \end{array} \right\} |j_\gamma, j_0 j_\delta(j) : J\rangle. \tag{E.5}$$

In the calculation of T matrix elements and integrated cross sections the following relations are useful,

$$\sum_{M_1 M_2} C^{JM}_{J_1 M_1 J_2 M_2} C^{J'M'}_{J_1 M_1 J_2 M_2} = \delta_{JJ'}\delta_{MM'}, \tag{E.6}$$

$$\sum_{JM} C^{JM}_{J_1 M_1 J_2 M_2} C^{JM}_{J_1 M'_1 J_2 M'_2} = \delta_{M_1 M'_1}\delta_{M_2 M'_2}, \tag{E.7}$$

and

$$C^{JM}_{J_1 M_1 J_2 M_2} = (-1)^{J_1+J_2-J} C^{JM}_{J_2 M_2 J_1 M_1} \tag{E.8}$$

$$= (-1)^{J_2+M_2}\sqrt{\frac{2J+1}{2J_1+1}} C^{J_1 - M_1}_{J - M J_2 M_2} \tag{E.9}$$

$$= (-1)^{J_1-M_1}\sqrt{\frac{2J+1}{2J_2+1}} C^{J_2 - M_2}_{J_1 M_1 J - M}. \tag{E.10}$$

The following equation is useful for comparing the T-matrix elements generated with the RCCC code against the corresponding non-relativistic T-matrix elements generated with the CCC code,

$$\begin{aligned} |j_1 j_2(J_{12}), j_3 j_4(J_{34}) : JM\rangle &= \textstyle\sum_{J_{12}J_{24}} \sqrt{(2J_{12}+1)(2J_{34}+1)} \\ &\times \sqrt{(2J_{13}+1)(2J_{24}+1)} \\ &\times \left\{ \begin{array}{ccc} j_1 & j_2 & J_{12} \\ j_3 & j_4 & J_{34} \\ J_{13} & J_{24} & J \end{array} \right\} \\ &\times |j_1 j_3(J_{13}), j_2 j_4(J_{24}) : JM\rangle. \end{aligned} \tag{E.11}$$

Appendix F

Historical Aspects of Relativistic Quantum Theory

The historical development of relativistic quantum theory has traversed a tumultuous path. Einstein, who played a leading role in the development of both quantum theory and special relativity did not publish any papers in which he explicitly attempted to unite special relativity with quantum theory. Pais [157] in reflecting on his encounters with Einstein highlighted the following:

> "It is striking how from the very beginning, Einstein kept his scientific writing on relativity theory separate from that on quantum theory. This was evident already in 1905. In his first relativity paper Einstein noted: 'It is remarkable that the energy and frequency of a light complex vary with the state of motion of the observer with the same law.' Here was an obvious opportunity to refer to the relation $E = h\nu$ of his paper on light-quanta, finished a few months earlier. But Einstein did not do that."

and furthermore:

> "It was even more difficult to discuss quantum field theory with him. He was willing to admit that quantum mechanics was successful on the non-relativistic level. However, he did not believe that this theory provided a secure basis for relativistic generalizations. Relativistic quantum field theory was repugnant to him. Valentine Bargmann has told me that Einstein asked him to give

> a private survey of quantum field theory, beginning with second quantization. Bargmann did so for about a month. Thereafter Einstein's interest waned."*

Dirac played a key role in synthesizing special relativity with quantum theory and yet, in the later parts of his life, expressed concern with the foundations of relativistic quantum theories, particularly renormalization techniques, and even suggested that Lorentz invariance might need to be dropped if the renormalization techniques were to be maintained [158]. It is also of importance to note that the prediction of the gyromagnetic ratio $g = 2$ and two component spin of the electron, initial vindications of the Dirac equation, can both be obtained from a non-relativistic wave equation that is linear in $\frac{\partial}{\partial x}, \frac{\partial}{\partial y}, \frac{\partial}{\partial z}$ and $\frac{\partial}{\partial t}$. Greiner [159] presents an elegant derivation and then explicitly states:

> "*Thus a completely non-relativistic linearized theory predicts the correct intrinsic magnetic moment of a spin-1/2 particle.* In contrast to this, almost all textbooks falsely claim that the anomalous magnetic moment is due to *relativistic* properties. The existence of spin is therefore not a relativistic effect, as is often asserted, but is a *consequence of the linearization of the wave equations.*"

The conceptual problems that arise when the Dirac equation is augmented with hole theory have been clearly pointed out by Weinberg in his treatise on quantum field theory [160] :

> "How can we interpret the antiparticles of charged *bosons*, such as the $\pi^{\pm}$ mesons or $W^{\pm}$ particles, as holes in a sea of negative energy states? For particles quantized according to Bose-Einstein statistics, there is no exclusion principle, and hence nothing to keep positive-energy particles from falling down into the negative-energy states, occupied or not. And if the hole theory does not work for bosonic antiparticles, why should we believe it for fermions?"

*One can appreciate Einstein's concern with extending special relativity into the domain of quantum theory: the former is founded on Maxwell's equations and their invariance, the latter was developed in order to replace Maxwell's equations because Maxwell's equations predicted that atomic orbitals would be unstable due to the continuous emission of electromagnetic waves.

Nevertheless, as highlighted by Sakurai [81], there are two compelling arguments for developing relativistically covariant quantum theories:

1. Quantum theories should recover the relativistic energy momentum relation in the classical limit $\hbar \to 0$ in accordance with the correspondence principle.

2. Relativistic quantum field theories provide a framework in which the creation and annihilation of particles and antiparticles can be modeled in a convenient manner.

Bibliography

[1] C. J. Fontes, D. H. Sampson, and H. L. Zhang. *Phys. Rev. A*, 47(2): 1009, 1993.

[2] N. Nakamura, D. Kato, N. Miura, T. Nakahara, and S. Ohtani. *Phys. Rev. A*, 63(2):024501, 2001.

[3] D. L. Robbins, P. Beiersdorfer, A. Ya. Faenov, T. A. Pikuz, D. B. Thorn, H. Chen, K. J. Reed, A. J. Smith, K. R. Boyce, G. V. Brown, R. L. Kelley, C. A. Kilbourne, and F. S. Porter. *Phys. Rev. A* , 74(2):022713, 2006.

[4] URL `http://www.nist.gov/`

[5] C. J. Fontes, D. H. Sampson, and H. L. Zhang. *Phys. Rev. A*, 59(2): 1329, 1999.

[6] R. E. Marrs, S. R. Elliott, and D. A. Knapp. *Phys. Rev. Lett.*, 72: 4082, 1994.

[7] O. Zatsarinny and K. Bartschat. *Phys. Rev. A*, 79(4):042713, 2009.

[8] G. F. Hanne, V. Nickich, and M. Sohn. *J. Phys. B*, 18(10):2037, 1985.

[9] T. W. Ottley and H. Kleinpoppen. *J. Phys. B*, 8(4):621, 1975.

[10] N. M. Erdevdi, O. B. Shpenik, and V. S. Vukstich. *Opt. Spectrosc*, 95: 529, 2003.

[11] D. S. Newman, M. Zubek, and G. C. King. *J. Phys. B*, 18(5):985, 1985.

[12] W. L. Borst. *Phys. Rev.*, 181:257, 1969.

[13] H. F. Krause, S. G. Johnson, and S. Datz. *Phys. Rev. A*, 15:611, 1977.

[14] D. V. Fursa, I. Bray, and G. Lister. *J. Phys. B*, 36:4255, 2003.

[15] M. Zubek, N. Gulley, A. Danjo, and G. C. King. *J. Phys. B*, 29:5927, 1996.

[16] R. Panajotović, V. Pejčev, M Konstantinović, D. Filipović, V. Bočvarski, and B. Marinković. *J. Phys. B*, 26:1005, 1993.

[17] F. J. Peitzmann and J. Kessler. *J. Phys. B*, 23:2629, 1990.

[18] G. Holtkamp, K. Jost, F. J. Peitzmann, and J. Kessler. *J. Phys. B*, 20:4543, 1987.

[19] K. Jost and B. Ohnemus. *Phys. Rev. A*, 19:641, 1979.

[20] M. Zubek, A. Danjo, and G. C. King. *J. Phys. B*, 28:4117, 1995.

[21] R. P. McEachran and M. T. Elford. *J. Phys. B*, 36(3):427, 2003.

[22] J. P. England and M. T. Elford. *Aust. J. Phys.*, 44(3):647, 1991.

[23] H. Geiger and E. Marsden. *Proc. R. Soc. London A*, 82:495, 1909.

[24] J. Franck and G. Hertz. *Verh. Deutschen Phys. Ges.*, 16:457, 1914.

[25] I. E. McCarthy and A. T. Stelbovics. *Phys. Rev. A*, 28:2693, 1983.

[26] B. A. Lippmann and J. Schwinger. *Phys. Rev.*, 79:469, 1950.

[27] I. Bray and A. T. Stelbovics. *Phys. Rev. A*, 46:6995, 1992.

[28] H-A. Yalim, D. Cvejanovic, and A. Crowe. *Phys. Rev. Lett.*, 79:2951, 1997.

[29] R. W. O'Neill, P. J. M. van der Burgt, D. Dziczek, P. Bowe, S. Chwirot, and J. A. Slevin. *Phys. Rev. Lett.*, 80:1630, 1998.

[30] J. F. Williams and A. G. Mikosza. *J. Phys. B*, 39(20):4113, 2006.

[31] J. F. Williams and A. G. Mikosza. *J. Phys. B*, 39(20):4339, 2006.

[32] H. S. W. Massey and C. B. O. Mohr. *Proc. Roy. Soc. A*, 146:880, 1934.

[33] N. F. Mott and H. S. W. Massey. *Theory of atomic Collisions*. Oxford University Press, London, 1965.

[34] D. V. Fursa and I. Bray. *Phys. Rev. A*, 52:1279, 1995.

[35] A. S. Kheifets and I. Bray. *Phys. Rev. Lett.*, 81:4588, 1998.

[36] M. Achler, V. Mergel, L. Spielberger, R. Dorner, Y. Azuma, and H. Schmidt-Böcking. *J. Phys. B*, 34(6):965, 2001.

[37] I. Bray. *Phys. Rev. A*, 49:1066, 1994.

[38] D. V. Fursa and I. Bray. *J. Phys. B*, 30:5895, 1997.

[39] I. Bray and D. V. Fursa. *Phys. Rev. A*, 54:2991, 1996.

[40] I. Bray and D. V. Fursa. *Phys. Rev. Lett.*, 76:2674, 1996.

[41] I. Bray. *Phys. Rev. Lett.*, 89:273201, 2002.

[42] A. T. Stelbovics, I. Bray, D. V. Fursa, and K. Bartschat. *Phys. Rev. A*, 71:052716(13), 2005.

[43] A. Einstein. *Annalen der Physik*, 17:891, 1905.

[44] H. M. Schwartz. *American Journal of Physics*, 45(1):18, 1977.

[45] M. Jammer. *The conceptual development of quantum mechanics*. Tomash Publishers, 1989.

[46] E. Schrödinger. *Annalen der Physik*, 79 (4):361, 1926.

[47] E. Schrödinger. *Annalen der Physik*, 79 (6):489, 1926.

[48] E. Schrödinger. *Annalen der Physik*, 79 (8):734, 1926.

[49] E. Schrödinger. *Annalen der Physik*, 80 (13):437, 1926.

[50] E. Schrödinger. *Annalen der Physik*, 79 (6):173, 1926.

[51] E. Schrödinger. *Naturwissenschaften*, 14:664, 1926.

[52] W. Heisenberg. *Z. Phys.*, 33:879, 1925.

[53] M. Born, W. Heisenberg, and P. Jordan. *Z. Phys.*, 35:557, 1925.

[54] P. A. M. Dirac. *Proc. Roy. Soc. (London)*, A117:610, 1928.

[55] P. A. M. Dirac. *The Principles of Quantum Mechanics*. Oxford University Press; 4th edition, 1982.

[56] J. Schwinger. *Phys. Rev.*, 73:416, 1948.

[57] J. Schwinger. *Phys. Rev.*, 76:790, 1949.

[58] J. Schwinger. *Phys. Rev.*, 75:898, 1949.

[59] J. Schwinger. *Phys. Rev.*, 82:664, 1951.

[60] S. Tomonaga. *Phys. Rev.*, 74:224, 1948.

[61] R. P. Feynman. *Phys. Rev.*, 76:749, 1949.

[62] R. P. Feynman. *Phys. Rev.*, 76:769, 1949.

[63] R. P. Feynman. *Phys. Rev.*, 80:440, 1950.

[64] F. J. Dyson. *Phys. Rev.*, 75:486, 1949.

[65] F. J. Dyson. *Phys. Rev.*, 75:1736, 1949.

[66] J. Schwinger, editor. *Selected Papers on Quantum Electrodynamics*. Dover Publication, 1958.

[67] S. S. Schweber. *QED and the men who made it: Dyson, Feynman, Schwinger, and Tomonaga*. Princeton Univ. Press, 1994.

[68] W. E. Lamb Jr. and R. R. C. Retherford. *Phys. Rev.*, 72:241, 1947.

[69] H. A. Bethe. *Phys. Rev.*, 72:339, 1947.

[70] W. H. Furry. *Phys. Rev.*, 81(1):115, 1951.

[71] "Relativistic Quantum Electrodynamics", by H.M. Quiney, in "*Handbook of Molecular Physics and Quantum Chemistry*", John Wiley & Sons, Ltd, Chichester, 2003.

[72] I. P. Grant. *Relativistic Quantum Theory of Atoms and Molecules: Theory and Computations*. Springer, 2007.

[73] J. J. Chang. *J. Phys. B*, 8:2327, 1975.

[74] P. H. Norrington and I. P. Grant. *J. Phys. B*, 14:L261, 1981.

[75] S. Ait-Tahar, I. P. Grant, and P. H. Norrington. *Phys. Rev. Lett.*, 79: 2955, 1997.

[76] M. J. Vilkas and Y. Ishikawa. *Phys. Rev. A*, 75(6):062508, 2007.

[77] O. Zatsarinny and K. Bartschat. *Phys. Rev. A*, 77:062701, 2008.

[78] O. Zatsarinny and K. Bartschat. *Phys. Rev. A*, 79(4):042713, 2009.

[79] N. R. Badnell. *J. Phys. B*, 41(17):175202, 2008.

[80] M. S. Pindzola, J. A. Ludlow, F. Robicheaux, J. Colgan, and C. J. Fontes. *Phys. Rev. A*, 80(5):052706, 2009.

[81] J. Sakurai. *Advanced Quantum Mechanics*. Addison-Wesley, 1967.

[82] K. G. Dyall, I. P. Grant, C. T. Johnson, F. P. Parpia, and E. P. Plummer. *Comp. Phys. Comm.*, 55:425, 1989.

[83] P. Strange. *Relativistic Quantum Mechanics*. Cambridge University Press, 1998.

[84] R. P. McEachran, D. L. Morgan, A. G. Ryman, and A. D. Stauffer. *J. Phys. B*, 10:663, 1977.

[85] W. Kutzelnigg. *Int. J. Quantum Chem.*, 25:107, 1984.

[86] I. P. Grant and H. M. Quiney. *Phys. Rev. A*, 62:022508, 2000.

[87] R. Szmytkowski. *J. Phys. B*, 30(4):825, 1997.

[88] I. S. Gradshteyn and I. M. Ryzhik. *Tables of Integrals, Series and Products*. Academic Press, San Diego, 1980.

[89] P. A. M. Dirac. *Proc. Roy. Soc. (London) Series A*, 118:351, 1928.

[90] I. P. Grant. *Advan. Phys.*, 19:747, 1970.

[91] R. H. Landau. *Quantum theory II: second course in quantum theory*. A. Wiley Interscience publication, 1989.

[92] A. T. Stelbovics. *Phys. Rev. A*, 41:2536, 1990.

[93] J. Sucher. *Phys. Rev. A*, 22:348, 1980.

[94] M. Rose. *Relativistic Electron Theory*. John Wiley and Sons, 1961.

[95] J. E. Sienkiewicz and W. E. Baylis. *J. Phys. B*, 20:5145, 1987.

[96] F. Salvat, J. M. Fernandez-Varea, and W. Williamson Jr. *Comp. Phys. Comm.*, 90:151, 1995.

[97] C. J. Joachain. *Quantum collision theory*. Elsevier Science Publishers B. V., Amsterdam, 3rd edition, 1983.

[98] G. Baum, N. Pavlovič, B. Roth, K. Bartschat, Y. Fang, and I. Bray. *Phys. Rev. A*, 66:022705, 2002.

[99] K. Bartschat and Y. Fang. *Phys. Rev. A*, 62:052719, 2000.

[100] M. Inokuti. *Rev. Mod. Phys.*, 43:297, 1971.

[101] C. J. Fontes and H. L. Zhang. *Phys. Rev. A*, 76:040703(R), 2007.

[102] G. Breit. *Phys. Rev.*, 34(4):553, 1929.

[103] G. Breit. *Phys. Rev.*, 36(3):383, 1930.

[104] G. Breit. *Phys. Rev.*, 39(4):616, 1932.

[105] C. Møller. *Ann. Phys.*, 14:531, 1932.

[106] W. Greiner. *Quantum Electrodynamics*. Springer-Verlag, 1996.

[107] J. Hata and I. P. Grant. *J. Phys. B*, 17(5):L107, 1984.

[108] D. W. Walker. *J. Phys. B*, 8(5):760, 1975.

[109] Abramowitz and Stegun, editors. *Handbook of Mathematical Functions*. Dover Publications, 1965.

[110] M. H. Mittleman. *Phys. Rev. A*, 4(3):893, 1971.

[111] M. H. Mittleman. *Phys. Rev. A*, 5(6):2395, 1972.

[112] M. H. Mittleman. *Phys. Rev. A*, 24(3):1167, 1981.

[113] D. L. Moores and M. S. Pindzola. *J. Phys. B*, 25(21):4581, 1992.

[114] D. V. Fursa, C. J. Bostock, and I. Bray. *Phys. Rev. A*, 80(2):022717, 2009.

[115] I. C. Percival and M. J. Seaton. *Philosophical Transactions of the Royal Society of London. Series A, Mathematical and Physical Sciences*, 251(990):113, 1958.

[116] S. A. Napier, D. Cvejanović, J. F. Williams, L. Pravica, D. Fursa, I. Bray, O. Zatsarinny, and K. Bartschat. *Phys. Rev. A*, 79(4):042702, 2009.

[117] M. Maslov, M. J. Brunger, P. J. O. Teubner, O. Zatsarinny, K. Bartschat, D. Fursa, I. Bray, and R. P. McEachran. *Phys. Rev. A*, 77(6):062711, 2008.

[118] W. Kedzierski, A. Abdellatif, J. W. McConkey, K. Bartschat, D. V. Fursa, and I. Bray. *J. Phys. B*, 34:3367, 2001.

[119] M. K. Inal and J. Dubau. *J. Phys. B*, 20:4221, 1987.

[120] P. Hakel, R. C. Mancini, C. Harris, P. Neill, P. Beiersdorfer, G. Csanak, and H. L. Zhang. *Phys. Rev. A*, 76:012716, 2007.

[121] K. J. Reed and M. H. Chen. *Phys. Rev. A*, 48(5):3644, 1993.

[122] H. L. Zhang, D. H. Sampson, and R. E. H. Clark. *Phys. Rev. A*, 41 (1):198, 1990.

[123] Y. Itikawa, R. Srivastava, and K. Sakimoto. *Phys. Rev. A*, 44(11): 7195, 1991.

[124] G. Weber. Private communication.

[125] I. Bray. *Phys. Rev. Lett.*, 78:4721, 1997.

[126] D. L. Moores and K. J. Reed. *Phys.Rev. A*, 51(1):R9, 1995.

[127] C. J. Fontes, D. H. Sampson, and H. L. Zhang. *Phys.Rev. A*, 51(1): R12, 1995.

[128] I. E. McCarthy and E. Weigold. *Electron-Atom Collisions*. Cambridge University Press, Cambridge, 1995.

[129] J. Kessler. *Polarized Electrons*. Springer, Berlin, 1985.

[130] J. F. Waymouth. *Electric Discharge Lamps*. The MIT Press, Cambridge, MA, 1971.

[131] G. G. Lister. In R. Hippler, S. Pfau, M. Schmidt, and K. H. Schoenbach, editors, *Low Temperature Plasma Physics: Fundamental Aspects and Applications*, page 387. Wiley, 2001.

[132] G. G. Lister, J. E. Lawler, W. P. Lapatovich, and V. A. Godyak. *Rev. Mod. Phys.*, 76(2):541, 2004.

[133] S. D Rockwood. *Phys. Rev. A*, 8:2348, 1973.

[134] M. T. Elford. *Aust. J. Phys.*, 33:251, 1980.

[135] D. W. Walker. *Adv. Phys.*, 20:257, 1971.

[136] R. P. McEachran and A. D. Stauffer. *J. Phys. B*, 20:5517, 1987.

[137] J. E. Sienkiewicz. *J. Phys. B*, 23:1869, 1990.

[138] J. E. Sienkiewicz. *J. Phys. B*, 30:1261, 1997.

[139] R. Haberland and L. Fritsche. *J. Phys. B*, 20:121, 1987.

[140] N. S. Scott, P G Burke, and K Bartschat. *J. Phys. B*, 16(11):L361, 1983.

[141] K. Bartschat, N. S. Scott, K. Blum, and P. G. Burke. *J. Phys. B*, 17 (2):269, 1984.

[142] K. Bartschat. Benchmark calculations for electron collisions with complex atoms. In F. Ownby D.R. Schultz, P.S. Krstic, editor, *Proceedings of the 3rd International Conference on Atomic and Molecular Data*. American Institute of Physics, 2002.

[143] W. P. Wijesundera, I. P. Grant, and P. H. Norrington. *J. Phys. B*, 25: 2143, 1992.

[144] K. Bartschat and D. H. Madison. *J. Phys. B*, 20:1609, 1987.

[145] R. Srivastava, T. Zuo, R. P. McEachran, and A. D. Stauffer. *J. Phys. B*, 26:1025, 1993.

[146] T. M. Miller and B. Bederson. *Adv. Atom. Mol. Phys.*, 13:1, 1977.

[147] I. Bray, D. V. Fursa, and I. E. McCarthy. *J. Phys. B*, 27:L421, 1994.

[148] A. R. Edmonds. *Angular Momentum in Quantum Mechanics*. Princeton University Press, 1957.

[149] L. S. Blackford, J. Choi, A. Cleary, E. D'Azeuedo, J. Demmel, I. Dhillon, S. Hammarling, G. Henry, A. Petitet, K. Stanley, D. Walker, and R. C. Whaley. *ScaLAPACK user's guide*. Society for Industrial and Applied Mathematics, Philadelphia, PA, USA, 1997.

[150] J. P. Sullivan, P. D. Burrow, D. S. Newman, K. Bartschat, J. A. Michejda, R. Panajotovic, M. Moghbelalhossein, R. P. McEachran, and S. J. Buckman. *New Journal of Physics*, 5(1):159, 2003.

[151] G. F. Hanne. *American Journal of Physics*, 56(8):696, 1988.

[152] P. Roman. *Advanced Quantum Theory*. Addison-Wesley, 1965.

[153] B. H. Bransden. *Atomic collision theory*. Lecture notes and supplements in physics. Benjamin/Cummings, Reading, Massachusetts, 2nd edition, 1983.

[154] M. L. Goldberger and K. M. Watson. *Collision Theory*. Krieger Publishing Co., New York, 1975.

[155] E. P. Wigner. *Z. Physik*, 43:624, 1927.

[156] C. Eckart. *Rev. Mod. Phys.*, 2:305, 1930.

[157] A. Pais. *Rev. Mod. Phys.*, 51(4):863, 1979.

[158] H. Kragh. *Dirac: A Scientific Biography*. Cambridge University Press, Cambridge, 1990.

[159] W. Greiner. *Quantum Mechanics: An Introduction*, page 366. Springer-Verlag, 1989.

[160] S. Weinberg. *The Quantum Theory of Fields, Vol I*, page 11. Cambridge University Press, 1996.

Every reasonable effort has been made to acknowledge the owners of copyright material. I would be pleased to hear from any copyright owner who has been ommitted or incorrectly acknowledged.